1-1-2014

Magnetic Resonance Imaging of Short-T2 Tissues with Applications for Quantifying Cortical Bone Water and Myelin

Cheng Li
University of Pennsylvania, licheng6@seas.upenn.edu

Magnetic Resonance Imaging of Short-T2 Tissues with Applications for Quantifying Cortical Bone Water and Myelin

Abstract
The human body contains a variety of tissue species with short T2 ranging from a few microseconds to hundreds of microseconds. Detection and quantification of these short-T2 species is of considerable clinical and scientific interest. Cortical bone water and myelin are two of the most important tissue constituents. Quantification of cortical bone water concentration allows for indirect estimation of bone pore volume and noninvasive assessment of bone quality. Myelin is essential for the proper functioning of the central nervous system (CNS). Direct assessment of myelin would reveal CNS abnormalities and enhance our understanding of neurological diseases.

However, conventional MRI with echo times of several milliseconds or longer is unable to detect these short-lived MR signals. Recent advances in MRI technology and hardware have enabled development of a number of short-T2 imaging techniques, key among which are ultra-short echo time (UTE) imaging, zero echo time (ZTE) imaging, and sweep imaging with Fourier transform (SWIFT). While these pulse sequences are able to detect short-T2 species, they still suffer from signal interference between different T2 tissue constituents, image artifacts and excessive scan time. These are primary technical hurdles for application to whole-body clinical scanners. In this thesis research, new MRI techniques for improving short-T2 tissue imaging have been developed to address these challenges with a focus on direct detection and quantification of cortical bone water and myelin on a clinical MRI scanner.

The first focus of this research was to optimize long-T2 suppression in UTE imaging. Saturation and adiabatic RF pulses were designed to achieve maximum long-T2 suppression while maximizing the signal from short-T2 species. The imaging protocols were optimized by Bloch equation simulations and were validated using phantom and in vivo experiments. The results show excellent short-T2 contrast with these optimized pulse sequences.

The problem of blurring artifacts resulting from the inhomogeneous excitation profile of the rectangular pulses in ZTE imaging was addressed. The proposed approach involves quadratic phase-modulated RF excitation and iterative solution of an inverse problem formulated from the signal model of ZTE imaging and is shown to effectively remove the image artifacts.

Subsequently image acquisition efficiency was improved in order to attain clinically-feasible scan times. To accelerate the acquisition speed in UTE and ZTE imaging, compressed sensing was applied with a hybrid 3D UTE sequence. Further, the pulse sequence and reconstruction procedure were modified to enable anisotropic field-of-view shape conforming to the geometry of the elongated imaged object.

These enhanced acquisition techniques were applied to the detection and quantification of cortical bone water. A new biomarker, the suppression ratio (a ratio image derived from two UTE images, one without and the other with long-T2 suppression), was conceived as a surrogate measure of cortical bone porosity. Experimental data suggest the suppression ratio may be a more direct measure of porosity than previously measured total bone water concentration.

Lastly, the feasibility of directly detecting and quantifying spatially-resolved myelin concentration with a clinical imager was explored, both theoretically and experimentally. Bloch equation simulations were conducted to investigate the intrinsic image resolution and the fraction of detectable myelin signal under

current scanner hardware constraints. The feasibility of quantitative ZTE imaging of myelin extract and lamb spinal cord at 3T was demonstrated.

The technological advances achieved in this dissertation research may facilitate translation of short-T2 MRI methods from the laboratory to the clinic.

Degree Type
Dissertation

Degree Name
Doctor of Philosophy (PhD)

Graduate Group
Bioengineering

First Advisor
Felix W. Wehrli

Keywords
Bone Water, Magnetic Resonance Imaging, Myelin, Short T2 Relaxation Time, Ultrashort Echo Time, Zero Echo Time

Subject Categories
Biomedical | Radiology

MAGNETIC RESONANCE IMAGING OF SHORT-T_2 TISSUES WITH APPLICATIONS FOR QUANTIFYING CORTICAL BONE WATER AND MYELIN

Cheng Li

A DISSERTATION

in

Bioengineering

Presented to the Faculties of the University of Pennsylvania

in

Partial Fulfillment of the Requirements for the

Degree of Doctor of Philosophy

2014

Supervisor of Dissertation

_____

Felix W. Wehrli, Ph.D.

Professor of Radiology

Graduate Group Chairperson

_____

Jason A. Burdick, Ph.D.

Professor of Bioengineering

Dissertation Committee

Charles L. Epstein, Ph.D., Professor of Mathematics

Ravinder Reddy, Ph.D., Professor of Radiology

Hee Kwon Song, Ph.D., Associate Professor of Radiology

To My family

ACKNOWLEDGMENT

The work presented in this dissertation would not have been possible without help and support from many people.

I am deeply grateful to my advisor, Dr. Felix Wehrli, for the unique opportunity to work in his research group and for his constant guidance, support, and encouragement throughout my Ph.D. work. His deep and broad knowledge of MRI, astute scientific insight and creative thinking, enthusiasm for high-quality research, patience and dedication toward his students has set up a model to follow in my future career. I would also like to thank my Ph.D. committee members, Dr. Charles Epstein, Dr. Ravinder Reddy and Dr. Hee Kwon Song, for their time, effort and valuable comments on my dissertation.

I am indebted to Drs. Jeremy Magland, Michael Langham, and Chamith Rajapakse for their help, support and encouragement. I have enjoyed the fruitful discussion with them particularly during our lunch time in the small conference room. My warmest thanks also go to all my lab mates, especially to Hamidreza Saligheh Rad, Henry Ong, Michael Wilhelm, Alan Seifert, Varsha Jain, Zach Rodgers and Erin Englund. Part of this thesis work would not be possible without my collaboration with Alan Seifert. His dedication to the work deeply impressed me. I would also like to thank our lab Associate Director Holly Flachs for her time and assistance in making my research work run smoothly.

I am indebted to Dr. Danny J.J. Wang at UCLA for his support and encouragement, to Dr. Kui Ying at Tsinghua University, China for guiding me into the MRI field.

I would also like to thank the financial support from the Howard Hughes Medical Institute (HHMI) with the international student research fellowship.

Finally, my special thanks go to my family for their love, support and encouragement through these years. This dissertation is dedicated to them.

Cheng Li

University of Pennsylvania

December, 2014

ABSTRACT

MAGNETIC RESONANCE IMAGING OF SHORT-T_2 TISSUES WITH APPLICATIONS FOR QUANTIFYING CORTICAL BONE WATER AND MYELIN

Cheng Li

Felix W. Wehrli, Ph.D.

The human body contains a variety of tissue species with short T_2 ranging from a few microseconds to hundreds of microseconds. Detection and quantification of these short-T_2 species is of considerable clinical and scientific interest. Cortical bone water and myelin are two of the most important tissue constituents. Quantification of cortical bone water concentration allows for indirect estimation of bone pore volume and noninvasive assessment of bone quality. Myelin is essential for the proper functioning of the central nervous system (CNS). Direct assessment of myelin would reveal CNS abnormalities and enhance our understanding of neurological diseases.

However, conventional MRI with echo times of several milliseconds or longer is unable to detect these short-lived MR signals. Recent advances in MRI technology and hardware have enabled development of a number of short-T_2 imaging techniques, key among which are ultra-short echo time (UTE) imaging, zero echo time (ZTE) imaging, and sweep imaging with Fourier transform (SWIFT). While these pulse sequences are able to detect short-T_2 species, they still suffer from signal interference between different T_2 tissue constituents, image artifacts and excessive scan time. These are primary technical hurdles for application to whole-body clinical scanners. In this thesis research, new MRI techniques for improving short-T_2 tissue imaging have been developed to

address these challenges with a focus on direct detection and quantification of cortical bone water and myelin on a clinical MRI scanner.

The first focus of this research was to optimize long-T_2 suppression in UTE imaging. Saturation and adiabatic RF pulses were designed to achieve maximum long-T_2 suppression while maximizing the signal from short-T_2 species. The imaging protocols were optimized by Bloch equation simulations and were validated using phantom and *in vivo* experiments. The results show excellent short-T_2 contrast with these optimized pulse sequences.

The problem of blurring artifacts resulting from the inhomogeneous excitation profile of the rectangular pulses in ZTE imaging was addressed. The proposed approach involves quadratic phase-modulated RF excitation and iterative solution of an inverse problem formulated from the signal model of ZTE imaging and is shown to effectively remove the image artifacts.

Subsequently image acquisition efficiency was improved in order to attain clinically-feasible scan times. To accelerate the acquisition speed in UTE and ZTE imaging, compressed sensing was applied with a hybrid 3D UTE sequence. Further, the pulse sequence and reconstruction procedure were modified to enable anisotropic field-of-view shape conforming to the geometry of the elongated imaged object.

These enhanced acquisition techniques were applied to the detection and quantification of cortical bone water. A new biomarker, the suppression ratio (a ratio image derived from two UTE images, one without and the other with long-T_2 suppression), was conceived as a surrogate measure of cortical bone porosity.

Experimental data suggest the suppression ratio may be a more direct measure of porosity than previously measured total bone water concentration.

Lastly, the feasibility of directly detecting and quantifying spatially-resolved myelin concentration with a clinical imager was explored, both theoretically and experimentally. Bloch equation simulations were conducted to investigate the intrinsic image resolution and the fraction of detectable myelin signal under current scanner hardware constraints. The feasibility of quantitative ZTE imaging of myelin extract and lamb spinal cord at 3T was demonstrated.

The technological advances achieved in this dissertation research may facilitate translation of short-T_2 MRI methods from the laboratory to the clinic.

TABLE OF CONTENTS

LIST OF TABLES

LIST OF ILLUSTRATIONS

Chapter 1 Introduction

1.1 T_2 Relaxation Time

MRI contrast of biological tissues is essentially characterized by their physical and physiological properties, which include T_1 and T_2 relaxation, magnetic susceptibility, diffusion and perfusion. However, the T_2 relaxation time constant, which determines the lifetime of the transverse magnetization, is perhaps one of the important parameters for quantitatively assessing tissue physiology and pathology. The T_2 relaxation time of biological tissues covers almost six orders of magnitude, ranging from a few microseconds to several seconds. Fig. 1.1 shows the T_2 spectrum of various human tissues at 3T.

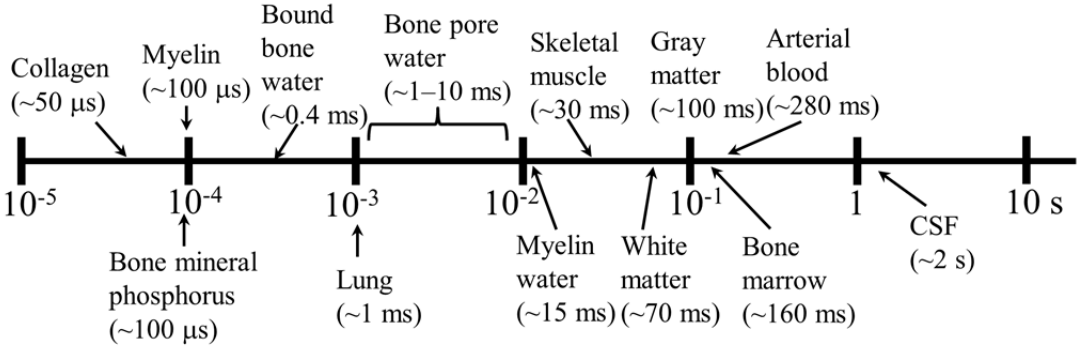

Figure 1.1 T_2 proton spectrum of various human tissues at 3T. A logarithmic scale is used to indicate the full range of T_2 values.

As indicated in Fig. 1.1, the human body contains a variety of short-T_2 tissue constituents with proton T_2 values ranging from a few microseconds to tens and hundreds of microseconds, including myelin (1), cortical bone water (BW) (2,3), lung tissue (4), as well as ^{31}P in bone mineral (5). Detection and quantification of these short-T_2 species is

of considerable clinical and scientific interest. For example, assessment of myelin would reveal central nervous system abnormalities and enhance our understanding of neurological diseases (6). However, conventional MRI with echo times (TEs) of several milliseconds or longer is unable to detect these short life-time MR signals.

With recent advances in MRI technology and hardware, several techniques have emerged for imaging short-T_2 constituents, including ultrashort echo-time (UTE) imaging (7), zero echo-time (ZTE) imaging (8-10), and sweep imaging with Fourier transform (SWIFT) (11). With these imaging pulse sequences, the short-T_2 species become visible, allowing researchers to explore and assess physiology and pathology of the short-T_2 tissues.

1.2 Magnetic Resonance Imaging of Short-T_2 Tissues

1.2.1 UTE Imaging

Currently UTE imaging is the most widely used short-T_2 imaging pulse sequence on clinical scanners due to its minimal hardware requirements and the availability of both 2D and 3D imaging (7,12). In order to capture the rapidly-decaying signal, effective echo times in UTE sequences need to be on the order of tens of microseconds or less. This can be accomplished by half or hard pulses (13,14), fast T/R switching and appropriate sampling strategies, e.g. radial center-out trajectories with ramp sampling. Figure 1.2 shows a typical 2D UTE imaging pulse sequence diagram.

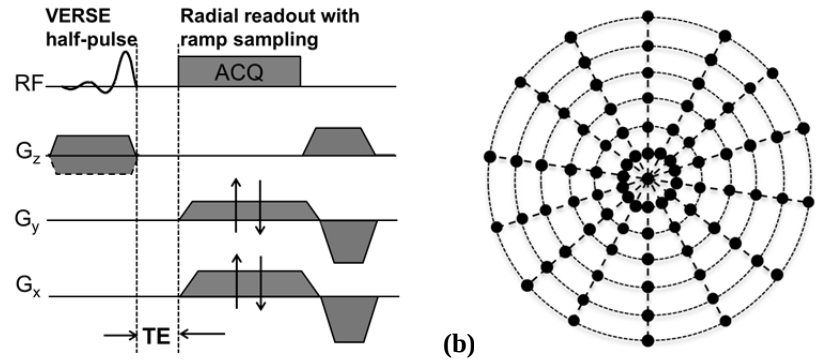

Figure 1.2 (a) 2D UTE pulse sequence diagram. The VERSE half-pulse is used to achieve slice selection. Data from two scans with slice selection gradient of opposite polarities are summed to cancel the out-of-slice magnetization response resulting from half-pulse excitation. To minimize the echo time, a radial center-out trajectory with ramp sampling is used. (b) The corresponding radial sampling trajectory. The solid dots represent discrete *k*-space samples.

One advantage of UTE imaging is that both 2D and 3D imaging versions are available. In 2D imaging, slice selectivity is achieved by a half-pulse to maintain minimum echo time. Specifically, the half-pulse is played out with a slice-selection gradient of opposite polarities in pairs of scans acquired for each spoke (14). Although each half-pulse itself excites the out-of-slice spins, the undesired out-of-slice magnetization is removed by summation of the signal from the two scans. The underlying principle is that the spatial response of a real-valued pulse is skew-Hermitian symmetric and the sum of the spatial profiles from two scans with opposite gradients cancels the unwanted resulting magnetization. To further minimize the echo time, a variable rate selective excitation (VERSE) half-pulse is often used (15). Another advantage of UTE is that it is flexible to change the echo time, allowing to measure short-T_2* relaxation time.

Images acquired by UTE sequences are reconstructed by a gridding algorithm (16), consisting of non-uniform sampling density compensation and non-uniform fast Fourier transform (NUFFT) (17). Artifacts may appear in the reconstructed images mainly due to the imperfect half-pulse excitation and sampling during gradient ramp. Several

approaches were proposed to correct these artifacts. Most of these methods are based on accurate characterization of gradient waveforms (18,19), since the resulting artifacts in UTE are caused by eddy current and gradient delays. For example, the author's laboratory developed a simple technique for mapping the k-space trajectory of the initial readout ramp to correct readout gradient imperfection (20). This method uses data from a short calibration scan in which two dimensions of spatial encoding are applied prior to readout. After correcting for B_0 inhomogeneity, it provides an accurate measurement of the *k*-space trajectory during the ramp, which can be used as input to a gridding-based reconstruction algorithm. Figure 1.3 (a) shows the measured gradient at 7T MRI along with an ideally trapezoidal gradient. When using the trapezoidal gradient for image reconstruction, the artifact is obvious, especially on the edge of the image, as shown in Figure 1.3 (b, c). The artifact is removed when using the measured gradient information for image reconstruction.

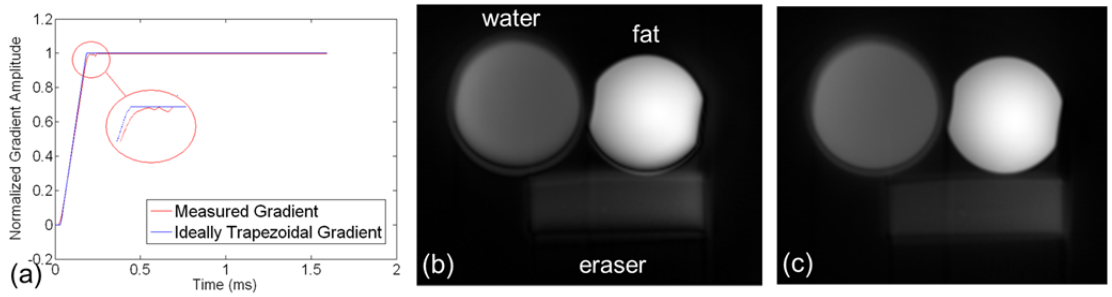

Figure 1.3 (a) measured gradient waveform (red) in a UTE sequence deviates from the desired trapezoidal gradient (blue). Images reconstructed assuming a trapezoidal gradient (b) and (c) measured gradient waveforms.

1.2.2 ZTE Imaging

In distinction to UTE, in ZTE the imaging gradient is turned on before RF transmission, which offers multiple advantages over UTE imaging. First, *k*-space is

traversed within a shorter time period, resulting in higher SNR and reduced blurring due to reduced T_2 decay within the data acquisition window. Second, data sampling occurs during the plateau period of the readout gradient, thereby avoiding image distortion artifacts associated with ramp sampling. Furthermore, off-center imaging is more straightforward to achieve with ZTE. A typical ZTE pulse sequence diagram is shown in Figure 1.4.

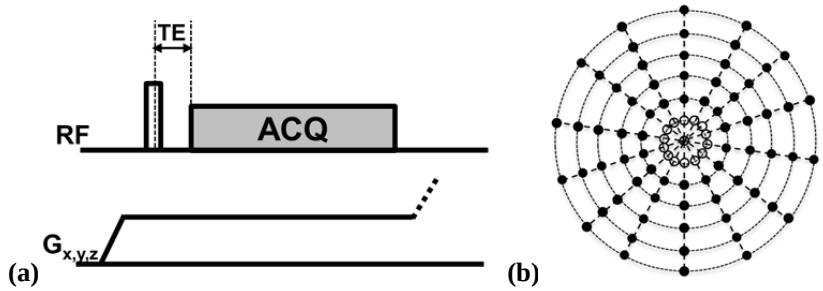

Figure 1.4 (a) Pulse sequence diagram for ZTE encoding. The imaging gradient $G_{x,y,z}$ is turned on before RF excitation. The data acquisition starts immediately after the dead time. (b) The corresponding trajectory. The solid dots represent the acquired k-space samples and the hollow circles denote the missing samples.

A common problem with ZTE is that the central *k*-space portion is missed due to the dead time between RF transmission and data acquisition. In order to recover the missing central *k*-space samples, several methods have been proposed, including algebraic reconstruction (10,21), acquisition of additional radial projections with lower gradient strength (WASPI: water- and fat-suppressed proton projection MRI) (8), or performing a complementary single-point imaging (SPI) scan (PETRA: pointwise encoding time reduction with radial acquisition) following the main body of the sequence (9).

Another well-known problem is the presence of the spatial encoding gradient during hard pulse excitation, causing the RF pulse to become spatially selective and resulting in blurring and shadow artifacts. The problem is negligible on laboratory imaging systems

which allow high peak power and thus very short pulse duration. However, B_1 peak power and specific absorption ratio (SAR) limitations impose practical limits for *in vivo* scanning of humans (22). Recently, Grodzki et al. investigated the effects of the sinc-shaped excitation profile in PETRA and proposed an approach to correct for the resulting image artifacts (23). However, their correction algorithm requires that the imaged object fit into the sphere defined by the main lobe of the sinc-shaped excitation profile. If these conditions are not met the amplified noise resulting from inversion of the ill-conditioned matrix rooted from the zero crossings of the sinc function will corrupt the resulting image. Chapter 3 will present a detailed analysis of the artifacts and describe a new algorithm for correcting them.

1.2.3 SWIFT

In conventional MRI pulse sequences, including UTE and ZTE sequences, excitation and acquisition are separated. In contrast, SWIFT excites spins and acquires signal nearly simultaneously (11), which allows echo times close to zero. Although ZTE is able to achieve the same echo time as SWIFT, it requires the excitation pulse to have a broad bandwidth to uniformly excite the spins across the whole FOV, which in turn limits the attainable flip angle due to the extremely short pulse duration and limited B1 peak power. SWIFT overcomes this limitation by using a frequency-swept pulse which covers the entire bandwidth spanned by the imaging gradient without B1 peak power limitation (11). In theory, it is possible to achieve arbitrary bandwidth with limited RF amplitude and without compromising the flip angle in SWIFT.

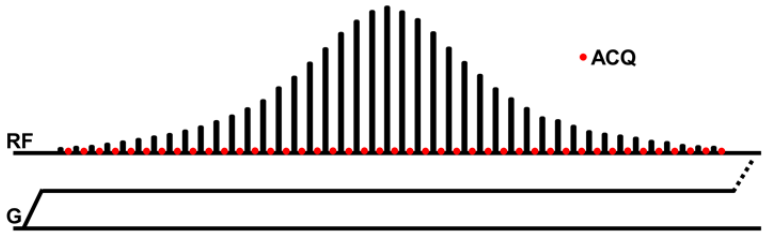

Figure 1.5 Pulse sequence diagram of SWIFT. A frequency sweep pulse is divided into sub-pulses, which interleave with the data acquisition (red dots). By using a frequency-modulated pulse, SWIFT is able to excite spins with a broad frequency band without compromising the optimal flip angle.

Due to the overwhelming voltage/signal from transmission compared with MRI signal level, the original SWIFT is operated in a time-share mode which interleaves between transmission and acquisition (24), therefore compromising SNR, which is roughly proportional to the square root of the transmission duty cycle. Fig. 1.5 shows the pulse sequence diagram of SWIFT sequence. In (10), Weiger et al. compared the gapped SWIFT and ZTE imaging with optimized protocols under clinical scanner hardware constraints, and concluded ZTE to yield higher SNR efficiency as well as shorter scan times than gapped SWIFT. More recently, Idiyatullin et al. achieved the transmitter-receiver isolation by connecting a quad coil to a quadrature hybrid, therefore minimizing the leakage signal from transmitter and allowing SWIFT to be operated in the continuous mode (25). Continuous SWIFT has the potential to achieve higher SNR efficiency than its gapped counterpart. However, unlike UTE and ZTE imaging, a dedicated coil may be needed for the implementation of SWIFT on a clinical scanner, perhaps the main obstacle to its usage as a routine short-T_2 imaging sequence on a whole body imager.

1.2.4 Other Short-T_2 Imaging Sequences

The single point imaging (SPI) method is another technique for imaging short T_2 species (26,27). Without using the common frequency encoding, SPI is a pure phase

encode pulse sequence. During each repetition, the RF is applied simultaneously with the imaging gradient and only a single *k*-space sample is acquired after the dead time. Due to its fixed echo time, SPI is free of the image blurring due to T_2 decay during the frequency-encoding period. Moreover, it is immune to B_0 inhomogeneity, chemical shift, and susceptibility variations (28). However, acquisition is inefficient since only one *k*-space point is acquired for each gradient switch on/off.

SPRITE (Single point Ramped Imaging with T1 enhancement) improves SPI acquisition efficiency by employing ramped phase encode gradient which permits image acquisition with less frequent gradient switching (29). However, the sampling is still inefficient. To further shorten scan time, multipoint *k*-space mapping samples a *k*-space line segment of **r** points per TR cycle, thereby accelerating the acquisition speed by a factor of **r** (30,31). Even though SPI and its variants minimize the T_2 decay effect, their usage in short-T_2 imaging is still limited by the method's relatively long scan time.

1.3 Cortical Bone Water

Although BW and myelin are unrelated to each other biologically, they share similar MRI properties, i.e. very short lifetime of the MR proton signals undetectable by conventional MRI with *TE*s of several milliseconds or longer. The remainder of this chapter briefly reviews research works on imaging of cortical bone water and myelin.

Cortical bone water (BW) can be categorized into two pools: pore water resides in the spaces of the Haversian and lacuno-canalicular pore system, while there is a significant water fraction bound to collagen (32-34). Recent work based on proton NMR transverse relaxation spectroscopy in human cortical bone specimens suggests that

approximately two thirds of the total bone water signal arises from collagen-bound water and one third from pore water, with the two constituents differing in T_2 relaxation time (32). The restricted motion of bound water by hydrogen bonding to the collagen backbone gives rise to its short T_2 values of around 400 μs. The pore water protons have relatively longer T_2, ranging from 1 ms to a few seconds, since their rotational and translational motion is unimpeded.

Cortical bone porosity, i.e. pore volume fraction, increases with advancing age and this process is further accelerated osteoporosis (35). Increasing in pore volume is a major cause of impaired strength of osteoporotic cortical bone (36,37). McCalden et al. found ultimate stress, ultimate strain, and energy absorption, to decrease by 5, 9, and 12 percent per decade, respectively (38). However, there is no strong evidence that the intrinsic mechanical properties of osteoporotic bone are different from those of normal bone. Rather, the impaired strength of osteoporotic cortical bone is a consequence of increased pore volume fraction (37). However, pore architecture is not directly observable by current imaging modalities *in vivo*. Instead, indirect method for porosity estimation needs to be used for *in vivo* studies. Since the pore water occupies the pore network of cortical bone, its concentration scales with pore volume. Hence, if pore water could be quantified, it would be possible to estimate porosity indirectly without a need to spatially resolve the pores.

Although the bone signal is undetectable with conventional MRI sequences, recent advances in MRI of short-T_2 tissues enables to detect and quantify the proton signals from human BW (6). However, conventional UTE imaging only measures the total BW

concentration, including both collagen-bound and pore water, which may be a less than optimal measure of bone porosity. This prompted research toward design of methods to separate the two bone water fractions. Recent work suggests that such separation may be achievable by exploiting the hypothesized differences in T_2* between the two water populations (39,40). Du et al. accomplished this goal via bi-exponential analysis of the UTE MRI signal decay measured from a series of UTE images with a range of echo-times (39,41). Horch et al. proposed methods using adiabatic single or double-inversion pulses as a means to obtain images displaying signal from predominantly bound or pore water, respectively (42). The same group also showed that the collagen-bound water was strongly positively correlated with peak stress while the fraction comprising longer-T_2 values (T_2 ~ 1-1,000ms), assigned to free water presumably residing in pore spaces, was negatively correlated with peak stress (43). Chapter 4 will introduce suppress ratio derived from long-T_2 suppressed UTE imaging, as a surrogate biomarker of cortical bone porosity.

1.4 Myelin

Myelin is another important short-T_2 tissue constituent. It is essential for proper functioning of the central nervous system (CNS) and accounts of 14% of the wet mass of white matter. It is a lipid-protein bilayer that extends from the outer membrane of glial cells, and discretely winds around individual axonal fibers acting as an insulator preventing loss of charge and leading to an increase in conduction velocity (6). Myelin pathology is one of the major causes of neurological diseases and deficiencies of myelin lay at the core of many demyelinating disorders, such as multiple sclerosis (6). Therefore,

the ability to measure myelin density noninvasively would have a major impact on diagnosis and evaluation of diseases that are responsible for much of CNS morbidity. Assessment of myelin may also provide insight into the function of oligodendrocytes since they shield axons with myelin membrane and also provide trophic support to the neurons (44-46). Hence, better capabilities for monitoring myelin status would further provide indirect evidence of glial status, and hence neuronal integrity.

To observe and quantify myelin, the common methods rely on histology-based optical microscopy (47), X-ray diffraction (48) or non-linear optical techniques (49,50). Unfortunately, all these techniques are destructive and thus applicable only to animal studies. During the past two decades MRI has made significant progresses toward detection of myelin abnormalities, mostly via magnetization transfer (MT) imaging based on the interaction between myelin and tissue water, yielding the magnetization transfer ratio (51,52) or quantities such as the bound proton fraction derived from a more detailed model-based analysis of the MT data (53,54). Another approach relies on detection of myelin water, which is interspersed between adjacent myelin lipid bilayers, and identified based on its T_2 relaxation properties (55,56). However, this reliance may be compounded by non-myelin loss related changes, for example, inflammation (57,58). Both methods are indirect, i.e. providing surrogate measures of myelin content (59), rather than detecting myelin itself, and the underlying biophysical mechanisms are not well understood. Therefore, direct detection of myelin with MRI would remove these complications and may provide contrast specific to myelin concentration.

Ramani et al. investigated the T_2 relaxation properties of myelin proton by using a multi-exponential fit of spin-echo decays on fixed human white matter samples from

normal and multiple sclerosis patients, concluding myelin protons have a T_2 value of ~50 μs (60). Recently, Horch et al. showed that these ultra-short T_2 signals are predominantly from methylene ^{1}H, originating from phospholipid membranes and various intracellular and extracellular proteins and reported T_2* and T_2 relaxation times of myelin proton with values of ~70 μs and between 50 to 1000 μs, respectively (61). More recently, the author's laboratory first showed that direct myelin imaging is feasible with UTE imaging with long-T_2 suppression on a 9.4 T spectrometer (1). In Chapter 6, the feasibility of direct detection of myelin with the developed short-T_2 imaging techniques will be further explored on clinical scanners.

1.5 Dissertation Outline

This thesis research aims to address some existing problems in UTE and ZTE imaging sequences and help establish them as routine solid-state pulse sequences on a clinical MRI imager with a focus on direct detection and quantification of cortical BW and myelin. The dissertation is organized as follows. In Chapter 2, the imaging parameters of three long-T_2 suppression techniques in UTE imaging are optimized and their performance is compared *in vivo* in the lower extremities of test subjects. Chapter 3 presents a method to correct the image artifacts in ZTE imaging caused by the spatial selectivity of the hard excitation pulse by applying quadratic phase-modulated excitation pulse and iterative reconstruction. In Chapter 4, the scan time of UTE and ZTE sequences is reduced by applying compressed sensing method and anisotropic FOV trajectory. In the remainder of the dissertation, applications of UTE and ZTE imaging to cortical bone water and myelin quantification are demonstrated. Chapter 5 describes a new biomarker,

suppression ratio in UTE imaging, as a surrogate measure of cortical bone porosity. Chapter 6 explores the feasibility of direct myelin quantification with long-T_2 suppressed ZTE imaging with a clinical scanner setup. Finally, Chapter 7 concludes the dissertation with a summary of this thesis research work and a brief discussion of future work.

Chapter 2 UTE Imaging with Soft Tissue Suppression

2.1 Abstract

Ultra-short echo time (UTE) imaging reveals short-T_2 components (typically hundreds of microseconds to milliseconds) ordinarily not captured or obscured by long-T_2 tissue signals on the order of tens of milliseconds or longer. However, since long-T2 tissues also give signal during UTE imaging it is critical to suppress these components. If this suppression is successful, the technique enables visualization and quantification of short-T_2 proton signals such as those in highly collagenated connective tissues. In this chapter, the performance of the three most commonly used long-T_2 suppression UTE sequences, i.e. echo subtraction (dual-echo UTE), saturation via dual-band saturation pulses (dual-band UTE), and inversion by adiabatic inversion pulses (IR-UTE) is compare at 3T, via Bloch simulations and experimentally *in vivo* in the lower extremities of test subjects. For unbiased performance comparison, the acquisition parameters are optimized individually for each sequence to maximize short-T_2 SNR and CNR between short- and long-T_2 components. Results show excellent short-T_2 contrast is achieved with these optimized sequences. A combination of dual-band UTE with dual-echo UTE provides good short-T_2 SNR and CNR with less sensitivity to B_1 homogeneity. IR-UTE has the lowest short-T_2 SNR efficiency but provides highly uniform short-T_2 contrast and is well suited for imaging short-T_2 species with relatively short T_1 such as bone water.

2.2 Existing Soft Tissue Suppression Techniques

As discussed in last chapter, UTE imaging is able achieve effective TEs of 100 μs or less depending on the MR system hardware, thereby capturing a significant portion of the

signal arising from short-T_2 nuclei. Although short-T_2 species become detectable in UTE imaging, their signals are often obscured by the much more intense signals of the surrounding long-T_2 components, which usually have far higher proton density. To better visualize the short-T_2 protons, long-T_2 suppression techniques are commonly employed in UTE imaging (12). Generally, the goal of long-T_2 suppression is to maximize suppression of the long-T_2 components while preserving the short-T_2 components. Several methods have been proposed for soft-tissue suppression and short-T_2 species contrast enhancement which can be categorized into two types: a combination of different TEs, or some form of magnetization preparation involving either saturation or inversion nulling.

The first type is perhaps the most common and the simplest, in which an image obtained with longer TE, containing signal principally from long-T_2 protons only, is subtracted from a short-TE image (12). The main benefit of this approach is that it is simple and can easily be incorporated into 2D and 3D UTE sequences without significant sequence modification or increase in scan time. However, T_2* losses and SNR reduction from the subtraction operation may degrade the quality of soft-tissue suppression. The first of the magnetization preparation based soft-tissue suppression techniques was proposed by Pauly et al. (62), i.e. T_2-Selective RF Excitation Contrast or TELEX, in which a long rectangular $\pi/2$ saturation pulse is applied followed by a spoiler gradient preceding short RF pulse excitation. The long saturation pulse selectively excites the long-T_2 species while leaving the short-T_2 components largely unperturbed since their decay rate exceeds the excitation rate. An improved version of this technique, referred to as refocused TELEX (63), reduces the sensitivity of the original method to B_0

inhomogeneity by interrupting the long π/2 pulse using a series of short refocusing pulses to broaden the bandwidth of the saturation pulse. However, the performance of this approach varies with T_1/T_2.

Recently, several research groups reported various improved long-T_2 suppression methods (64-68), based either on saturation or inversion pulses. Larson et al. designed single-band and dual-band maximum-phase saturation pulses (65) using the Shinnar-Le Roux (SLR) design tools with complex Parks-McClellan algorithm (69). The beneficial feature of SLR design algorithm is that the designer has the freedom to specify the pulse parameters, such as pulse duration, suppression bandwidth and desired ripple values for each band. These saturation pulses created good short-T_2 contrast at 1.5 T. However, they are sensitive to B_1 inhomogeneity, causing nonuniform soft-tissue suppression. To overcome the sensitivity to B_1 field variation, long adiabatic inversion pulses can be employed to invert the long-T_2 components, while affecting to a lesser extent the short-T_2 species, then followed by UTE acquisition at the null point of the long-T_2 components (12). Recently, two variants of this approach have appeared. Larson et al. used phase-sensitive inversion recovery at 1.5 T to allow UTE acquisition immediately after the adiabatic inversion pulse by combining the images with inversion preparation with those collected without preparation pulses (66). Du et al. proposed dual inversion-recovery UTE (DIR-UTE) (67) in which two long adiabatic inversion pulses centered on the water and fat resonance frequencies are applied to account for the T_1 difference between water and fat.

Other magnetization-preparation based soft-tissue suppression methods exist as well. In work performed on a 4.7 T small-bore system, Wu et al. used two long rectangular $\pi/2$ pulses placed on resonance with fat and water, executed with and without π pulses in two successive scans added to cancel the effect of $\pi/2$ pulse imperfections in what they termed water- and fat-suppressed proton projection MRI (WASPI) (8,64). However, because of the greater B_1 variation on a clinical scanner and doubled imaging time due to the need for two scans, only two long rectangular $\pi/2$ pulses were applied in this more recent implementation of the WASPI technique (70). Thus, the long-T_2 suppression portion of this embodiment of WASPI is essentially identical to TELEX. Du et al. conceived the technique called UTE with off-resonance saturation contrast (UTE-OSC) (68), in which two images with and without application of a high-power off-resonance saturation pulse are acquired. Short-T_2 contrast is achieved by subtraction of the two images. One possible problem with this approach is that the subtraction operation and magnetization transfer effect may impair the effectiveness of long-T_2 suppression.

Given the many long-T_2 suppression schemes available, comparison of their performance would provide insight and guide their use in research and clinical applications. Although several research groups compared some soft-tissue suppression approaches (71,72), these comparisons were not based on optimal imaging protocols and the results therefore were not conclusive.

This work compared the performance of the three most commonly used soft-tissue suppression schemes, echo subtraction using two different TEs (termed as dual-echo UTE), saturation via dual-band saturation pulses (dual-band UTE) and inversion by

adiabatic inversion pulses (IR-UTE) at 3T, via Bloch equation simulations and experimentally *in vivo* in the lower extremities of test subjects. The strategy adopted that allows for unbiased performance comparison entails optimization of the acquisition parameters individually for each method to maximize short-T_2 SNR and CNR between short- and long-T_2 components. Based on the outcome of these experiments for the target short-T_2 tissues (bone and tendon), the performance of the various methods examined was quantitatively evaluated.

2.3 Image SNR of Long-T_2 Suppressed UTE Sequences

For unbiased comparison of the various soft-tissue suppression methods, the acquisition parameters for each of the three pulse sequences need to be optimized to maximize SNR of short-T_2 species and CNR between short- and long-T_2 components. SNR efficiency (SNR_{eff}) is defined as image SNR normalized by the square-root of total scan time for the purpose of comparing sequences with different imaging times. Image SNR depends on field strength, T_1, T_2, voxel dimensions, pulse sequence type and timing parameters, and total sampling time. Since the long-T_2 suppression methods are variants of the original UTE sequence, the imaging parameters to be optimized reduce to a small set, including TR, flip angle of the half excitation pulse and magnetization preparation pulses, with all other parameters being held constant. The following subsections describe each pulse sequence and the relevant parameters for optimizing long-T_2 suppression and short-T_2 SNR_{eff}.

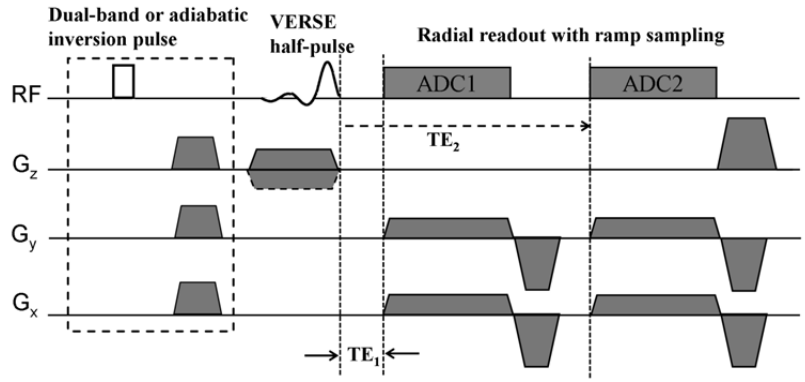

Figure 2.1 2D UTE pulse sequence with soft-tissue suppression. In dual-echo UTE two identical half-radial projections differing in echo time are acquired after each half-pulse excitation. The dashed box indicates the magnetization-preparation portion of long-T_2 suppression, in which a dual-band pulse (dual-band UTE) or adiabatic inversion pulse (IR-UTE) followed by a spoiler gradient is applied before standard UTE acquisition. For IR-UTE, an inversion time (not shown here) is inserted to null the longitudinal magnetization before UTE acquisition.

2.3.1 Dual-echo UTE

Dual-echo UTE is the most commonly used method for soft-tissue suppression. As shown in the pulse sequence diagram (Fig. 2.1), two identical half radial projections differing in echo times are acquired after each half-pulse excitation. The long-TE image, containing signal predominantly from long-T_2 species, is subtracted from the first echo image, which contains both long and short-T_2 species. The resulting difference creates an image highlighting the short-T_2 tissue components. Assuming that the magnetization reaches the steady state and there is negligible short-T_2 proton signal in the second TE image, SNR_{eff} of short-T_2 species in dual-echo UTE can be written as:

$$SNR_{eff} \propto f_{xy} \frac{1-\exp(-TR/T_1)}{\sqrt{2}(1-f_z \exp(-TR/T_1))\sqrt{T_{acq}}} \quad [1]$$

where f_{xy}, f_z representing the normalized transverse and longitudinal magnetizations in response to the excitation pulse (63) deviate from the usual sine and cosine terms of the flip angle due to the evolution of the magnetization during the finite duration of the

pulse relative to T_2, and need to be numerically evaluated from the Bloch equations. T_{acq} is the total sampling time, which is proportional to *TR*. The factor $\sqrt{2}$ results from the subtraction operation.

2.3.2 Dual-band UTE

Dual-band UTE involves magnetization-preparation based soft-tissue suppression, in which a long dual-band saturation pulse is played out before the UTE acquisition in order to suppress the long-T_2 species. The dual-band pulse has two spectral saturation bands at water and fat resonances, which can be designed using SLR algorithm with complex Parks-McClellan algorithm (65,69). Since lipid protons have multiple resonance peaks and relaxation times considerably shorter than those of water protons, the optimal flip angle of the saturation pulse for fat may be different from water. Therefore, the flip angles for both water and fat were included as design variables, along with the pulse duration, filter order, fat resonance frequency, desired ripple values and suppression bandwidth corresponding to the range of the off-resonance frequencies. Considering the effect of dual-band pulse on short-T_2 species, SNR_{eff} can be expressed as follows, assuming magnetization is in the steady state:

$$SNR_{eff} \propto f_{xy} \frac{f_{z,dualband}(1-\exp(-(TR-T_{dualband})/T_1))}{(1-f_{z,dualband} f_z \exp(-(TR-T_{dualband})/T_1))\sqrt{T_{acq}}} \quad [2]$$

where $f_{z,dualband}$ is the normalized longitudinal magnetization in response to the dual-band pulse. This can be calculated by numerical solution of the Bloch equations. Quantities f_{xy}, f_z and T_{acq} have previously been defined, and $T_{dualband}$ is the dual-band pulse duration. From Eq.2, one can see that the SNR of short-T_2 species depends on the dual-

band saturation pulse, the excitation pulse and *TR*. Since the dual-band pulse has already been designed to maximally suppress the long-T_2 components, its saturation effect on short-T_2 species could be predetermined by the Bloch equation evaluation prior to optimizing the excitation pulse and *TR*.

2.3.3 IR-UTE

IR-UTE is a soft-tissue suppression method in which a long adiabatic pulse inverts the long-T_2 components while only slightly perturbing the short-T_2 protons, followed by UTE acquisition at the null point of the long-T_2 components. This method is relatively immune to spatial B_1 variations because of the properties of adiabatic pulses. A potential difficulty with IR-UTE is achieving simultaneous nulling of both types of protons given the significantly different T_1 relaxation times of water and fat protons. However, it turns out that for TR < T_1 optimal inversion delays for water and fat are close (i.e. differing by a few milliseconds), thereby resulting in negligible residual longitudinal magnetization at the time-point of sampling the UTE signal. Including the effect of the adiabatic inversion pulse and assuming the magnetization to have reached a steady state, SNR_{eff} for the short-T_2 protons is calculated according to:

$$SNR_{eff} \propto f_{xy} \frac{1-(1-f_{z,inv})\exp(-TI/T_1)-f_{z,inv}\exp(-(TR-T_{inv})/T_1)}{(1-f_{z,inv}f_z\exp(-(TR-T_{inv})/T_1))\sqrt{T_{acq}}} \quad [3]$$

In Eq. 3 $f_{z,inv}$ is the normalized longitudinal magnetization of the short-T_2 protons in response to the adiabatic inversion pulse. T_{inv} is the adiabatic inversion pulse duration. *TI* is the inversion time, defined as the time interval between the end of the adiabatic pulse and the start of the half-sinc pulse. Short-T_2 SNR is a function of the inversion pulse, TI,

excitation pulse and TR. The inversion pulse, TR and TI are optimized to suppress the long-T_2 species. The effect of the adiabatic inversion pulse on short-T_2 components was evaluated by numerically solving the Bloch equations, and the optimal flip angle of the excitation pulse was determined from Eq. 3.

2.4 Imaging Protocol Optimization

For each of the three sequences, the adjustable parameters described above were first optimized to maximize soft-tissue suppression, including TE_2 (dual-echo UTE), dual-band pulse (dual-band UTE), and adiabatic inversion pulse, TR and TI (IR-UTE), The imaging parameters were then chosen to maximize short-T_2 SNR_{eff}. After initially optimizing the imaging parameters for each sequence via Bloch equation simulations, the optimized sequences were used to acquire *in vivo* images for cortical bone and Achilles tendon, and SNR and CNR of the three sequences were compared to evaluate their performance.

2.4.1 Tissue Parameters

To optimize the imaging parameters for each sequence, the relaxation times for the target tissue components needed to be determined first as input parameters for the Bloch equation simulations and computation of SNR. Although there is significant age dependence of relaxation times in cortical bone and Achilles tendon (for example, in cortical bone as a result of porosity and pore size (3)), the typical T_1 and T_2 relaxation times used in the optimization procedures were: $T_{1,bone}$ = 200 ms, $T_{2,bone}$ = 420 μs (73), $T_{1,tendon}$ = 600 ms, $T_{2,tendon}$ = 1 ms (74,75).

2.4.2 Imaging Parameter Optimization

The critical variable determining the effectiveness of soft-tissue suppression in dual-echo UTE is the second TE, which needs to be chosen to allow adequate short-T_2 signal decay while minimally affecting the long-T_2 components. To avoid signal cancellation from long-T_2 components with different chemical shifts, the water and fat methylene resonances should be in phase at TE_2, i.e., at an integer multiple of 2.3 ms at 3T. The durations for sampling of the first echo and readout rewinding gradients limit TE_2 to a minimum of 4.6 ms.

For dual-band UTE, the dual-band pulse must be optimized to achieve maximal soft-tissue suppression. As stated in the theory section, the optimal flip angle of the saturation pulse for fat may differ from that for water. To determine optimal saturation pulse flip angles, a series of conventional dual-band pulses were first designed with flip angles from 80^o to 130^o degrees in steps of 5^o. These preparation pulses were then incorporated into a spoiled gradient echo sequence to image a phantom consisting of containers of distilled water doped with 0.09 mM $MnCl_2$ and 0.2M NaCl and vegetable oil with the following parameters: FOV = 200×200 mm^2, slice thickness of 5 mm, matrix size = 256×256, TR = 200 ms, TE = 4 ms. SNR of both water and fat images were calculated and plotted as a function of the flip angle of the dual-band saturation pulse. As suggested in Fig. 2.2, the optimal flip angle to produce minimal water signal is 100^o, while for fat it is 110^o. Once the optimal flip angles for water and fat were obtained, a dual-band pulse with different flip angles on water and fat bands was designed using the SLR and complex Parks-McClellan algorithms. The design function was derived from Larson et al.'s dual-band pulse design function (65), which includes flip angles for water and fat,

pulse duration, filter order, fat resonance frequency, desired ripple values and suppression bandwidths as input design parameters. A pulse duration of 15 ms, filter order of 300, flip angles of 100° for water and 110° for fat, suppression bandwidths of 120 Hz on resonance and 320 Hz at the fat resonance centered at -430 Hz at 3T, and ripple values of 0.5% were chosen for all the *in vivo* experiments. To validate the performance of the dual-band pulse, its off-resonance and T_2 profiles were evaluated using matrix-form Bloch equation simulation (76). For off-resonance simulation, T_2 = 100 ms, T_1 = 1 s were used with frequencies between -800 Hz and 400 Hz relative to water protons.

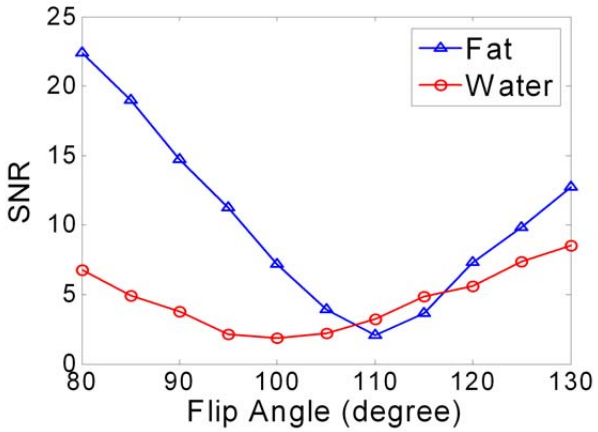

Figure 2.2 SNR for doped water and vegetable oil vs. flip angle of the conventional dual-band pulse. The optimum flip angles are different for water (100 degrees) and fat (110 degrees), reflecting their different relaxation times and spectral bandwidths.

The adiabatic inversion pulse, TR and TI are the parameters to be optimized to suppress the long-T_2 species in IR-UTE. A hyperbolic secant (HS) adiabatic inversion pulse was used in all *in vivo* experiments. To minimize bone water suppression and maximally suppress the long-T_2 components, the HS pulse was optimized as follows: 1) Pulse bandwidth/duration = 1 kHz/20 ms, with a frequency shift of 270 Hz towards the lipid peak in order to cover both fat and water peaks; 2) The frequency was swept from

higher to lower frequency, inverting water before fat to compensate for the longer T_1 of water; 3) The HS pulse amplitude was set to allow 30% B_1 variation. Bloch equation simulations were performed to evaluate the off-resonance and T_2 profiles of the HS pulse and overall performance. T_2 = 100 ms, T_1 = 1 s were used in the off-resonance simulation. Water and fat longitudinal magnetizations could not be completely nulled simultaneously because of their very different T_1 values. However, as pointed out previously, their null time points (i.e. TIs), are relatively close when TR is short and the magnetization has reached a steady state. Based on Ref. (77) and of some of the authors' previous work (78), a combination of TR = 300 ms and TI = 100 ms is a good balance between short-T_2 SNR and long-T_2 suppression.

After the soft-tissue suppression related parameters were determined, other imaging parameters were optimized to maximize the SNR_{eff} of the target short-T_2 species for each sequence according to Eqs. 1-3. The effects of dual-band pulse, HS pulse and half excitation pulse were calculated by Bloch equation simulation. The parameters of the dual-band and HS pulses have been described above. The parameters for the Hamming filtered half-sinc variable rate-selective excitation (VERSE) pulse (15) were as follows: pulse duration = 830 μs with 580 μs played out at the plateau and 250 μs at the ramp-down of the slice selection gradient (bandwidth = 4258 Hz creating 5mm slice thickness with 20 mT/m slice selection gradient). For dual-echo UTE and dual-band UTE, TR and flip angle of the half excitation pulse were optimized, while in IR-UTE, only the optimal flip angle of the half excitation pulse needs to be determined. In the case where the optimal excitation flip angle was close to 90^o, the half-sinc pulse was replaced by a half-

SLR pulse (79) in the subsequent *in vivo* scans as a means to improve the slice profile. All pulse design tasks, simulations and optimizations were implemented with MATLAB (Mathworks, Natick, MA, USA) using in-house programs.

2.4.3 Human Subject Studies

All *in vivo* MRI scans were performed at 3T (TIM Trio; Siemens Medical Solutions, Erlangen, Germany). The mid-tibia (38% site as measured from the lateral malleolus) and Achilles tendon of five healthy volunteers (age range: 24-40 years; gender: 3 males and 2 females) were imaged with all the three sequences. The protocol for this study was approved by the Institutional Review Board and informed written consent was obtained for each participant. The same scan parameters were used for the UTE acquisition portion of the three sequences to ensure unbiased comparison (slice thickness = 5 mm, TE_1/TE_2 = 60 μs/4.6 ms). For the dual-TE sequence 2000 ramp-sampled half-radial projections were acquired (corresponding to 24% oversampling) to achieve adequate SNR considering the short TR (20 ms). For the other two sequences (dual-band and IR-UTE) only 500 projections were acquired (corresponding to an undersampling factor of 3.2) in order to reduce total scan time, given the much longer TR required by these sequences (see Table 1). Note here that the superior long-T_2 suppression tolerates some undersampling without causing apparent streaking artifacts. In order to drive the magnetization to steady state, 40 dummy scans were performed before data acquisition. For the mid-tibia, an 8-channel transmit-receive knee coil was used with FOV = 180×180 mm^2, sampling frequency bandwidth = ±83.3 kHz, 268 readout points for each half radial projection resulted in a reconstructed matrix size of 512×512 and image resolution 0.35×0.35 mm^2. The Achilles

tendon was imaged with a 4-channel receive-only ankle coil (Insight MRI, Boston, MA) with FOV = 120×120 mm^2, sampling frequency bandwidth = ±62.5 kHz, 205 readout samples for each half radial projection, reconstructed matrix size = 384×384 and pixel size = 0.31×0.31 mm^2. The body coil was used for RF transmission. To avoid confounding effects from the angle dependence of the collagen-bound water, the subjects were positioned horizontal and supine to ensure collagen fibers in the tendon aligned with the main magnetic field (80). Other acquisition parameters are listed in Table 2.1.

	Cortical Bone	**Tendon**
dual-echo UTE	TR = 20 ms, FA = 25°	TR = 20 ms, FA = 15°
dual-band UTE	TR = 240 ms, FA = 75°	TR = 500 ms, FA = 76°
IR-UTE	TR = 300 ms, TI = 100 ms, FA = 87°	TR = 300 ms, TI = 100 ms, FA = 89°

Table 2.1 Imaging parameter sets for dual-echo UTE, dual-band UTE and IR-UTE used in the in vivo experiments.

2.4.4 Image Reconstruction and Analysis

The acquired *k*-space data were remapped onto Cartesian grids using Greengard's regridding algorithm (17) before applying 2D IFFT. Prior to gridding, sampling density compensation weighting was performed. The weighting was calculated based on the gradient mapping (20) which measured the *k*-space trajectories. The final magnitude image was synthesized as the square-root of the sum-of-squares of the multi-coil images. The subtracted image was reconstructed as the magnitude image difference between the short- and long-TE images. The image reconstructions were implemented with MATLAB.

To quantitatively assess the performance of dual-echo UTE, dual-band UTE and IR-UTE, short-T_2 SNR and CNR were calculated. SNR was calculated as the ratio of the

mean magnitude image intensity inside a user-defined region of interest to the standard deviation of the background signal. Typical regions of interest included more than 100 pixels. CNR was calculated as the difference between SNR of the tissue components of interest. For comparing sequences with different scan times, SNR was normalized by the square-root of total scan time to obtain *relative* SNR_{eff} with dual-echo UTE as the reference. The ratio of short-T_2 SNR to surrounding long-T_2 SNR was also calculated as a quantity measuring the level of short-T_2 retention and long-T_2 suppression.

2.5 Simulation and Experimental Results

The off-resonance and T_2 profiles of the designed dual-band pulse are shown in Fig. 2.3. The dual-band pulse generates flip angles at water and fat bands of 100^o and 110^o, respectively (Fig. 2.3b). Since the bandwidth was designed large enough to compensate for field inhomogeneity and to cover the broad fat spectrum at 3T, its saturation effect on short T_2 species becomes substantial. The dual-band pulse is predicted to saturate 40% of cortical bone water (T_2 = 420 μs) and 60% of the tendon water protons (T_2 = 1 ms). Fig. 2.4 shows the off-resonance and T_2 profiles of the designed HS adiabatic pulse. As illustrated in Fig. 2.4b, a variation in RF amplitude by ±30% has negligible effect on the spectral profile of the pulse, demonstrating its insensitivity to B_1 inhomogeneity. However, Fig. 2.4c shows that short-T_2 signals are significantly attenuated. The residual longitudinal magnetizations of cortical bone water and tendon protons are on the order of 5% only immediately after the HS adiabatic pulse. Further, as T_2 shortens, the HS pulse gradually loses its insensitivity to B_1 variations (81).

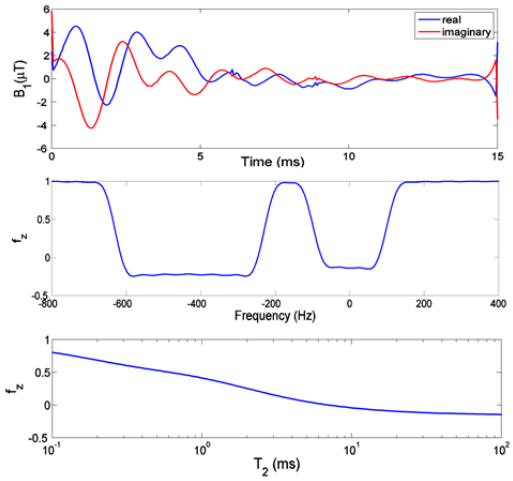

Figure 2.3 Bloch equation simulations of (a) 15 ms dual-band pulse. (b) Off-resonance profile for T_2 = 100 ms, T_1 = 1 s. The dual-band pulse had a suppression bandwidth of 120 Hz with flip angle of 100o on resonance with water and bandwidth of 320 Hz with flip angle of 110^o at the fat resonance centered at -430 Hz. (c) On-resonance T_2 profile. Due to the increased suppression bandwidth at 3T, 40% of cortical bone water (T_2 = 420 μs) and 60% of the tendon signal (T_2 = 1ms) are saturated.

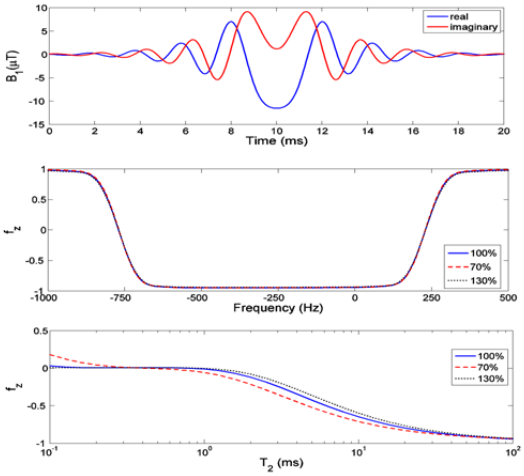

Figure 2.4 Bloch equation simulations of (a) 20 ms HS pulse with bandwidth of 1 kHz. (b) Off-resonance profile for T_2 = 100 ms, T_1 = 1 s. The HS pulse is shifted 270 Hz towards the lipid peak to cover both fat and water peaks. The solid line was calculated at the desired B_1 amplitude. The dashed and dotted lines correspond to 70% and 130% of the desired amplitude, respectively. For B_1 variations of up to 30% the frequency profile of the HS pulse changes negligibly. (c) On-resonance T_2 profile: less than 5% longitudinal magnetization remains for protons with $T_2 \leq 1$ ms upon application of the HS adiabatic pulse.

The normalized theoretical SNR_{eff} of both cortical bone and tendon, as a function of *TR* for all three sequences, is shown in Figs. 2.5a and b, respectively. Imaging parameters used in the *in vivo* scans are indicated by markers in the figure. For each TR value the

SNR_{eff} was calculated at the optimal flip angle of the excitation pulse. In IR-UTE, to obtain the SNR_{eff} dependence on TR, TI is selected as the time point for which the magnitude sum of fat and water signals achieves a minimum at a given TR. However, it is noted that the extent of soft-tissue suppression is TR dependent. For dual-band UTE, TR of 500 ms was used instead of optimal TR around 750 ms for tendon imaging, to trade off SNR efficiency gain and scan time.

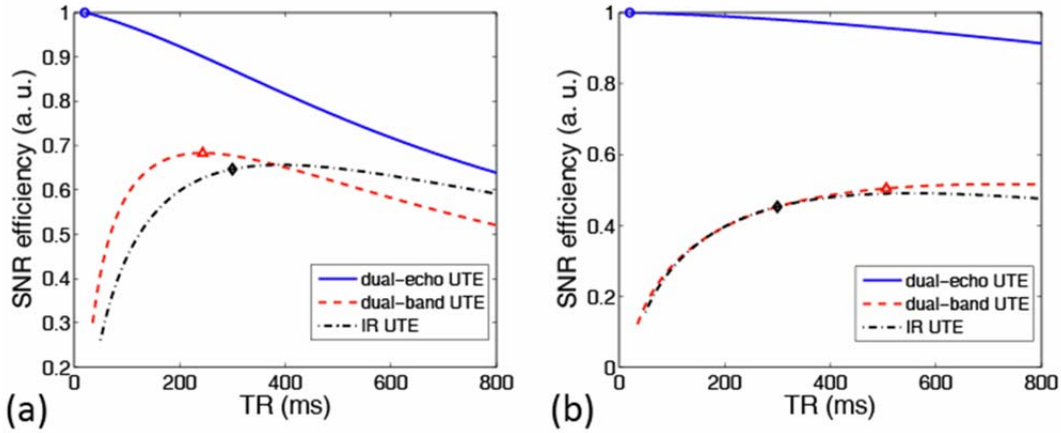

Figure 2.5 Normalized theoretical SNR efficiencies for (a) cortical bone and (b) tendon as a function of *TR* for the three sequences. Short-T_2 SNR efficiency is highest for dual-echo UTE (solid line) but generally lower for dual-band UTE (dashed line) and IR-UTE (dashed-dotted line) due to perturbation of the spin system by the magnetization preparation pulses. The imaging parameters used in the *in vivo* scans are indicated by markers: circle: dual-echo UTE; triangle: dual-band UTE; diamond: IR-UTE.

Fig. 2.6 displays a representative comparison of left mid-tibia images from a 26-year-old healthy male volunteer using the three soft-tissue suppression methods with optimized image protocols. Fig. 2.6a shows the first echo image of dual-echo UTE in which the contrast between cortical bone and the surrounding tissue is poor. In dual-echo UTE (Fig. 2.6b), although the muscle signal is well suppressed, the bone marrow and subcutaneous fat signal are not removed by subtraction since T_2* of the lipid protons is on the order of the inter-echo time. Dual-band UTE yields considerably better short-T_2

contrast, but the soft-tissue suppression is not uniform across the FOV due to B_1 inhomogeneity, (Fig. 2.6c). When combining dual-band UTE with echo subtraction, better overall soft-tissue suppression is achieved (Fig. 2.6d). IR-UTE yields the highest contrast between short- and long-T_2 regions with homogeneous soft-tissue suppression (Fig. 2.6e). On the other hand, cortical bone SNR in IR-UTE is lowest.

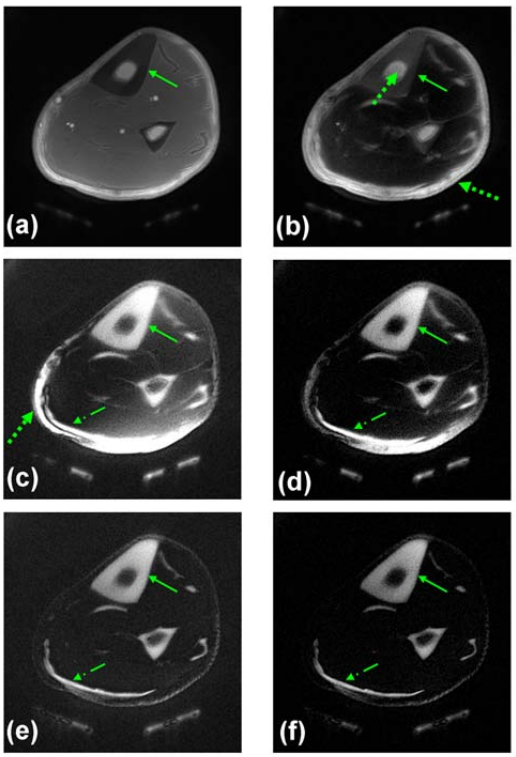

Figure 2.6 Axial mid-tibia images of a healthy volunteer: a, b) dual-echo UTE; c, d) dual-band UTE; e, f) IR-UTE. Left column (a, c, e): first-echo images; right column (b, d, f): difference images (first minus second-echo). Cortical bone (thin arrow) is obscured by the surrounding intense soft-tissue signal, but highlighted in the long-T_2 suppressed images. The tendon signal also appears enhanced (dotted-dashed arrow). There is significant residual fat signal in dual-echo UTE (dashed arrow in (b)). Dual-band UTE has high short-T_2 SNR but its soft-tissue suppression is inhomogeneous (dashed arrow in (c)). Cortical bone contrast is highlighted and uniform in IR-UTE (e, f). For better comparison, (c, d, e, f) are on the same window/level. Signal extraneous to the boundaries of the calf is from polymeric structures of the coil.

Fig. 2.7 shows images of the left Achilles tendon of a 38-year-old healthy male volunteer. Since the water density in tendon is substantially higher than that in bone, its

signal intensity is comparable to the surrounding muscle tissue even without long-T_2 suppression. Otherwise, the relative benefits and trade-offs of the various suppression techniques are replicated for this short-T_2 tissue.

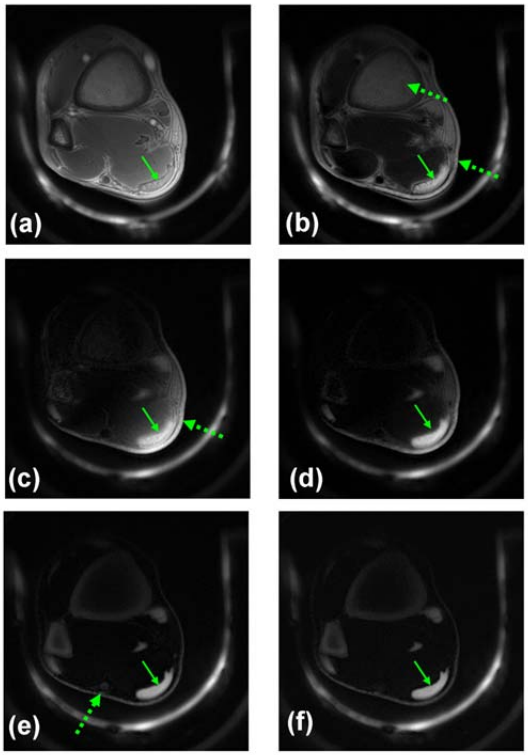

Figure 2.7 Axial lower-extremity images of a healthy volunteer: a, b) dual-echo UTE, c, d) dual-band UTE: e, f) IR-UTE. Left column (a, c, e): first-echo images; right column (b, d, f): difference images (first minus second-echo). Contrast between Achilles tendon (thin arrow) and muscle is poor without soft-tissue suppression. Considerable residual fat signal appears in dual-echo UTE (dashed arrow in b)). Soft-tissue suppression is inhomogeneous (dashed arrow in c)) but it is improved when combined with dual-echo UTE (d). IR-UTE creates the highest and most homogeneous tendon contrast. Residual blood signal is visible (dotted arrow in (e)) due to its long T_1. The image window levels for echo row images are individually adjusted for better visualization since the image SNRs are substantially different from each other (see Table 2.2). Signal extraneous to the anatomy is from proton-containing structures of the ankle coil.

Table 2.2 quantitatively compares the performance of the three sequences in terms of the evaluation criteria used. Overall, dual-echo UTE yields the highest SNR_{eff} but the lowest contrast between short- and long-T_2 components. Relative to IR preparation dual-band saturation pulse preserves a greater fraction of short-T_2 signal. IR-UTE generates

the highest contrast between short and long-T_2 tissues, albeit at the expense of short-T_2 SNR, which is lowest at this suppression scheme. This behavior is exacerbated when the short-T_2 protons have relatively long T_1, as in the case of tendons. Some discrepancies were observed between the simulations (Fig. 2.5) and experimental results (Table 2.2), particularly for the tendon images. Possible reasons are the presence of multiple T_2 components for tendon water protons, and deviations from the desired flip angle due to the tendon's off-center location.

.

	Cortical Bone					
	SNR_{bone}	CNR_{bone}^{muscle}	CNR_{bone}^{marrow}	SNR_{bone}^{eff}	$\frac{SNR_{bone}}{SNR_{muscle}}$	$\frac{SNR_{bone}}{SNR_{marrow}}$
dual-echo UTE	25.6±2.7	15.6±1.1	-42.4±2.4	1.00	2.56	0.38
dual-band UTE	32.1±7.3	20.7±6.6	16.3±7.0	0.72	2.84	2.03
IR-UTE	26.1±5.0	20.2±4.5	17.1±3.0	0.53	4.42	2.90

	Tendon			
	SNR_{tendon}	CNR_{tendon}^{muscle}	SNR_{tendon}^{eff}	$\frac{SNR_{tendon}}{SNR_{muscle}}$
dual-echo UTE	140.5±17.4	126.5±9.1	1.00	10.0
dual-band UTE	172.2±34.6	160.0±29.0	0.49	14.1
IR-UTE	86.5±7.2	81.4±7.2	0.32	17.0

Table 2.2 Quantitative comparison of three long-T_2 suppression sequences, including absolute SNR of cortical bone (SNR_{bone}) and Achilles tendon (SNR_{tendon}), CNR Between cortical bone and muscle (CNR_{bone}^{muscle}), cortical bone and marrow (CNR_{bone}^{marrow}), Achilles tendon and muscle (CNR_{tendon}^{muscle}), relative SNR efficiencies of cortical bone (SNR_{bone}^{eff}) and Achilles tendon (SNR_{tendon}^{eff}), SNR ratios of cortical bone to muscle ($\frac{SNR_{bone}}{SNR_{muscle}}$), cortical bone to marrow ($\frac{SNR_{bone}}{SNR_{marrow}}$), and Achilles tendon to muscle ($\frac{SNR_{tendon}}{SNR_{muscle}}$), expressed as means ± standard deviation from five subjects

2.6 Discussion and Conclusions

Soft-tissue suppression techniques employed in UTE imaging generate high short-T_2 contrast so as to reveal short-T_2 components ordinarily obscured by long-T_2 components. This work attempted to compare the performance of three long-T_2 suppression UTE sequences in an unbiased manner via simulation and experiment. Results show that excellent short-T_2 contrast can be achieved when generated with these optimized sequences.

Dual-echo UTE is the most commonly used soft-tissue suppression method. It is insensitive to both B_1 and B_0 inhomogeneities and is most SNR efficient as predicted theoretically and experimentally. This result is intuitive since no magnetization preparation is needed, which will always involve losses. Somewhat unexpected was the finding that background noise appears to be attenuated in multi-coil combined magnitude image subtraction, even though noise is amplified by $\sqrt{2}$ in a single-channel complex difference image. In fact, the noise level is amplified as expected by a factor of $\sqrt{2}$. However, since the mean of the background signal is substantially reduced after subtraction (all values before subtraction are strictly positive), the noise appears to be attenuated in the magnitude display (refer to Figs. 3.6(b), (d) and (f)). Additionally the subtraction operation may attenuate subtle streaking artifacts. The major problem with dual-echo UTE is the significant residual signal from species with T_2* comparable to the echo spacing, such as bone marrow and subcutaneous fat. Lipid protons tend to have T_2* values as short as 10 ms resulting from destructive interference of their various chemically shifted components, and field inhomogeneity induced by susceptibility

variations of the air-tissue and bone-soft tissue interfaces. The data suggest that incorporation of dual-echo subtraction into magnetization preparation methods may be beneficial as a means to capitalize on the latter's complementary long-T_2 suppression properties.

With the optimized dual-band pulse, dual-band UTE achieves short-T_2 contrast superior to dual-echo UTE and higher SNR than IR-UTE. Since the UTE acquisition is played out immediately after the dual-band pulse, shorter scan time is possible than with IR-UTE which demands inclusion of an inversion delay. As well, the pulse design algorithm offers significant freedom to control the dual-band pulse, including flip angles, bandwidths and ripple values. In particular, frequency-band flip angles allow suppression of either long-T_2 component, which is not possible with a single-band saturation pulse. However, as all frequency-selective saturation pulses are, the dual-band pulse is sensitive to spatial variations in B_1 and B_0 fields, resulting in inhomogeneous soft-tissue suppression. A possible alternative is the use of 90^o adiabatic pulses to address the B_1 sensitivity problem (82), but its saturation effect on short-T_2 species first needs to be investigated. To minimize sensitivity to B_0 inhomogeneity, larger bandwidths are required, particularly at high magnetic field, which in turn augment undesired saturation of the short-T_2 protons (65). To alleviate the pulse's sensitivity to B_1 and B_0 inhomogeneities and maximize soft-tissue suppression as demonstrated by the results, it is recommended to combine the dual-band UTE and echo subtraction method.

IR-UTE produces the highest short-T_2 contrast, achieved at the expense of SNR, which is lowest among the three long-T_2 suppression techniques. Soft-tissue suppression is uniform across the entire FOV due to the relative immunity of the adiabatic inversion

pulse to B_1 inhomogeneity. In the present work the pulse was designed to achieve optimal soft-tissue suppression. Further, judicious choice of TR minimizes the TI difference between components differing in T_1. However, because of the time delay for long-T_2 inversion nulling, the scan time is relatively extensive compared to other sequences. Phase-sensitive IR (66) obviates the need for an inversion delay allowing for UTE acquisition immediately after the adiabatic inversion pulse. However, as shown in the simulations, saturation of the short-T_2 protons is significant, particularly in combination with long T_1 and increased pulse-bandwidth of the preparation pulse. Furthermore, two acquisitions with and without inversion preparation are required, which would double total scan time. Therefore, this method is not well suited in high-field applications since greater absolute field inhomogeneity and broader lipid spectrum necessitate larger pulse bandwidth. Also, because of the substantial saturation caused by the adiabatic pulse, the short-T_2 signal in IR-UTE mainly arises from longitudinal magnetization built up during the inversion time. This intuitively explains why half pulses with flip angles near 90 degrees are used in IR-UTE to maximize the short-T_2 signal, which indicates that IR-UTE may not be favorable to image short-T_2, long-T_1 species. Instead of a single adiabatic inversion pulse, two back-to-back pulses were used by Du et al. in DIR-UTE to suppress long-T_2 components with different T_1s (67). However, since the difference in inversion null times for water and fat is usually less than the duration of the long adiabatic pulse, TI for fat is suboptimal. Prolonging TR can partially rectify this problem, but at the expense of impractically long scan times. Another possible solution is to use dual-band adiabatic inversion pulse (83) to invert the long-T_2 components sequentially rather than simultaneously according to their TI difference. In (23), Du et al. conducted a comparison

between the soft-tissue suppression schemes investigated in this work with 3D UTE imaging. Although the imaging parameters for each individual long-T_2 suppression method were not optimized and the comparison experiments were not carried out on the same anatomy due to long scan time of 3D UTE in (23), the authors also concluded that IR-based UTE (IR-TUE or DIR-UTE) is a simple and efficient method that can relatively easily be implemented on clinical scanners. The evaluation in this work showed that IR-UTE is a low-SNR but high-CNR sequence with uniform soft-tissue suppression, which is preferred for imaging short-T_2 species with relatively short T_1, such as cortical bone. The results of the performance evaluation and comparison among the various sequences are summarized in Table 2.3.

Performance criterion	dual-echo UTE	dual-band UTE	IR-UTE
Short-T_2 SNR	+	=	−
Long-T_2 suppression	−	=	+
Robustness to B_0 inhomogeneity	+	=	=
Robustness to B_1 inhomogeneity	+	−	+
Scan time	+	=	−

Table 2.3 Relative performance of three soft-tissue suppression sequences: -/=/+ scale indicating poorest to best.

The short-T_2 SNR efficiency could be improved by acquiring multiple slices in an interleaved fashion. For the dual-echo UTE this mode of operation would increase SNR efficiency by a factor equal to the square-root of the number of slices acquired within a given TR period (just as in conventional multi-slice MRI). For dual-band UTE and IR-UTE, multiple slices can also be acquired within a TR period after each magnetization preparation pulse. However, this may result in somewhat impaired soft-tissue suppression

across slices. Thus, there is a trade-off between SNR efficiency and extent of long-T_2 suppression when translating these soft-tissue suppression schemes into multislice mode.

The key motivation for soft-tissue suppression in UTE imaging is to enhance the visualization of short-T_2 tissues obscured by the overwhelming long-T_2 signal. More recently, soft-tissue-suppressed UTE imaging has been applied to directly quantify short-T_2 species, such as cortical bone water concentration (77), carotid plaque calcium (84,85) and myelin content (86). The motivation for incorporating long-T_2 suppression into UTE imaging is to avoid soft-tissue contamination because UTE imaging without suppression suffers from contamination of the signal from long-T_2 components or slice profile imperfections in 2D UTE. To decide on specific suppression schemes for short-T_2 imaging, the user will have to evaluate their performance and optimize the imaging parameters with SNR and CNR as the objective function. Also, as new soft-tissue suppression methods arise, it would seem appropriate to examine their performance against the methods evaluated in the present work to allow for unbiased comparison.

A limitation of this study is its focus on a comparison of short-T_2 SNR and CNR between short- and long-T_2 tissues for the three most widely used soft-tissue suppression methods in their 2D embodiments. Other methods, such as TELEX (62,63) and DIR-UTE (67), were not evaluated and compared although they are variants of the methods investigated in this work. The sensitivity of these methods to pathologic changes of short-T_2 tissues remains to be examined to assess their clinical capabilities. Lastly, 3D implementations of the above sequences and their potential to visualize the microanatomy of collagen-rich short-T_2 tissues need to be investigated in future work.

This work has attempted to achieve an unbiased quantitative performance assessment of the three most commonly used soft-tissue suppression methods by optimizing imaging protocols by both simulation and measurements in phantoms and *in vivo*. IR-UTE provides the highest short-T_2 contrast and is well suited for imaging short-T_2 species with relatively short T_1. A combination of dual-band UTE with dual-echo UTE yields both good SNR and CNR and reduced sensitivity to B_1 inhomogeneity. The results provide a guide for the use of soft-tissue-suppressed UTE in research and in the clinic and the approach described may be useful for evaluating the performance of future soft-tissue suppression methods.

Chapter 3 ZTE Imaging with Excitation Profile Correction

3.1 Abstract

ZTE imaging is a promising technique for MRI of short-T_2 tissue nuclei in tissues. A problem inherent to the method currently hindering its translation to the clinic is the presence of a spatial encoding gradient during excitation, which causes the hard pulse to become spatially selective, resulting in blurring and shadow artifacts in the image. While shortening RF pulse duration alleviates this problem, the resulting elevated RF peak power and specific absorption rate (SAR) in practice impede such a solution. In this work, an approach is described to correct the artifacts by applying quadratic phase-modulated RF excitation and iteratively solving an inverse problem formulated from the signal model of ZTE imaging. A simple pulse sequence is also developed to measure the excitation profile of the RF pulse. Results from simulations, phantom and *in vivo* studies, demonstrate the effectiveness of the method in correcting image artifacts caused by inhomogeneous excitation. The proposed method may contribute toward establishing ZTE MRI as a routine 3D pulse sequence for imaging protons and other nuclei with quasi solid-state behavior on clinical scanners.

3.2 Introduction

As discussed in Chapter 1, the unique feature of ZTE imaging is the presence of the spatial encoding gradient during non-selective excitation. The sequence variants currently in practice include SPRITE (single-point ramped imaging with T_1 enhancement) (29), WASPI (water- and fat-suppressed proton projection MRI) (8) and PETRA (pointwise encoding time reduction with radial acquisition) (9). Compared to UTE, ZTE traverses *k*-

space faster, resulting in higher SNR and reduced blurring due to less T_2 decay within the data acquisition window (87). Since data sampling occurs during the plateau period of the readout gradient in ZTE, the image distortion artifact associated with ramp sampling in UTE imaging is avoided.

However, problems can arise in ZTE due to the imaging gradient being on during hard pulse excitation. First, the central portion of *k*-space is missed resulting from the time delay between the end of RF transmission and the start of data acquisition. Several approaches have been proposed to solve this problem, including algebraic reconstruction (10,21), acquisition of additional radial projections with lower gradient strength as in WASPI (8), and single point imaging as in PETRA (9) following the radial encoding portion of the sequence.

Another well-known problem resulting from the presence of the imaging gradient is that the hard pulse becomes spatially selective. In the low flip-angle regime, the excitation profile of the hard pulse as a function of frequency is sinc-shaped as given by the Fourier transform of a rectangular waveform. The problem is negligible on laboratory imaging systems allowing for high peak power and thus very short pulse duration. However, B_1 peak power and SAR limitations impose practical limits for *in vivo* scanning of humans (22). As elaborated upon in the following section, both blurring and shadow artifacts near the object's boundary can arise in the reconstructed image without correction of the spatially dependent excitation profile.

Recently, Grodzki et al. investigated the effects of the sinc-shaped excitation profile in PETRA and proposed an approach to correct for the resulting image artifacts (23). However, their correction algorithm requires that the imaged object fit into the sphere

defined by the main lobe of the sinc-shaped excitation profile. If these conditions are not met the amplified noise resulting from inversion of the ill-conditioned matrix rooted from the zero crossings of the sinc function would corrupt the resulting image. Thus, the problem of spatially dependent excitation in ZTE imaging of humans in clinical scanners has yet to be solved.

In this work, the ZTE sequence signal is modeled to include the excitation profile effect, and formulate a correction algorithm as a solution to an inverse problem. In order to eliminate the zero crossings in the sinc excitation profile and to condition the inverse problem, the hard RF pulse is modulated with quadratic phase, which produces a flatter excitation profile. A simple pulse sequence is also developed to measure the excitation profile of the RF pulse. Without loss of generality, the proposed method was applied to one variant of ZTE imaging sequences, namely PETRA. By combining phase-modulated RF excitation and iteratively solving the inverse problem, results from simulations, phantom and *in vivo* studies demonstrate the effectiveness of the proposed method for correcting image artifacts caused by inhomogeneous excitation, even when the extent of the imaged object exceeds the main lobe of the sinc function.

3.3 Signal Model of ZTE Imaging

In standard MRI, the signal model is given by:

$$s(k) = \iiint_V m(r) e^{-i2\pi <k,r>} dr + \varepsilon \qquad [1]$$

where $s(\boldsymbol{k})$ is the complex signal at the spatial frequency-space (k-space) location $\boldsymbol{k}$, $m(\boldsymbol{r})$ denotes the spatial distribution of the imaged object's transverse magnetization at

spatial coordinate $\boldsymbol{r}$, $\langle \bullet, \bullet \rangle$ denotes the vector inner product, and ε is additive complex Gaussian noise. The *k*-space location $\boldsymbol{k}$ at a particular point in time depends on the sampling pattern of the pulse sequence. For example, for PETRA, as shown in Fig. 3.1, the *k*-space sampling is divided into two parts: the outside portion is acquired with radial trajectories, while the center is filled on a Cartesian grid by single point imaging (9).

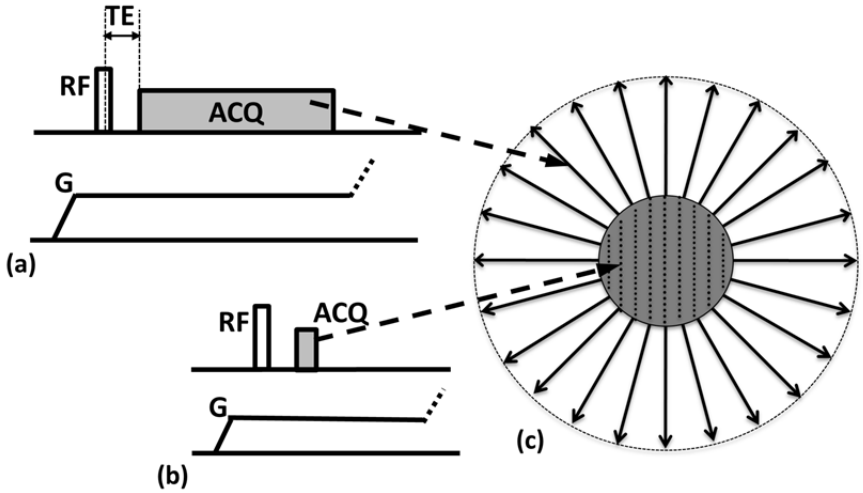

Figure 3.1 Pulse sequence diagram of PETRA, consisting of, a) radial acquisition, b) Cartesian portion. The latter uses single point encoding to fill the missing *k*-space points; c) corresponding *k*-space trajectory.

As pointed out above, the presence of the spatial encoding gradient during RF pulse excitation makes the non-selective pulse in ZTE frequency selective. As a result, an excitation profile is superimposed onto $m(r)$:

$$s(k) = \iiint_V m(r)\, p(f) e^{-i2\pi \langle k, r \rangle} dr + \varepsilon \qquad [2]$$

For a given RF pulse waveform, $p(f)$ is the excitation profile expressed as a function of resonance frequency f which is given by $f = \gamma \langle G, r \rangle$, with γ being the gyromagnetic ratio and G the imaging gradient. The goal is to reconstruct $m(\boldsymbol{r})$. In conventional image

reconstruction a uniform excitation profile $p(f)$ is assumed. A gridding algorithm is usually employed to accomplish image reconstruction (16).

However, in practice $p(f)$ is not homogeneous due to the finite pulse duration imposed by the peak RF power and SAR constraints (particularly restrictive with clinical imaging hardware). The profile must therefore be included in the image reconstruction in order to avoid artifacts that would degrade image quality. A rectangular hard pulse is typically used for excitation in ZTE:

$$B_1(t) = \begin{cases} b_1, & \text{if } |t| \le \dfrac{\tau}{2} \\ 0, & \text{elsewhere} \end{cases} \qquad [3]$$

where τ is the pulse duration, and the reference time of the hard pulse is at the center of the pulse, i.e. the *k*-space center. The pulse amplitude b_1 is determined by the desired flip angle θ and the pulse duration τ according to $\theta = 2\pi\gamma b_1 \tau$.

Based on the small-tip-angle approximation theory, which is valid for flip angles less than 30 degrees (88,89), the excitation profile $p(f)$ is calculated as the Fourier transform of rectangular hard RF pulse waveform:

$$p(f) = \frac{\sin(\pi f \tau)}{\pi f \tau} = \mathrm{sinc}(\pi f \tau) \qquad [4]$$

Substituting $f = \gamma < G, r >$ into Eq.4:

$$p(G, r) = \mathrm{sinc}(\pi\gamma < G, r > \tau) \qquad [5]$$

Eq.[5] shows that the excitation profile is a function of both the imaging gradient and the

spatial location thereby resulting in image artifacts. During acquisition of the outer (i.e. radial) portion in PETRA, the imaging gradient amplitude $|G|$ is kept constant for each projection. As r increases from the center to the edge of the field-of-view (FOV), $p(G, r)$ decreases and signal variation is introduced across the FOV causing a shadow artifact at the object's boundary. One can see that the artifacts are less severe in the center FOV region because of smaller r, and in fact the FOV center should be relatively free of artifacts. On the other hand, in the central Cartesian portion of k-space, a lower gradient amplitude $|G|$ is used, resulting in higher $p(G, r)$ values. From a signal processing perspective, $p(G, r)$ acts like low spatial frequency filter and the reconstructed image without correction suffers from blurring.

The severity of the image artifacts depends on the relative length of the pulse duration τ compared to the readout sampling time gap d (termed dwell time). To see this, the maximum distance from the FOV center, r_{max}, is given by:

$$r_{\max} = \frac{1}{2\gamma |G| d} \qquad [6]$$

Inserting Eq.6 into Eq.5, obtain the profile at the FOV boundary:

$$p(G, r_{\max}) = \operatorname{sinc}\left(\frac{\pi\tau}{2d}\right) \qquad [7]$$

As is evident from Eq.7, the excitation profile is relatively uniform and no image as long as the pulse duration τ is much shorter than the dwell time d, in which case no artifacts are apparent. However, for longer pulse durations, the profile becomes increasingly heterogeneous and image artifacts become noticeable. In practical imaging

experiments, a typical value of d is 5 μs, therefore the pulse duration should be less than 5 μs in order to make the image artifacts negligible. In practice, this condition is difficult to achieve as the B_1 peak power to allow a desired flip angle may exceed SAR limits when scanning humans.

3.4 Proposed Algorithm for Excitation Profile Correction

3.4.1 Model as an Inverse Problem

In order to eliminate image artifacts, the effect of the non-uniform excitation profile needs to be considered in image reconstruction. The discretization of Eq.2 yields

$$s(k_j) = \sum_{i=1}^{N} m(r_i) p(G_j, r_i) e^{-i2\pi < k_j, r_i >} + \varepsilon_j \quad j = 1, 2, ..., M \qquad [8]$$

where N is the number of pixels of the reconstructed image, and M is the number of k-space samples. In matrix form, Eq.8 becomes:

$$s = Am + \varepsilon \qquad [9]$$

where A is the system matrix with its elements $A_{i,j} = p(G_j, r_i) e^{-i2\pi < k_j, r_i >}$.

Image reconstruction can now be formulated as an optimization problem with an optional regularization term. As pointed out in (90), a small total variation (TV) regularization term is helpful to alleviate the streaking artifact in radial imaging. The final form of the reconstruction problem can be written as:

$$\hat{m} = \arg\min_m \left\| Am - s \right\|_2^2 + \lambda \left\| Dm \right\|_1 \qquad [10]$$

where D is the finite difference operator. $\|\cdot\|_1$ denotes the vector's L_1-norm and λ is the regularization parameter. Several algorithms can be used to solve Eq.10, among which the Split-Bregman method (or Augmented Lagrangian method) (91) has been proven to be efficient. During the iteration, a Conjugate Gradient algorithm is employed as a subroutine to solve a quadratic optimization problem, in which the matrix-vector multiplication is the most computationally intensive (~$O(N^2)$). For example, assuming the reconstructed image matrix size (or N) is 128^3, each matrix-vector multiplication takes $O(128^6)$~$O(10^{12})$ computations. Therefore, the enormous size of the system matrix A prevents explicit matrix-vector multiplication during the iterations.

Instead, the matrix-vector multiplication is implicitly computed as a series of operators on a vector. Here s is defined as the coordinate along the imaging gradient direction. According to the central slice theorem, the k-space signal along the gradient direction in Eq.2 is rewritten as:

$$s(k_G) = \int_{-\infty}^{\infty} \{\mathscr{R}(m(r)p(G,r))\}(G,s)e^{-i2\pi ks}ds \qquad [11]$$

where R denotes the Radon transform. The noise term is dropped for simplicity. Noting that $s = \langle G, r\rangle$, p is a function of s and thus can be moved out of the Radon transform:

$$s(k_G) = \int_{-\infty}^{\infty} \{\mathscr{R}(m(r))\}(G,s)p(s)e^{-i2\pi ks}ds \qquad [12]$$

Therefore, the k-space signal of each projection in ZTE imaging can be interpreted as the 1D Fourier transform of the Radon transform of the magnetization modulated by

the excitation profile. The Radon transform can be approximated by the non-uniform fast Fourier transform (NUFFT) (17,92) with sufficient accuracy and fast computation, which reduces to ~$O(N\log N)$ per the matrix-vector multiplication. From Eq.12, the system matrix is decomposed into three operators:

$$A = RPF \qquad [13]$$

where F is the NUFFT operator that maps the (Cartesian) image to k-space (full) radial spokes, with one spoke for each radial trajectory, and additionally one spoke for each Cartesian point. The P operator acts on each projection separately by zero-padding (by a factor of 2), 1D IFFT, multiplication with the excitation profile, 1D FFT, and finally restoration of the original vector length. The sampling operator, denoted R, masks out the fraction of the radial signal that was not acquired (recall that less than half of each radial spoke is acquired) and performs Dirichlet interpolation in the Cartesian portion (since the coordinates of the single points may not coincide with those in the radial spokes) (93). Application of the operator F is the most time-consuming process, requiring ~$O(N\log N)$ computations. The adjoint operator A^H is the reverse process of the above steps. A flow chart describing the algorithm is shown in Fig. 3.2. The image reconstruction algorithm was implemented in Matlab (Mathworks, Natick, MA, USA) with NUFFT algorithm as a mex function written in C.

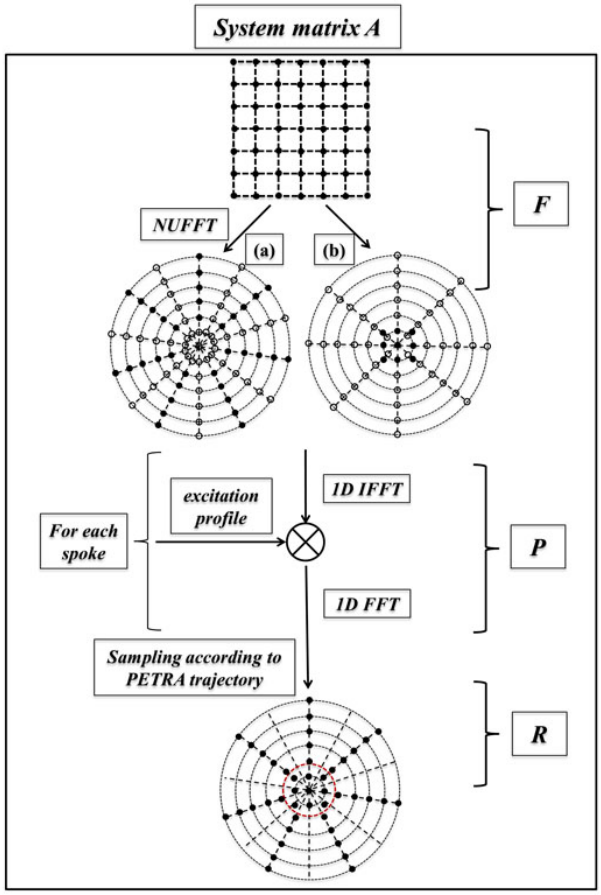

Figure 3.2 Diagram of the implementation of the system matrix *A*, composed of three sequential operators: the NUFFT operator *F*, the excitation profile modulation operator *P* and the sampling operator *R*. The solid dots in a) and b) represent the acquired samples in *k*-space and the hollow circles denote the locations which are interpolated by NUFFT but not acquired by the sequence.

3.4.2 Quadratic Phase-Modulated Hard RF Pulse

As shown in Eq.7, when the RF pulse duration is twice the dwell time, the profile's zero crossings are within the FOV, causing the system matrix *A* to be singular and the inverse problem to be ill conditioned. In order to eliminate the zero crossings of the rectangular pulse excitation profile, a quadratic phase is modulated to the RF pulse waveform:

$$B_1(t) = \begin{cases} b_1 e^{i2\pi\beta\left(\frac{t}{\tau}\right)^2}, & \text{if } |t| \le \frac{\tau}{2} \\ 0, & \text{elsewhere} \end{cases} \qquad [14]$$

where β controls the amount of quadratic phase applied to the RF pulse. In all of the following applications, β is set to 1. The corresponding excitation profile can be computed by numerical Bloch equation simulation. The quadratic phase-modulated pulse has a flatter excitation profile than does a simple hard pulse. More importantly, no zero-crossing point occurs in the profile even when the pulse duration is four times that of the dwell time (see Fig. 3.4).

3.4.3 Excitation Profile Measurement

In order to confirm that the theoretical excitation profile is indeed achieved, a simple pulse sequence is used for its measurement, which can be inserted as a pre-scan into the ZTE sequence. A sketch of this pulse sequence is shown in Fig. 4.3(a, b). Suppose the signals acquired by the first and second acquisitions are S_1 and S_2, respectively. The excitation profile $p(f)$ is calculated as:

$$p = \frac{FT^{-1}(S_1)}{FT^{-1}(S_2)} \qquad [15]$$

A flow diagram illustrating the data acquisition and processing procedures is shown in Fig. 3.3.

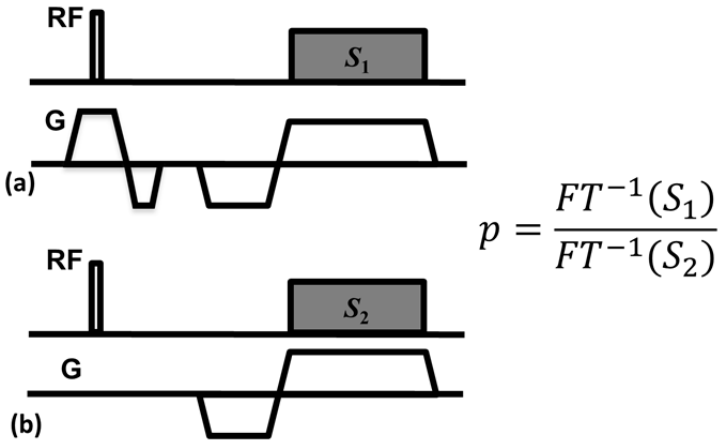

Figure 3.3 Pulse sequence diagram for RF pulse excitation profile measurement. The signals from acquisitions a) and b) are first transformed into image space by inverse Fourier transform, generating projections with and without modulation excitation profile. The profile is then obtained by taking ratio between the projections.

3.4.4 Simulations

A 2D Shepp-Logan phantom was used to generate the simulated data by applying the operators described in Eq.13. The excitation profile effects of both the rectangular and quadratic phase-modulated RF pulse were simulated. The pulse duration τ was varied from one to four times the dwell time d of 5 μs. Other parameters of the sequence used in the simulation were: T/R switch dead time = 70 μs, 300 half radial projections, and reconstructed image matrix size = 128×128. Complex Gaussian noise was then added to the simulated k-space data, yielding SNR ~50. The images were reconstructed with and without the correction algorithm from the simulated noisy *k*-space data.

3.4.5 Experiments

A doped-water phantom was imaged at 3T (SIEMENS Tim Trio, Erlangen, Germany) using the PETRA sequence with a four-channel receive-only head coil and body coil RF transmission and the following scan parameters: 1.30 mm isotropic voxel

size, matrix size = 192^3, number of half-projections = 30,000, flip angle = 6º, TE = 100 μs, TR =10 ms. To investigate the effect of inhomogeneous excitation profile a series of scans were performed with dwell times of 5, 10 and 20 μs while fixing the pulse duration at 20 μs. The excitation profiles of both rectangular (Eq.3) and phase-modulated (Eq.14) RF pulses were measured by the proposed pulse sequence and compared with those obtained by Bloch equation simulations. A product spoiled gradient-echo (GRE) sequence with TE of 2.5 ms was also run with the same image resolution for comparison.

The head of a 40 year-old healthy male volunteer was scanned with the PETRA sequence with the same coil as previously used in the phantom experiments. The protocol for this study was approved by the Institutional Review Board and written informed consent was obtained from the subject. Scan parameters were: 1.17 mm isotropic voxel size, matrix size = 256^3, number of half-projections = 50,000, flip angle = 5º, TE = 85 μs, TR = 10 ms, readout bandwidth = ±62.5 kHz (corresponding to 5 μs dwell time). Both rectangular and phase-modulated excitation pulses were used as excitation pulses with 20 μs duration. Images from a GRE sequence with TE of 2.5 ms obtained at the same image resolution were used for comparison.

To ensure that all reconstructions were performed under identical conditions, the same regularization parameter $\lambda = 0.0001$ was used after automatically scaling the raw data for consistency. While it is possible that the image quality could be improved slightly with a different choice of the total variation weight, this type of optimization is beyond the scope of the present analysis. Since *k*-space was not significantly undersampled, modest L1 regularization is not expected to appreciably impact image

quality. For the sake of simplicity, the multiple-coil data are treated separately. All images were first reconstructed channel-by-channel and then combined as square root of the sum of squares.

3.5 Results

3.5.1 Excitation Profile Measurement

The rectangular and quadratic phase-modulated pulse waveforms with 20 μs duration are shown in Fig. 3.4a. Figs. 3.4b and c compare the magnitude and phase of the excitation profiles of both RF pulses as a function of frequency, obtained by numerical Bloch equation simulations, with measurements by the proposed pulse sequence, respectively. The simulation results are in good agreement with those obtained experimentally. As seen from Fig. 3.4b, the phase-modulated pulse eliminates the zero crossings in the sinc-shaped profile of the hard pulse excitation, which improves the condition number of the system matrix of the inverse problem.

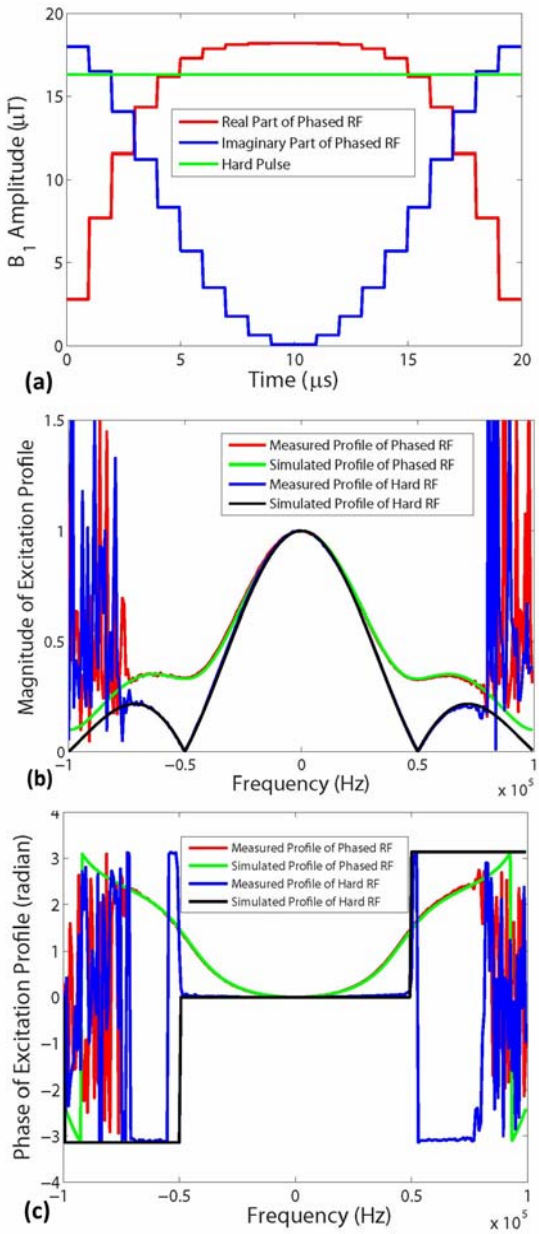

Figure 3.4 a) Waveforms of hard and quadratic phase-modulated RF pulses with 20 μs duration and flip angle of 5°; b) Magnitude and c) the phase of the excitation profiles of both pulses obtained by Bloch equation simulations and measurements with the pulse sequence in Fig. 4.3 with dwell time of 5 μs. The experimental data are in good agreement with simulations. The noisy oscillations in b) and c) occur in the region outside the imaged object.

3.5.2 Simulations

The simulated uncorrected images with varying pulse durations and constant dwell

time are shown in Figs. 3.5a-c. Figs. 3.5d-f and j-l show the corresponding corrected images with hard and phase-modulated pulse excitation, respectively, along with the difference images from the true image in Figs. 3.5g-i and m-o. No visible artifacts are present in the uncorrected image (Fig. 3.5a) with the same pulse duration and dwell time since the excitation bandwidth covers the spin resonance frequencies created by the spatial encoding gradient and the excitation profile inside the phantom is relatively uniform. However, as the pulse duration increases, the excitation bandwidth becomes narrower, resulting in a less homogeneous excitation profile and a more severe image artifact, as predicted by the theoretical analysis. The corrected images with hard pulse excitation eliminate the artifacts within the main lobe of the sinc-shaped profile, indicated by the dashed circle. However, residual artifacts are visible in the region outside the circle (Fig. 3.5f) since the spins in this area resonate at frequencies where the excitation profile is close to zero. The reconstructed images with phase-modulated pulse excitation in Figs. 3.5j-l effectively correct the artifacts even in the region outside the first zero crossing of the sinc function.

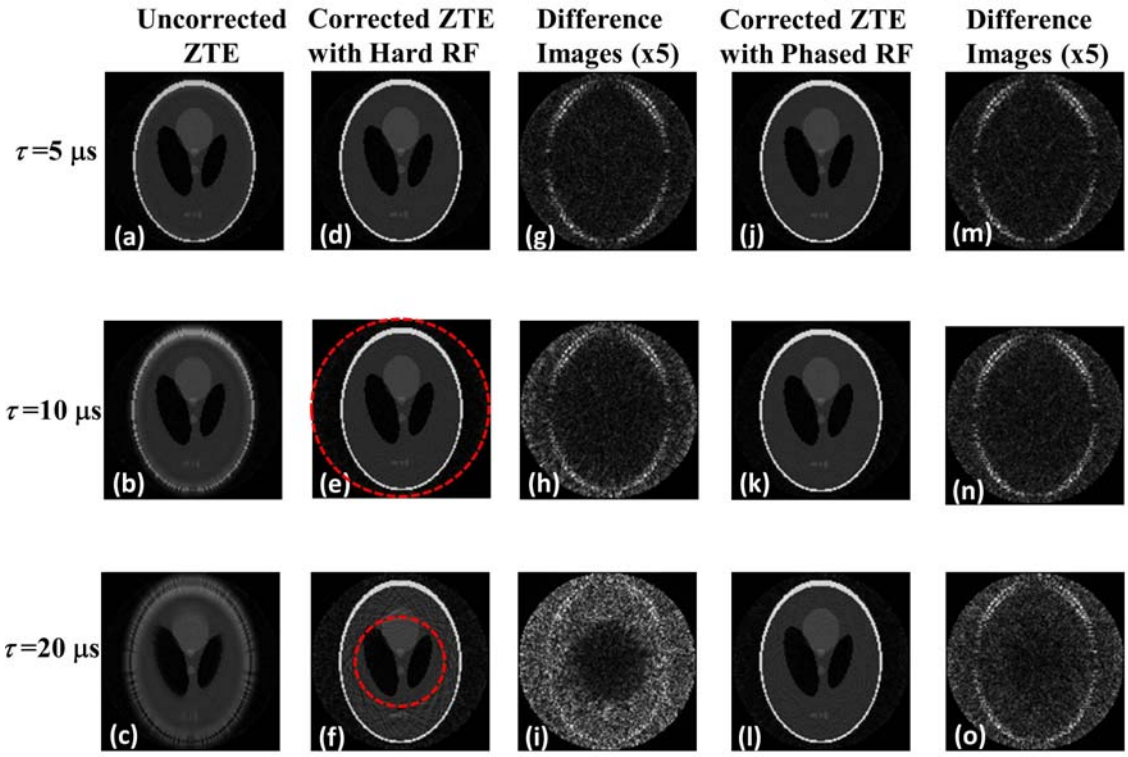

Figure 3.5 Simulated 2D phantom images with various pulse durations and constant dwell time of 5 μs. As the pulse duration increases image artifacts become more severe in the uncorrected image (a-c). The proposed algorithm and hard pulse excitation (d-f) removes the artifacts inside the sinc main lobe indicated by the dashed circle. However, residual artifacts are still visible outside the circle (f), which is also evident in the difference images (g-i). Combination of our algorithm and quadratic-phase modulated pulse effectively correct the artifact even when the pulse duration is four times of dwell time (j-o).

3.5.3 Experiments

Similar results as simulations are observed in phantom images with different dwell times in Figs. 3.6. As the dwell time gets shorter, the blurring and shadow artifacts become more apparent. The algorithm presented based on quadratic phase-modulated pulse excitation successfully removes the image artifacts in all cases and the images compare favorably with the reference gradient-echo image (Fig. 3.6j).

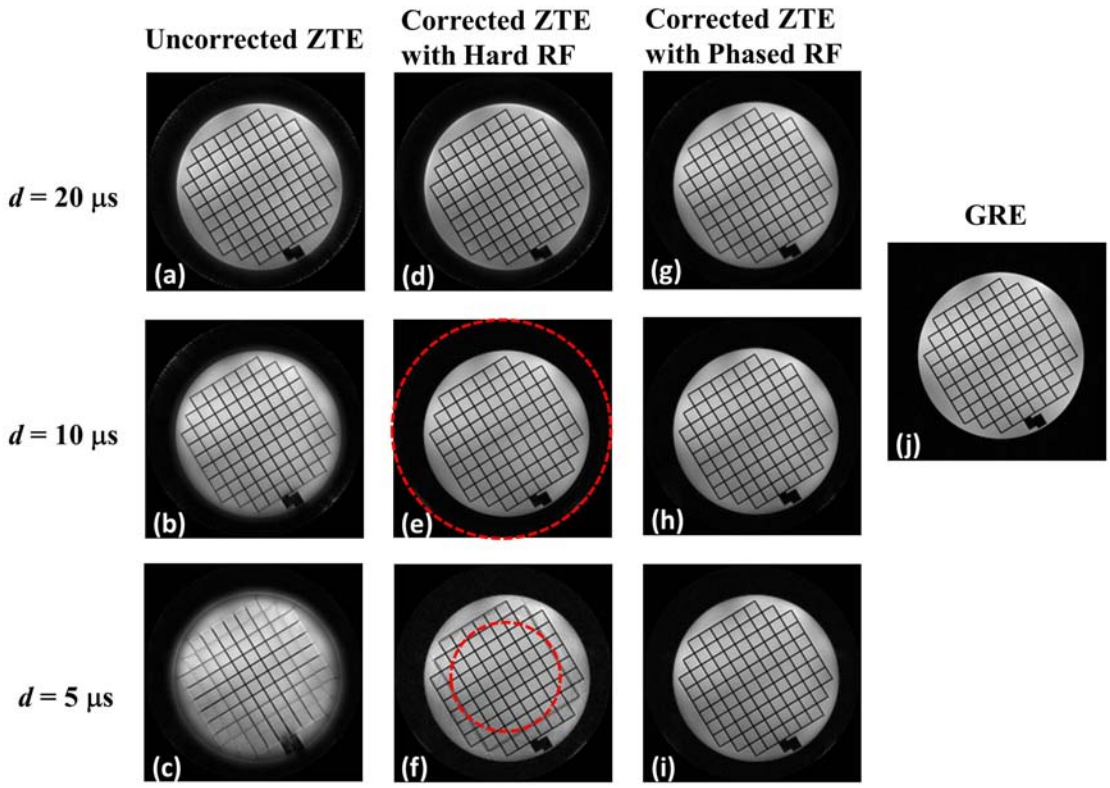

Figure 3.6 Axial ZTE phantom images obtained with constant pulse duration but varying dwell time. As the dwell time gets shorter, blurring and shadow artifacts become more apparent in (a-c). Although artifacts in images with hard pulse excitation are corrected inside the main lobe of the sinc-shaped excitation profile indicated by the dashed circle, the outside region still suffers from artifacts (d-f). The new algorithm, along with phase-modulated RF pulse excitation (g-i) removes the artifacts yielding image quality to that of a conventional GRE sequence (j).

Fig. 3.7 compares *in vivo* ZTE brain images on the sagittal and coronal planes with and without correction, along with images from a reference GRE sequence. The dashed circles in the second column images (Figs. 3.7c and d) indicate the locations of the zero crossing of sinc-shaped profile with hard pulse excitation. While no residual artifact appears in the regions inside these circles, the noise amplification due to the inversion of a singular system matrix creates artifacts in the corrected images with hard pulse excitation. In contrast, the artifacts are effectively corrected with quadratic-phase pulse excitation yielding image quality comparable to the GRE sequence. Lastly, one can see

that the ZTE images are free from the susceptibility artifact due to the air-tissue interface in GRE images as indicated by the arrows in Fig. 3.7g.

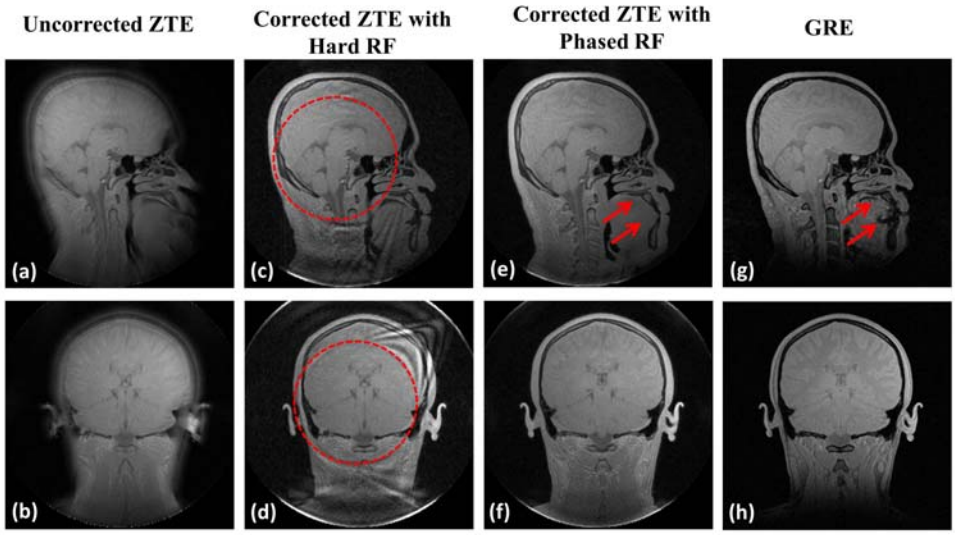

Figure 3.7 *In vivo* ZTE brain images with 20 μs pulse duration and 5 μs dwell time showing the sagittal and coronal planes. Results are in good agreement with those from simulations and phantom experiments. Note that the ZTE images corresponding to TE = 85 μs eliminate the susceptibility artifact due to the air-tissue interface noticeable in GRE images (TE = 2.5 ms) as indicated by arrows (g).

3.6 Discussion and Conclusions

In ZTE imaging, the presence of the spatial encoding gradient during non-selective RF excitation offers advantages over UTE imaging in terms of faster *k*-space traversal and elimination of artifact from ramp sampling. However, the imaging gradient also causes a non-uniform excitation profile across the FOV. Therefore, as pointed out in (23) and in section III, the measured ZTE signal turns out to be the Fourier transform of the Radon transform of the magnetization modulated by the excitation profile according to the central slice theorem. As a result, blurring and shadow artifacts appear in the uncorrected images. Although extremely short RF pulse durations compared to the dwell time can be used to alleviate such artifacts, high peak power is needed to achieve the

optimal Ernst angle and SAR could be an issue for human scans. Also higher power RF transmission requires a stronger RF amplifier and a dedicated transmit coil. In (23), the effect of the inhomogeneous excitation profile was simulated and an algorithm was proposed to correct the artifacts. This algorithm works under the condition that the object is inside the main lobe of the sinc-shaped excitation profile of the rectangular pulse. However, once this condition is violated, the elevated noise level corrupts the reconstructed image.

This chapter has presented an effective algorithm for correcting the artifacts in ZTE imaging within the limits of current clinical scanner hardware and SAR constraints without any modification of coil hardware, and more importantly, allowing the imaged object to extend beyond the main lobe of the hard pulse excitation profile. The proposed method is readily adapted to other ZTE sequences, e.g. SPRITE (29), WASPI (8).

There are several innovations in this proposed method. First, the signal model in ZTE imaging was derived to include the effect of non-uniform excitation profile, from which the origins of the artifacts can be analyzed. An inverse problem was formulated from the signal model. By taking advantage of the central slice theorem and computationally efficient NUFFT, an iterative algorithm was designed and implemented to solve the inverse problem with an optional regularization term. Since the noise effect is included in this new correction algorithm, the reconstructed image quality is superior to the corrected images shown in (23).

Second, a quadratic phase-modulated rectangular (chirped) pulse was designed for excitation instead. As shown in both simulations and experiments, the corrected image with hard RF pulse excitation shows residual artifact outside the spherical region defined

by the main lobe of the sinc-shaped profile. This is because the null points in the excitation profile cause the system matrix to be singular and make the inverse problem ill-conditioned. When a quadratic phase modulation is applied to the RF pulse, the excitation profile becomes flatter and lacks a null point, as shown in the Bloch equation simulation results. This improved excitation profile can be understood as a type of regularization to physically reduce the condition number of the inverse problem. The sinc-shaped hard pulse excitation profile is pure real. As a way to remove the null point, an imaginary part is added into the profile to make it complex. Hence the magnitude of the profile is no longer singular. The improvement in the reconstructed images is evident. The amount of phase modulation applied to the RF pulse constitutes a trade-off between the flip angle and the minimum value of the absolute magnetization profile within the field of view. Application of too much phase yields low flip angle for a given peak B_1 amplitude and pulse duration. On the other hand, inadequate quadratic phase causes the magnetization profile to approach a sinc profile, and the noise will be amplified due to a close-to-singular system matrix. Here, a relatively small amount of quadratic phase was chosen in order achieve minimal flip-angle loss while maintaining a relatively flat excitation profile.

Third, a pulse sequence was proposed to measure the excitation profile. In (23), the profile was obtained by measuring the actual pulse shape with an oscilloscope followed by taking the Fourier transform of the pulse shape. This proposed approach does not require additional hardware and can be inserted as an optional component into the ZTE pulse sequence. The spectral profile measured by the new sequence shows good agreement with that obtained from the Bloch equation simulation. Therefore, the profile

from the numerical simulation is sufficiently accurate as an input for the correction algorithm.

As pointed out in (22), a general drawback of ZTE imaging in humans is the need for high power RF transmission with large-bandwidth excitation and the associated increase in SAR. With the proposed approach, ZTE imaging operated at lower peak power, longer pulse duration, larger flip angle or higher readout bandwidth becomes practical on clinical imagers, thus providing new opportunities for short-T_2 imaging. While the majority of short-T_2 imaging reported so far in the literature (1,2,12) has been by UTE MRI, there is both theoretical and experimental evidence that ZTE achieves superior SNR (94,95). The need for prolonged RF pulses is particularly stringent when the method is combined with soft-tissue suppression preparation pulses. In order to optimize short-T_2 contrast, inversion recovery (IR)-based long-T_2 suppression is usually employed to highlight short-T_2 tissue components (72,96). However, the optimal excitation flip angle of IR-based sequences is close to 90 degrees, therefore, requiring relatively long RF pulses to achieve the desired flip angle that optimizes SNR of the short-T_2 tissue without incurring image artifacts. Lastly, the proposed method allows for higher readout bandwidth thus shortening sampling time, which in turn reduces blurring due to T_2 decay within the acquisition window (87).

Besides its capability to image extremely short-T2 species, ZTE imaging has also been shown to have potential applications in routine clinical scans due to its low acoustic noise from smoothly varying gradients that reduce the slew rate requirements (22). Therefore, the proposed method may be helpful to broaden the clinical utility of the ZTE imaging sequence.

Currently, the running time of the algorithm to reconstruct a 256^3 image matrix is on the order of 3-4 hours on a PC with 3.16 GHz Intel Xeon CPU and 16 GB RAM. However, the computation of the operators in the system matrix is highly parallelizable, which could significantly accelerate reconstruction speed (current implementation used a single processing thread). GPU implementation of the NUFFT operator has shown more than two orders of magnitude acceleration (97,98). The P operator processes each projection independently and can be parallelized trivially. Devising an accelerated version of the proposed algorithm will be investigated in future work. Another minor limitation is that the B1 peak power increases ~10% for a phase-modulated pulse to achieve the same flip angle as the hard pulse, which is a slight trade-off in return for the significant improvement in image quality.

In conclusion, an effective approach integrating quadratic-phase modulated RF excitation and iterative reconstruction for correcting artifacts caused by the heterogeneous excitation in ZTE imaging is presented. The new method has potential to establish ZTE imaging as a routine pulse sequence for visualization and quantification of short-T_2 tissue constituents.

Chapter 4 Accelerated UTE and ZTE Imaging

4.1 Abstract

Although UTE and ZTE pulse sequences are able to directly image tissue components with sub-millisecond T_2 values, they usually require long scan time. In this chapter two approaches are described to accelerate their imaging speed: compressed sensing and anisotropic field-of-view (FOV). 3D compressed sensing UTE (COMPUTE) and anisotropic FOV ZTE (AFOV ZTE) imaging were developed. Imaging performance was evaluated by simulations and experimentally by phantom, *ex vivo* and *in vivo* scans. Results demonstrated COMPUTE technique achieved an acceleration factor of ~6 and scan time was shortened by a factor of ~3 in AFOV ZTE. They both have potential applications in short-T_2 imaging with long scan time, such as non-proton short-T_2 imaging and inversion recovery-based long-T_2 suppressed imaging.

4.2 Introduction

Although UTE and ZTE pulse sequences are able to directly image tissues with very short-T_2 relaxation time on the order of hundreds of microseconds, they usually require long scan time. For example, 2D UTE imaging is time-inefficient: half-pulse excitation requires two scans with opposite slice-selection gradient polarities to achieve spatial selectivity; radial center-out sampling doubles the scan time for full *k*-space coverage. ZTE imaging is also scan-time intensive, for mainly two reasons: (i) the method is exclusively 3-dimensional by default, which requires a large number of half-projections; (ii) the additional acquisition may be relatively long to fill the missing central portion of *k*-space, depending on the number of missing *k*-space points per half projection. In order

to reduce scan time and improve imaging efficiency, compressed sensing (CS) and trajectory with anisotropic field-of-view are employed in this chapter.

Recently, CS has emerged as a widely used approach to accelerate the imaging speed (99). CS mainly consists of two ingredients: incoherent artifacts and sparse constraint. Since radial trajectories are typically used in UTE and ZTE imaging and undersampled radial trajectories often result in streaking artifact in the reconstructed images which mimics the incoherent artifacts, CS is compatible for UTE and ZTE sampling strategy if the underlying image exhibits sparsity in some transformation domain and the incoherent artifacts are also present in that domain. Typical sparsifying transforms are finite transform, wavelet transform. For long-T_2 suppressed UTE and ZTE, the image itself exhibits sparsity since only short-T_2 tissue signals show up.

In many MRI applications, the target anatomies have asymmetric dimension, which can also be exploited to accelerate scan speed by tailoring the field-of-view (FOV) to their anisotropic shape. This property is especially applicable in short-T_2 imaging, since many short-T_2 tissue rich sites, such as extremities, are elongated. Scheffler et al. proposed to apply trajectory functions with varying angular density to create anisotropic 2D FOV (100). Larson et al. utilized the relationship between *k*-space interval and FOV to design radial trajectories conforming to a given FOV shape (101), allowing shorter the scan time and aliasing artifacts reduction at the same time.

In this chapter, a 3D compressed sensing UTE (COMPUTE) imaging method was developed with a hybrid-radial encoding strategy. Phantom and *in vivo* results show the performance of COMPUTE. A ZTE sequence was designed with anisotropic FOV (AFOV) to tailor its FOV to the shape of the target anatomy. Point spread function (PSF)

simulations were used to evaluate the predicted FOV shape. Further, the proton AFOV ZTE imaging performance was evaluated in a synthetic polymer as well as in cortical bone of the human tibia. Lastly, the feasibility of the method for ^{31}P imaging of mineralized tissue was examined.

4.3 Compressed Sensing UTE (COMPUTE) Imaging

4.3.1 Pulse Sequence

Compared with 2D UTE, 3D UTE provides volume coverage and higher SNR efficiency. Since a hard pulse is employed, 3D UTE is also immune to artifacts associated with half-pulse excitation and obviates the need for two scans with opposite slice-selection gradient polarities. A hybrid stack-of-radial pattern, rather than pure 3D radial acquisition was chosen as the sampling trajectory for the following reasons: 1. It is more straightforward to achieve anisotropic FOV considering that the dimensions of most target anatomies are not spherical, (e.g., tibia); 2. Compared with 3D gridding, the image reconstruction is faster by first applying IFFT in slice dimension followed by 2D gridding reconstruction in each slice, especially considering that iterative image reconstruction algorithm used in this work is time-consuming.

As shown in Fig. 4.1, the hybrid encoding is achieved via radial readout with ramp sampling on the *kx–ky* plane and Fourier encoding along *kz*. To minimize the signal loss from T_2* decay during the phase-encoding period, the duration of the trapezoidal gradients is stepped, thereby minimizing TE at kz=0. To test the feasibility and evaluate the performance of COMPUTE, the full data sets were acquired in both phantom and mid-tibia *in vivo* with the following scan parameters: FOV=160×160×250mm^3,

TE_{min}/TR=50μs/10ms, FA=10º with 20μs pulse duration, 500 half-projections (corresponding to an undersampling factor of 1.6) and 180 readout points per projection, readout bandwidth=±125kHz, 128 slices, reconstructed image matrix=256×256×128, total scan time=10minutes. A four-channel head coil and an eight-channel knee coil were used to image phantom and mid-tibia, respectively.

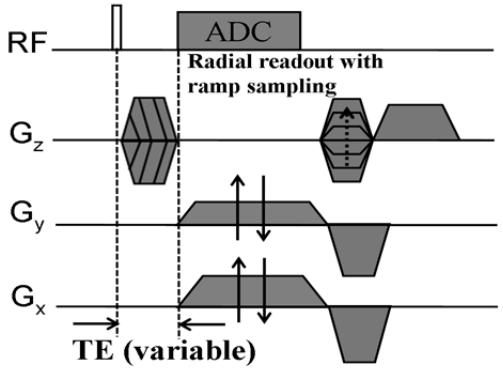

Figure 4.1 Hybrid 3D UTE pulse sequence diagram. The hybrid encoding is achieved via radial readout with ramp sampling on the *kx–ky* plane and Fourier encoding along *kz*. To minimize the signal loss from T_2* decay during the phase-encoding period, the duration of the trapezoidal gradients is stepped to minimize TE.

4.3.2 Simulations and CS Reconstruction

The undersampled data were synthesized by randomly sampling *kz* and variably undersampling the projection views. A power of 5 of distance from the *kz* center was chosen as the sampling probability density function to achieve an undersampling factor of 2 in the *kz* dimension. 250 equiangular views were selected in the central *kz* portion while 125 views in the edge *kz* region. With this undersampling strategy, a total acceleration factor of 10 was achieved.

The images were reconstructed by solving the following optimization problem with total variation (TV) as the sparsity constraint (99):

$$\hat{m} = \arg\min_{m} \left\| F_u m - y \right\|_2^2 + \lambda \left\| Dm \right\|_1 \qquad [1]$$

Here $\hat{m}$ is the reconstructed image, y denotes the undersampled k-space data and λ is the regularization parameter. F_u represents the undersampled Fourier transform operator that maps the image onto the k-space data according to the sampling pattern in COMPUTE, and D is the finite difference operator. $\|\cdot\|_p$ denotes the vector's p-norm. A nonlinear Conjugate Gradient algorithm was used for solving Eq.1. The images were also reconstructed from the undersampled data by zero-filling with density compensation (ZF-w/dc), which consists of zero-filling the missing k-space data, multiplying with k-space density compensation factor (DCF), IFFT along kz and NUFFT (17) on the kx–ky plane. DCF is computed from the probability density function with random sampling, the variable density of radial views along kz and the radial ramp sampling. For comparison, full data sets were used to reconstruct the reference images with the similar procedure as ZF-w/dc but without zero-filling.

4.3.3 Results

Axial phantom images reconstructed from full and undersampled data sets with CS and ZF-w/dc are shown in Fig. 4.2. The streaking artifacts are apparent with ZF-w/dc reconstruction (Fig. 4.2c). These artifacts are significantly reduced with CS reconstruction (Fig. 4.2b). To further compare the reconstruction accuracy, the signal profiles along the dash lines indicated in Fig. 4.2a-c are plotted in Fig. 4.2d, demonstrating that the CS reconstruction recovered the signal from undersampled k-space data with high accuracy.

Fig. 4.3 shows the images of the mid-tibia of a 25-year-old male volunteer in axial and coronal planes with different reconstructions. The CS reconstructed images are still comparable to the fully sampled images but correspond to one sixth of the original scan time. Some smoothing effects are observed in the images from CS reconstruction. A more appropriate choice of the regularization parameter λ would further improve the CS reconstructed images.

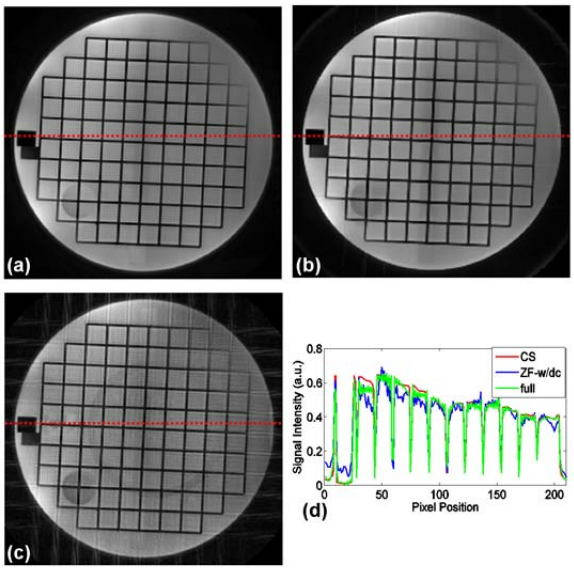

Figure 4.2 Phantom images reconstructed from full data set (a), from undersampled data set with CS (b) and ZF-w/dc (c), with the signal profiles along the red dashed line (d)

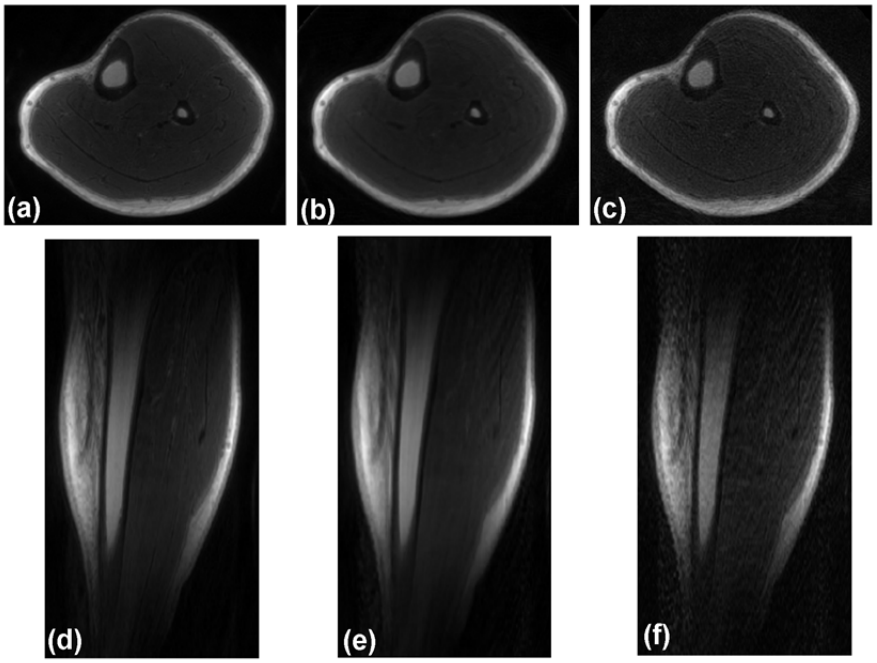

Figure 4.3 *in vivo* mid-tibia images reconstructed from full data set (a, d), from undersampled data set with CS (b, e) and ZF-w/dc (c, f). (a-c) are in the axial plane and (d-f) are in the coronal plane.

4.4 Anisotropic FOV ZTE (AFOV ZTE) Imaging

4.4.1 Pulse Sequence

The anisotropic FOV ZTE imaging sequence was derived from its isotropic counterpart, PETRA, in which the central *k*-space portion is filled by Cartesian SPI while the outer portion is sampled with center-out radial trajectory (9). PETRA was chosen as the prototype ZTE sequence since it offers constant effective echo time in the central k-space part and a smooth *k*-space modulation transfer function, resulting in minimal T_2-blurring.

To generate an asymmetric FOV, the *k*-space sampling patterns of the radial and Cartesian portions in PETRA are treated separately. First, according to the shape of the target anatomy, the FOV is prescribed with estimated size based on localization images;

for example, the mid-tibia can be made to fit into a cylindrical or elliptical volume. Based on the prescribed FOV, the half-projections in the 3D radial part are arranged in a manner analogous to a spiral-based anisotropic FOV design approach described in (101). Specifically, the relationship between the FOV and the *k*-space sampling interval Δk between adjacent projections as a function of the polar angle θ and the azimuthal angle ϕ obey the following relations (101):

$$FOV_{\hat{\theta}}\left(\theta+\frac{\pi}{2},\phi\right)=\frac{1}{\Delta k_{\hat{\theta}}(\theta)} \quad [2]$$

$$FOV_{\hat{\phi}}\left(\theta=\frac{\pi}{2},\phi+\frac{\pi}{2}\right)=\frac{1}{\Delta k_{\hat{\phi}}(\phi)} \quad [3]$$

where $\hat{\theta}$ and $\hat{\phi}$ denote the polar angle and azimuthal directions, respectively. Because of the diffuse nature of streaking artifacts, the radial portion is allowed to be undersampled. In the current implementation, a typical undersampling factor of 4~5 is used.

In the SPI portion, the *k*-space sampling interval in each dimension between neighboring data samples is determined by the maximum FOV in the corresponding dimension according to

$$FOV_i=\frac{1}{\Delta k_i} \quad [4]$$

where i denotes the encoding direction, i.e. *x*, *y* and *z*, and Δk_i is the *k*-space encoding step. To avoid aliasing artifacts, the FOV of SPI should be large enough to encompass the entire object. Fig. 4.4 shows a schematic trajectory diagram in the k_x-k_z plane, creating an

elongated FOV along the k_z dimension. The pulse sequence was implemented on SIEMENS 3T and 7T scanners with cylindrical and ellipsoidal FOV shape support.

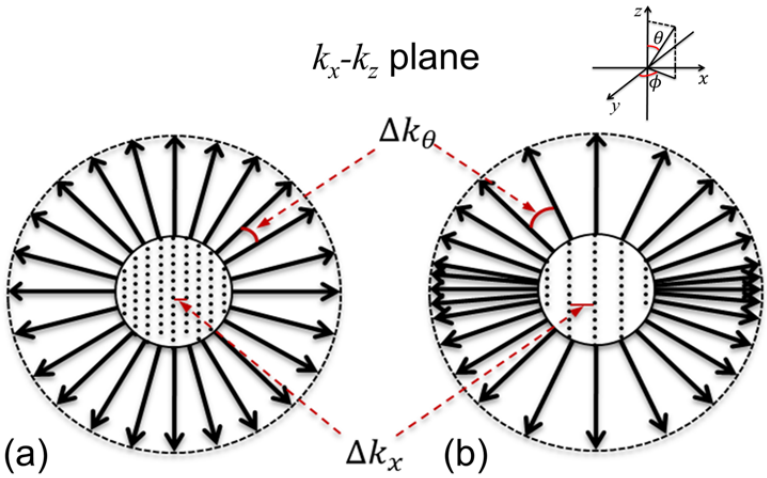

Figure 4.4 Schematic k-space trajectory in k_x-k_z plane of (a) conventional ZTE with isotropic FOV and (b) AFOV ZTE sequences with coordinate system indicated. In the radial portion, the FOV is determined by the spacing between adjacent projections. For example, the FOV along the polar angle θ direction is determined by the *k*-space interval $\Delta \boldsymbol{k_\theta}$ between adjacent spokes along its orthogonal direction. In the Cartesian part, the *k*-space interval $\Delta \boldsymbol{k}$ determines the FOV along the corresponding axis.

4.4.2 Image Reconstruction

Typically, the image can be reconstructed from the hybrid k-space data with the Cartesian portion in the center and radial portion outside by regridding (16). A proper sampling density compensation factor (DCF) needs to be first estimated in the gridding algorithm. However, calculating DCF is more complicated in this case due to the complex *k*-space sampling. Instead, the images were reconstructed by solving the following optimization problem:

$$\hat{m} = \arg\min_{m} \|Fm - y\|_2^2 \qquad [5]$$

Here $\hat{m}$ is the reconstructed image, y denotes the k-space data and F represents the non-uniform Fourier transform operator that maps the image onto the k-space data according to the sampling trajectory. A linear conjugate gradient algorithm was used for solving Eq. 5. The Fourier transform operator F and its adjoint operator F^H were performed by using the NFFT C library function (92).

4.4.3 Simulations and Experiments

Numerical PSF Simulation

PSF simulations were conducted to evaluate the accuracy of the FOV relative to the target shape. The k-space trajectory of the radial portion was designed to generate an aliasing-artifact-free cylindrical FOV volume with diameter and length of 64 and 128, requiring 22,282 half projections in total. The Cartesian portion with 506 single points supported a FOV of size 128×128×256. To better visualize the FOV shape, the image was reconstructed with matrix size of 256×256×256.

Synthetic Polymer Study

A cylindrical sample (length/diameter 60 mm/35 mm) of ultrahigh molecular-weight polyethylene (McMaster-Carr, Robbinsville, NJ) was imaged at 3T (TIM Trio; Siemens Medical Solutions, Erlangen, Germany) using a custom-built 4.5-cm diameter solenoidal RF coil with both anisotropic and isotropic FOV ZTE-PETRA sequences. The T_1 and T_2* relaxation times of this material were 240 ms and 90 μs, respectively, as obtained by saturation recovery NMR and curve fitting. Imaging parameters were the same for both sequences: TR = 7 ms, FA = 15º with 16 μs hard pulse duration, duration between the

end of the RF pulse and the start of the data acquisition was 50 μs, dwell time = 8 μs. Additional parameters relevant to FOV and trajectory are summarized in Table 4.1.

^{31}P Imaging

A cortical bone specimen of the mid-tibia from an 83 years old female donor was scanned at 7T (Magnetom; Siemens Medical Solutions, Erlangen, Germany) with the same AFOV ZTE sequence and a custom-built solenoidal RF coil. 4,872 half-projections were arranged to create a cylindrical FOV with diameter and length of 30 and 60 mm. The SPI portion consisted of 983 samples with FOV of 160×160×320 mm^3 (large FOV was chosen due to low ^{31}P gyromagnetic ratio). Other parameters were: TR = 250 ms, FA=5º with 10 μs hard pulse duration, T/R switch time = 50 μs, readout bandwidth =±100 kHz, reconstructed image matrix = 128×128×256. The total scan time was 24 minutes.

^{1}H Inversion-Recovery (IR) ZTE Imaging of the Human Mid-Tibia in Vivo

To evaluate the performance of proton ZTE for the visualization of collagen-bound bone water the anisotropic FOV sampling strategy was applied to image the mid-tibia of a 30-year-old healthy male subject with an eight-channel transmit/receive knee coil at 3T (TIM Trio; Siemens Medical Solutions, Erlangen, Germany). Informed written consent was obtained from the subject. A hyperbolic secant (HS) adiabatic pulse with a pulse bandwidth/duration of 5000 Hz/5 ms was inserted for magnetization inversion with the central frequency set to the resonance frequency of water. To further shorten scan time, seven ZTE spokes were acquired after each inversion and their excitation flip angles were determined by a binary search algorithm in order to achieve optimum response and

constant amplitude of the collagen-bound bone water signal. The resulting seven flip angles were 16.6°, 17.1°, 17.5°, 18.0°, 18.6°, 19.3 ° and 20.0°. The binary search algorithm is given as follows:

Step 0: Specify tissue parameters, i.e. T_1, T_2, and some imaging parameters: *TI*, *TR*, pulse duration τ, maximum available flip angle θ_{max}, number of ZTE readouts;

Step 1:

a. Set the initial longitudinal magnetization after the inversion recovery (assume the saturation effect of the adiabatic inversion pulse on the bound water pool): $M_{init} = 1 - e^{-TI/T_1}$;
b. Set the maximum available transverse magnetization: $M_{max} = 1 - e^{-TI/T_1}$;
c. Set the minimum transverse magnetization: $M_{min} = 0$;
d. Set the initial guess of the target transverse magnetization at the midpoint: $M_{mid} = (M_{max} + M_{min})/2$;
e. Set the tolerance *tol,* for example, 10^{-5}. The binary search is completed when the search interval size is less than *tol*;

Step 2: Repeat until the search is finished

for each ZTE readout after the inversion

Set initial guess of flip angle: $FA_0 = \sin^{-1}\left(\frac{M_{mid}}{M_{init}}\right)$

Obtain the flip angle θ by solving the following nonlinear equation for the magnetization response to hard pulse excitation:

$$M_{mid} = e^{-\tau/2T_2}\theta \,\mathrm{sinc}\left(\sqrt{\theta^2 - (\tau/2T_2)^2}\right)$$

If θ exceeds θ_{max} or there is no feasible solution, set the search interval to $[M_{min}, M_{mid}]$, and terminate the *for* loop;

Set θ as the excitation flip angle for current ZTE readout;

Calculate the longitudinal magnetization after the ZTE readout:

$$M_z = e^{-\tau/2T_2}\left(\cos\left(\sqrt{\theta^2 - (\tau/2T_2)^2}\right) + (\tau/2T_2)\mathrm{sinc}\left(\sqrt{\theta^2 - (\tau/2T_2)^2}\right)\right)$$

Set the initial longitudinal magnetization for the next ZTE readout:

$$M_{init} = 1 + (M_z - 1)e^{-TR/T_1}$$

end (*for*)

if the search interval is set to $[M_{min}, M_{mid}]$, set $M_{max} = M_{mid}$;

else set $M_{min} = M_{mid}$;

if $M_{max} - M_{min} > tol$, bisect the interval: $M_{mid} = (M_{max} + M_{min})/2$;

else complete the search;

Reset the initial longitudinal magnetization back: $M_{init} = 1 - e^{-TI/T_1}$;

Step 3: Output the optimal flip angles θ and the resulting transverse magnetization M_{mid}.

Other imaging parameters were: TR = 300 ms, T/R switch time = 50 μs, TI (duration between HS pulse and the first ZTE acquisition) = 90 ms, TR of ZTE acquisition = 2 ms, readout bandwidth = ±100 kHz, reconstructed image matrix = 160×160×250. 7,641 half-projections were acquired in the radial part to support an ellipsoidal FOV with principal axes lengths of 40, 40 and 80 mm. The central *k*-space was filled with 1,731 single point samples to support a FOV of 160×160×250 mm^3. For the purpose of comparison, an isotropic FOV IR-ZTE was also run with identical imaging parameters except with

isotropic FOV of 80 mm consisting of 20,125 half-projections and 4,139 single points. The total scan time was 6 minutes 30 seconds for AFOV IR-ZTE and 17 minutes for the isotropic version.

4.4.4 Results

Fig. 4.5 shows the simulated PSF in the three orthogonal planes. The aliasing-artifact free FOV is rectangular in both *yz* and *xz* planes and circular in the *xy* plane, in excellent agreement with the cylindrical shape.

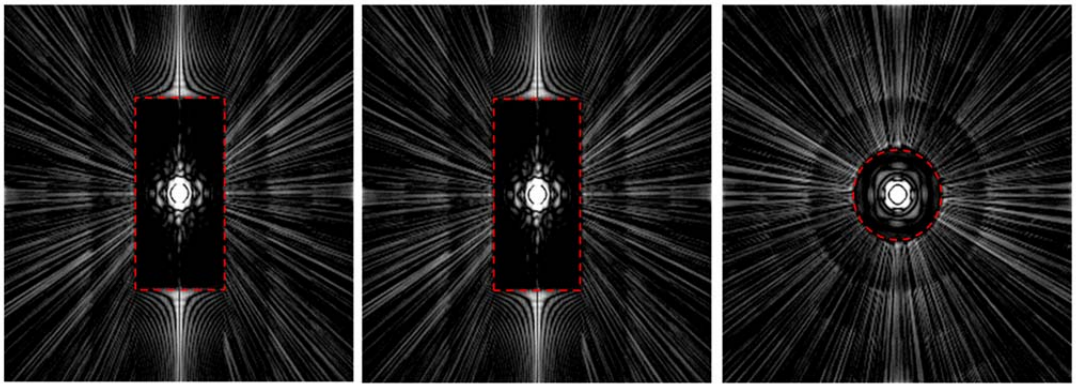

Figure 4.5 PSF of ZTE with cylindrical FOV in the three orthogonal planes: (a) x=0, (b) y=0 and (c) z=0. The rectangular shapes in (a) and (b) and the circular shape in (c) confirm the desired cylindrical FOV shape.

Axial, coronal and sagittal views of the polyethylene sample are shown in Fig. 4.6. The extremely short T_2* of 90 μs results in ~2-pixel image blurring. Scan time is reduced by a factor of about 3 in AFOV ZTE imaging while no aliasing artifacts are observed in the images. However, as expected, the image SNR is lower compared with the isotropic version, as 28 versus 47, calculated as the ratio between the plastic sample signal and the background intensity. Scan parameters and performance characteristics of full FOV and AFOV experiments are summarized in Table 4.1.

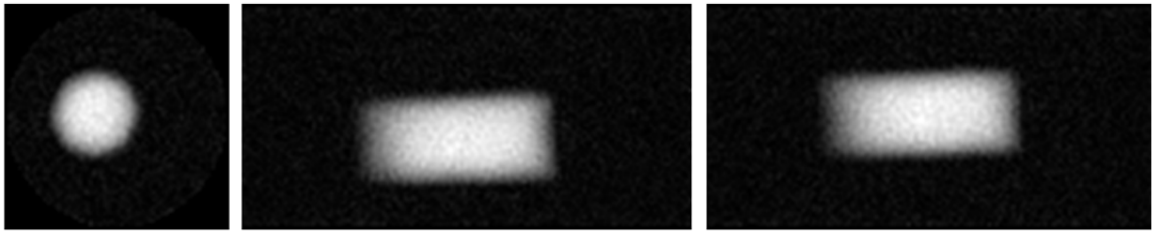

Figure 4.6 AFOV ZTE images at 3T of a polyethylene sample: (a) axial, (b) coronal and (c) sagittal. K-space was sampled with 22,281 half-projections and 507 single points. The cylindrical sample was 35 mm in diameter and 60 mm in length. Given the material's T_2* of approximately 90 μs, a 2-pixel image blurring is estimated. Image SNR was 28 at 1 mm nominal isotropic resolution.

Sequences	Number of Half-Projections	FOV of Radial Portion	Number of Single Points	FOV of SPI (mm^3)	Total Scan Time	SNR
Isotropic ZTE	58,352	128 mm sphere	2,103	128×128×128	7mins 4s	47
AFOV ZTE	22,281	64×64×128 mm^3 cylinder	507	64×64×128	2mins 40s	28

Table 4.1 Comparison of imaging parameters, scan time and SNR between isotropic FOV ZTE and AFOV ZTE in polyethylene phantom scans.

^{31}P image images representing three orthogonal slices, along with 3D volume rendition, are shown in Fig. 4.7. The image blurring due to the short T_2* decay within the sampling is about 3 pixels.

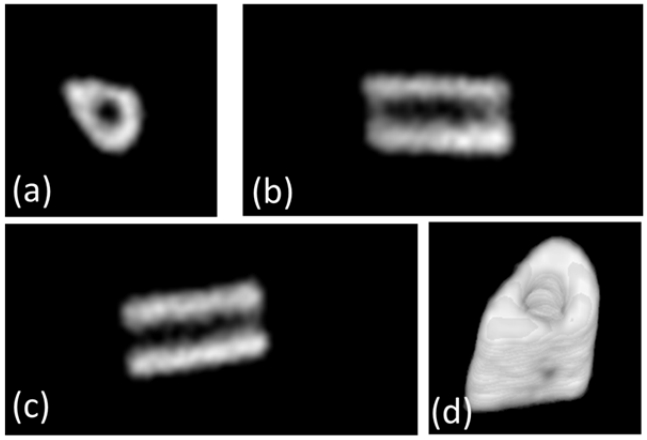

Figure 4.7 AFOV ZTE images at 3T of a polyethylene sample: (a) axial, (b) coronal and (c) sagittal. *K*-space was sampled with 22,281 half-projections and 507 single points. The cylindrical sample was 35 mm in diameter and 60 mm in length. Given the material's T_2* of approximately 90 μs, a 2-pixel image blurring is estimated. Image SNR was 28 at 1 mm nominal isotropic resolution.

Fig. 4.8 displays representative left mid-tibia images in axial and sagittal planes from the long-T_2 suppressed AFOV IR-ZTE image (a, b) and IR-ZTE with isotropic FOV(c, d), along with gradient-echo (GRE) images (e, f) as anatomic references. The corresponding FOV boundaries are indicated by dashed lines in Fig. 4.8 (b) and (d). High contrast between cortical bone and surrounding soft tissue was achieved in all IR-ZTE images, while scan time of AFOV IR-ZTE images was about one third of that of the full-FOV images. Cortical bone SNR of AFOV and isotropic IR-ZTE was 8 and 20, respectively. The signal is predominantly from collagen-bound water while the free water residing in pores with longer T_2 is largely suppressed (42).

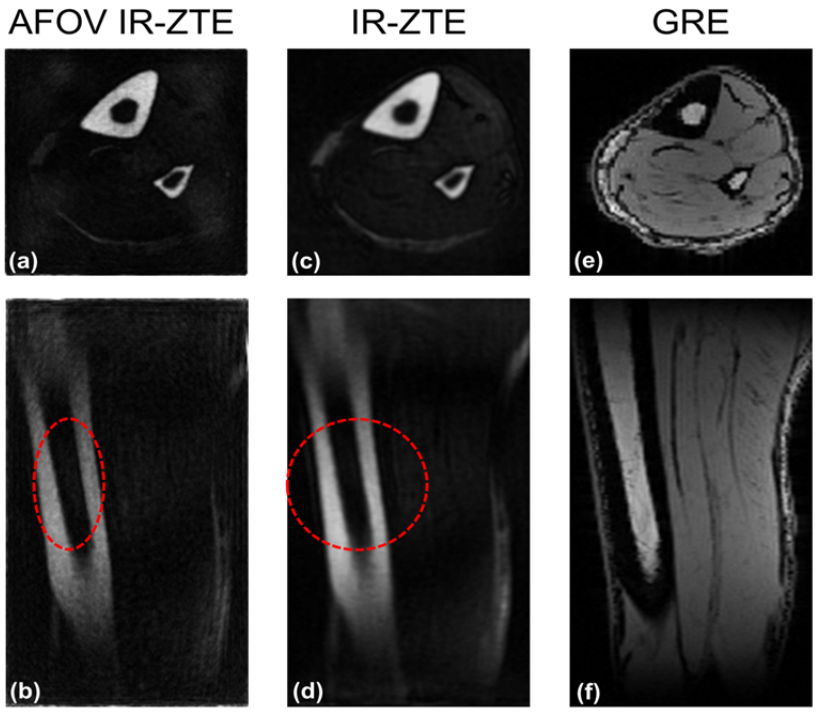

Figure 4.8 *In vivo* mid-tibia images: (a, b) AFOV IR-ZTE, (c, d) isotropic FOV IR-ZTE and (e, f) anatomic reference images from gradient echo sequence. Dashed lines in (b) and (d) indicate the designed FOV boundaries ($40\times40\times80$ mm^3 ellipsoid and 80 mm sphere, respectively, with 1 mm isotropic voxel size). 7,641 half-projections and 1,731 single points were used to sample *k*-space in AFOV IR-ZTE while 20,125 half-projections and 4,139 single points were sampled for isotropic FOV IR-ZTE. Note high contrast between cortical bone and surrounding soft tissue.

4.5 Discussion and Conclusions

In this chapter, CS was applied to UTE imaging (COMPUTE) and anisotropic FOV trajectory to ZTE imaging (AFOV ZTE) to reduce their scan time. COMPUTE consists of a custom-designed hybrid 3D UTE sequence and CS reconstruction. It achieved an acceleration factor of 10 with no perceptible image quality degradation in phantom study and in vivo scans. AFOV ZTE was achieved by appropriately arranging the spokes in the radial portion of *k*-space and the single-sample points in the Cartesian part. PSF simulations confirm that the designed trajectory indeed creates the specified FOV shape. Experiments on synthetic materials indicate that image quality is not compromised while achieving a near 3-fold scan-time reduction relative to isotropic FOV scanning. ^{31}P ZTE of a bone specimen and *in vivo* ^{1}H IR-ZTE imaging of mid-tibial shaft demonstrate its potential applications for non-proton short-T_2 solid-state imaging and inversion recovery-based long-T_2 suppressed imaging.

As shown in Chapter 2, long-T_2 suppression based on adiabatic inversion nulling is a particularly effective approach to create highly uniform short-T_2 contrast (72,96). However, the scan time is largely determined by the inversion delay because data sampling cannot commence until the magnetization of the undesired species reaches the null point, thus rendering IR-ZTE particularly time-inefficient and resulting in prohibitively long scan time for *in vivo* studies.

Both CS and AFOV approaches are suitable to accelerate the imaging speed in IR-based long-T_2 suppressed UTE and ZTE imaging. For CS reconstruction, the sparsity is readily available in the image domain since most of the signals are from short-T_2 tissue constituent. As demonstrated in AFOV ZTE imaging, IR-ZTE combined with multi-

spoke readouts after each adiabatic inversion preparation achieved an acceleration factor of ~3 with effective suppression of long-T_2 components.

CS and AFOV are also beneficial for solid-state imaging applications of nuclei other than protons, such as ^{31}P of mineralized tissues or imaging of rapidly relaxing quadrupolar nuclei (e.g. ^{23}Na, ^{11}B, ^{17}O), where the resulting image is sparse and signal is not contaminated by external objects such as polymeric RF coil structures, which are usually visible in proton ZTE imaging. Extremely long T_1 and short T_2 relaxation times of ^{31}P (~60 s and ~120 μs, respectively (5)), in addition to low gyromagnetic ratio (17.235 MHz/T) pose difficulties in phosphorus imaging of cortical bone. In order to obtain sufficient image SNR, much longer TR is ordinarily used than for proton short-T_2 imaging, thereby resulting in significantly prolonged scan time. One can exploit the sparsity in the image domain since the ^{31}P signal arises from cortical bone only (soft-tissue metabolite concentrations are two to three orders of magnitude lower). FOV can also be adjusted to the bone region rather than including soft tissue, thereby effectively reducing the total scan time.

The main potential problem for CS and AFOV applications in short-T_2 imaging is the SNR loss. Since image SNR is proportional to the square root of the total sampling time, the reduction in the number of projections sampled will exact a SNR penalty. A possible solution to the tradeoff between scan time and SNR is to incorporate anisotropic resolution. In this manner the SNR loss could be offset while possibly further shortening scan time. Anisotropic resolution may be indicated when the signal variation along a given direction is less than in other directions. A case in point is imaging of long bones or

spinal cord, i.e. structures with quasi-axial symmetry. Future extension of the method will include anisotropic resolution as an option.

In summary, UTE and ZTE sequences with compressed sensing and anisotropic FOV were designed and implemented on clinical scanners. COMPUTE and AFOV ZTE achieve substantially reduced scan time without notable image quality degradation. They have potential applications in short-T_2 imaging with long scan times, such as non-proton short-T_2 imaging and IR-based long-T_2 suppressed imaging.

Chapter 5 Cortical Bone Water Quantification with UTE Imaging

5.1 Abstract

In this chapter, UTE sequences were applied to quantify bulk bone water to test the hypothesis that bone water concentration (BWC) is negatively correlated with bone mineral density (BMD) and positively with age, and propose the suppression ratio (SR) (the ratio of signal amplitude without to that with long-T_2 suppression) as a potentially stronger surrogate measure of porosity, which is evaluated *ex vivo* and *in vivo*. BWC in the tibial mid-shafts of 72 healthy human subjects was quantified with a hybrid radial UTE sequence. In a subset of 40 female subjects, the SR was measured with the long-T_2 suppressed UTE sequences developed in Chapter 2. Cortical volumetric BMD (vBMD) was measured with peripheral quantitative computed tomography (CT). The method was validated against micro-CT–derived porosity in 13 donor human cortical bone specimens. Statistical analysis results show that BWC was positively correlated with age ($r = 0.52$) and negatively correlated with vBMD at the same location ($r = -0.57$). Stronger associations with SR were observed ($r = 0.64$ for age; $r = -0.67$ for vBMD), indicating that SR may be a more direct measure of porosity. *Ex vivo* measurements show SR was strongly positively correlated with micro-CT porosity ($r = 0.88$) and with age ($r = 0.87$). The MR imaging-derived SR may serve as a biomarker for cortical bone porosity that is potentially superior to BWC.

5.2 Introduction

UTE MRI has been shown to detect the short-T_2 proton components in cortical bone (7,102). Fernandez et al. subsequently showed that the large majority of the short-T_2

signal resulted from exchangeable protons (103), and Techawiboonwong et al. developed a quantitative UTE method to determine total (bulk) bone water concentration (3,104). Some of this work indicated bulk bone water to be significantly greater in postmenopausal women than in their premenopausal peers and was found to be particularly elevated in patients with end-stage renal disease (3). A significant problem is that during aging and osteoporosis, a loss of osteoid results in a proportionate loss of collagen-bound water while the resulting increase in pore space would cause an increase in pore water. Total bone water concentration, being the sum of these two constituents, may therefore be a less than optimal measure of bone health. This prompted research toward design of methods to separate the two bone water fractions.

Recent work suggests that such separation may be achievable using UTE MRI by exploiting the hypothesized differences in T_2* between the two water populations (39,40). The authors accomplished this goal via bi-exponential analysis of the UTE MRI signal decay measured from a series of UTE images with a range of echo-times (39). While this method is straightforward to implement, it requires collection of image data at many echo times, substantially prolonging scan time and increasing the risk of image corruption by subject motion. It is further complicated by static magnetic field inhomogeneity caused by the magnetic susceptibility difference between bone tissue and water (105), decreasing the T_2* of pore water to values closer to those of bound water, particularly at elevated field strengths. More recently, Horch et al. proposed methods using adiabatic single or double-inversion pulses as a means to obtain images displaying signal from predominantly bound or pore water, respectively (42).

This chapter aims to quantify bulk bone water to test the hypothesis that BWC is negatively correlated with BMD and positively with age, and to propose the suppression ratio, i.e. the ratio of signal amplitude without and with long-T_2 suppression, as a surrogate measure of porosity, which is evaluated *ex vivo* and *in vivo*.

5.3 Methods and Materials

5.3.1 Bulk Bone Water Quantification

Bulk (i.e. total) BWC was quantified with a three-dimensional hybrid-radial ultra-short echo-time (3D HRUTE) imaging technique (Fig. 6.1a). The pulse sequence and processing method were previously developed in the author's laboratory and described in (2). The sequence consists of a half-sinc slab-selective excitation pulse, variable-TE slice-encoding, and involves measurement of T_1 of both bone water and a reference sample of known proton concentration. Signal intensity of bone (I_{bone}) is converted to bone water concentration (ρ_{bone}) using the following equation (2):

$$\rho_{bone} = \rho_{ref} \frac{I_{bone} F_{ref}}{I_{ref} F_{bone}} e^{-TE_{eff}\left(R^*_{2,ref} - R^*_{2,bone}\right)} \qquad [1]$$

where ρ_{ref} is the proton concentration of the reference sample, I_{ref} is the reference signal, TE_{eff} is the effective echo time, and $R^*_{2,ref}$ and $R^*_{2,bone}$ are the effective transverse proton relaxation rates of the reference sample and bone, respectively. Further, the variable F is given as: $F = f\left(T_1, T_2^*, \tau, TR\right) = f_{xy}\left(\tau, T_2^*\right) \dfrac{1 - e^{-\frac{TR}{T_1}}}{1 - f_z\left(\tau, T_2^*\right) e^{-\frac{TR}{T_1}}}$.

where τ is the duration of the UTE half-pulse and terms f_{xy} and f_z are the responses of the transverse and longitudinal magnetization to the RF pulses used in the imaging sequence. Although analytical expressions for f_{xy} and f_z have been derived for rectangular pulses (63), they must be calculated numerically for shaped RF pulses.

This technique does not resolve signals from water residing in different spaces and binding environments; rather, it yields all detectable water in the cortex. All MRI studies were performed on a 3T whole-body scanner (TIM Trio, Siemens Medical Solutions, Erlangen, Germany).

5.3.2 Suppression Ratio

The SR, defined as the ratio of the unsuppressed to the long-T_2 suppressed UTE signal intensity, yields an index of porosity (106). The rationale underlying the proposed approach is that bound water possesses shorter T_2 values (T_2 ~ 300-400 μs) than pore BW (T_2 > 1 ms), as pointed out in the introduction. Thus, in the absence of suppression the UTE sequence detects the signal from both bound and pore water, while the long-T_2 suppressed UTE signal arises primarily from bound water. The suppression ratio should therefore scale positively with pore water fraction, thus representing a surrogate marker of pore volume fraction (i.e., porosity).

In order to partially suppress pore BW, the long-T_2 suppression techniques detailed in Chapter 3 were used. Long-T_2 suppression was achieved in two different ways: (a) with a dual-band saturation pulse (DB-UTE), and (b) with an adiabatic inversion pulse (IR-UTE). In (a), the dual-band saturation pulse used the following parameters: pulse length = 15 ms, flip angle FA (water/fat) = 100°/110°, suppression bandwidth = 120 Hz

on resonance with water and 320 Hz on resonance with the lipid protons centered at 430 Hz (3T). For inversion nulling (b), a hyperbolic secant (HS) pulse was used with the following parameters: pulse bandwidth/duration = 1 kHz/20 ms, 270 Hz frequency-shift towards the lipid peak. The B_1 amplitude was set to allow for 30% variation (maximum B1 amplitude ~20 μT), and TI = 100 ms was chosen to null the pore water signal. The scanner center frequency was set to that of muscle water. The response of different proton pools in cortical bone to the dual-band RF pulse computed by numerical Bloch Equation simulation is shown in Fig. 5.1. The collagen protons with extremely short-T_2 values (~50 μs) (103) are beyond the detection limit of the UTE sequences. The bound water protons contribute to the major portion of UTE signal. On the other hand, the extent to which the pore water is suppressed depends to some extent on the pore size since its T_2 relaxation time is inversely proportional to the surface-to-volume ratio of the pore (107). Generally, the larger the pore size, the smaller the surface-to-volume ratio, resulting in longer T_2 relaxation times for the water in larger pores. Therefore, not only will an increase in pore BW fraction cause increased SR, the increasing contribution of large pores will further enhance the effectiveness of suppression, thereby further elevating SR values. Lastly, any increase in pore volume fraction occurs at the expense of loss of osteoid and therefore bound water, thus reducing the denominator in the quotient $S_{unsuppressed}/S_{suppressed}$, which defines the suppression ratio. Identical digital and analog gain settings were used in the unsuppressed and long T_2-suppressed scans.

In order to evaluate the reproducibility of the SR method, seven subjects (three males and four females) covering the entire age range, were scanned at three time points

within an average period of two weeks and root-mean square error and intra-class correlation coefficient were computed.

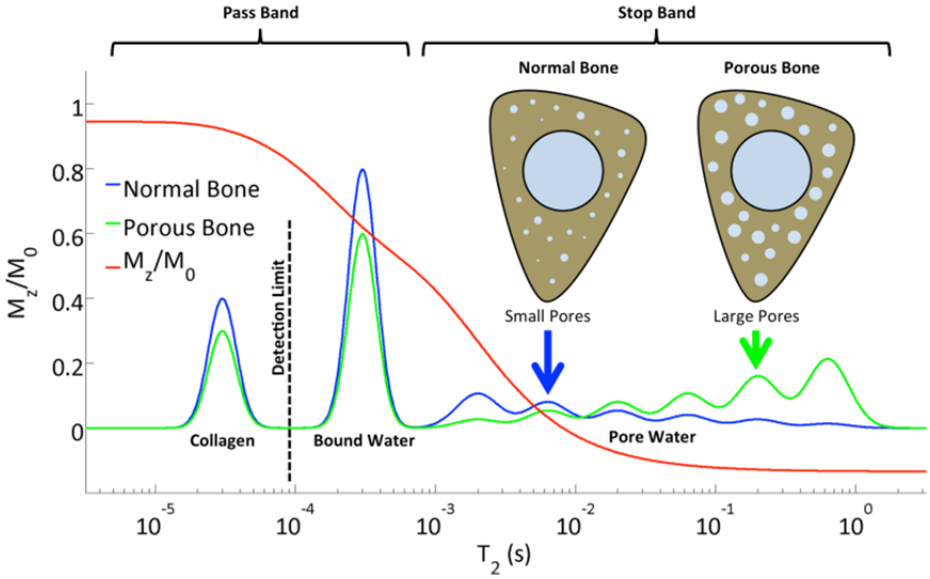

Figure 5.1 Longitudinal magnetization of different proton pools in cortical bone following application of a dual-band saturation pulse as a function of T_2 simulated by a numerical Bloch equation solver. While bound water covers a narrow band centered around 250 µs the pore water ranges in T_2 from about 1 to 1,000 ms. Increased porosity along with greater pore sizes shifts the free water spectrum toward longer T_2 along with increased overall magnitude, therefore leading to increased suppression ratio. In parallel, both bound water and (not detectable) collagen fractions decrease. The various populations of protons are for illustration of principle only and are not drawn to scale.

5.3.3 Human Subject Study

A prospective human subject study was conducted between July 2009 and May 2012. Bulk water was quantified in healthy men (N=30, ages 22-77 years, average 51 years) and women (N=42, ages 26-79 years, average 57 years) evenly covering the age range from 20 to 80 years. Since after menopause bone quality is more variable in women than in men, the number of women enrolled was nine per decade for the age range of 50 to 80 years, and five per decade for men and females less than 50 years old. Subjects with medical histories that included diseases or treatments known to affect bone mineral

homeostasis (e.g. malabsorption syndromes, renal or hepatic disease, or treatment with dexamethasone or methotrexate) or conditions that limit normal physical activity (e.g. stroke, hip or leg fracture, or rheumatoid arthritis) were excluded, as were subjects with BMI>35, or hip BMD z-score ≥2 or ≤-2). Patients were examined with the protocol described above and detailed in Rad et al. (2). 3D UTE images were acquired with the pulse sequence shown in Fig. 2.1 and processed and analyzed as in (2). Specifically, a 5.0-cm axial slab of the left mid-diaphyseal tibia, centered at 38% of tibial length proximal to the lateral malleolus (site of thickest cortex) was scanned with an 8-channel transmit-receive knee coil (Invivo Corp., Gainesville, FL). The lateral malleolus was chosen because it is an easily identifiable landmark.

A subset of the female subjects for whom bulk BWC had previously been obtained (N=34, ages 26-79 years, average 57 years) were selected (complemented by six new subjects since some subjects from the prior cohort were not available) and were re-examined with the SR protocol detailed above. Again, it was ensured that the postmenopausal age range was represented by a greater number of subjects than the premenopausal range. The purpose of this part of the study was to explore the differential abilities of the suppression ratio as a determinant of porosity in comparison to bulk bone water. The rationale for selecting women only was the observation that the range of bulk BWC in men was far smaller than in women (see Results). The anatomic site selected and the size and location of the imaging FOV matched that of the bulk water study. The total scan time for unsuppressed UTE, DB-saturated UTE, and IR-UTE sequences was 15 minutes. The protocols for all human studies were approved by the investigators' Institutional Review Board and written informed consent was obtained from the subjects.

5.3.4 *Ex vivo* Study

To validate the suppression ratio's relationship to porosity, a specimen study was conducted and the results validated by micro-computed tomography (μCT)-based measurements. Thirteen 36-mm long bone specimens were cut from human tibiae (9F, 4M, 27-97 years) procured from the National Disease Research Interchange (NDRI, Philadelphia, PA). The center of each specimen was located at 38% of the total length of the tibia measured proximally from the lateral malleolus to match the scan locations in the *in vivo* study. Bone specimens were housed in plastic tubes containing phosphate-buffered saline and the samples were centrifuged and sealed prior to scanning to eliminate air bubbles. Imaging was performed with an in-house custom-built elliptical transmit-receive birdcage wrist coil at 3T using 2D UTE sequences without and with long-T_2 suppression magnetization preparation. The latter was achieved by both DB-UTE and IR-UTE as described above. Imaging parameters common to all three sequences were: FOV = 180×180 mm^2, slice thickness = 5 mm, TR/TE = 300 ms/50 μs, FA= 60°, sampling frequency bandwidth= ±125 kHz, number of readout points per half-radial projection = 288. Reconstruction yielded a matrix size of 512×512 and in-plane resolution = 0.35×0.35 mm^2. The entire bone volume was scanned and included in the analysis.

For comparison to MRI metrics, cortical bone porosity was measured using μCT. A 3D μCT image dataset of each entire bone specimen was acquired at 9μm isotropic resolution using a Bruker μCT scanner (Bruker, Kontich, Belgium). The endosteal and periosteal borders were segmented, and binary thresholding was applied to distinguish pore space from bone tissue. Porosity was quantified as the ratio of pore volume to total

volume of the segmented bone. Apparent bone mineral density was also measured by peripheral quantitative computed tomography (pQCT). A single slice was acquired at the center of each cortical bone specimen (0.4 mm×0.4 mm×2.3 mm) using a Stratec XCT pQCT scanner (Orthometrix, White Plains, NY), and apparent cortical bone mineral density was quantified in a manner similar to the standard approach used for clinical mid-tibia pQCT studies using the software provided by the manufacturer.

5.3.5 Image Reconstruction

First, *k*-space sampling density compensation weighting, computed on the basis of gradient mapping (which measures the true *k*-space trajectories) (96), was performed. Next, *k*-space data were remapped onto a Cartesian grid using a gridding algorithm and 2D inverse Fourier transform performed. The final magnitude images were generated as the square-root of the sum-of-squares of the images from each coil.

SR maps were computed as a ratio of the conventional UTE image amplitude to the corresponding DB-UTE and IR-UTE image amplitude. Manual segmentation of the periosteal and endosteal cortical boundaries was performed, followed by voxel-wise extraction of IR- and DB-SR values.

5.3.6 Statistical Analysis

A flow chart illustrating the data processing procedure is shown in Fig. 5.2. All image analysis and reconstruction steps were performed using custom-designed software programmed in MATLAB (MathWorks, MA). Correlations between relevant parameters were examined in StatPlus:Mac LE2009 by linear least-squares regression yielding the Pearson correlation coefficient. The significance of each correlation was determined

using one-way ANOVA, with a significance threshold of $p < 0.05$. Retest reproducibility and reliability were assessed in terms of the root-mean-square error and intra-class correlation coefficient.

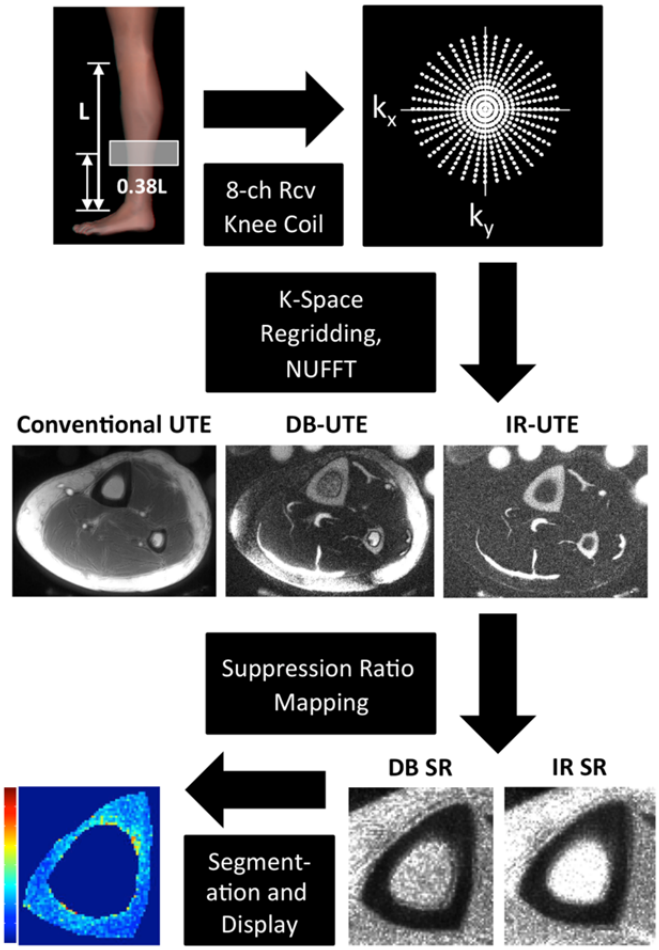

Figure 5.2 Flow chart of SR data acquisition and processing procedure showing an axial slice acquired without (labeled 'conventional UTE') and with DB and IR suppression, yielding suppression ratio maps by taking ratio between conventional UTE image and the corresponding DB- and IR-UTE images. After segmentation of the periosteal and endosteal cortical boundaries SR parametric maps of the cortical bone are obtained. (NUFFT: Non-uniform fast Fourier transform)

5.4 Results

5.4.1 Human Subject Study

Associations involving BWC and suppression ratio versus age and BMD are charted in Fig. 5.3 (data for IR-SR only are shown). While data for all subjects are presented, comparisons of correlation coefficients between the two measures of porosity involve the same cohort of subjects. Both BWC and SR correlated positively with subjects' age (Figs. 5.3a, c). Inclusion of all 72 subjects (30 males, 42 females) in the regression for BWC yielded r=0.46 (N=72, 95% CI: (0.26, 0.63), p<0.001). Stratifying by gender showed no significant correlation for males (N=30, p=0.08) unlike when regressing females only (N=42, r=0.51, 95% CI: (0.25, 0.71), p<0.001). The positive association involving SR (N=34, r=0.64, 95% CI: (0.39, 0.81), p<0.001) appeared stronger than that for BWC involving the same 34 subjects (r=0.52, 95% CI: (0.22, 0.73), p=0.002). This observation is consistent with bulk BW comprising both bound and pore water, which have opposing relationships with porosity (43,108). For the same reason, bulk BW and SR (for the same subjects undergoing studies with both protocols) were only moderately positively associated with each other (N=34; r=0.48, 95% CI: (0.17, 0.70), p=0.004, Fig. 5.3e). Cortical BMD was inversely correlated with BWC (N=72; r=-0.51, 95% CI: (-0.66, -0.32), p<0.001; Fig. 5.3b**)** and with SR (N=40; r=-0.70, 95% CI: (-0.83, -0.50), p<0.001; Fig. 5.3d) suggestive of the notion that increased porosity is an outcome of osteoid loss, which in the case of constant mineralization density scales with volumetric BMD.

Fig. 5.4 shows representative axial mid-tibia SR parametric maps of six subjects covering the spectrum of SR values (Figs. 5.4a-f**)**, along with the corresponding histograms (Fig. 5.4g). Note that SR histograms of bone with low values of SR are

relatively symmetric. In contrast, in bone with higher average SR values, histograms become increasingly asymmetric, with long tails toward high SR values, suggesting the presence of large pores commensurate with long T_2 values. Noticeable also is cortical thinning along with periosteal expansion of the bone in older subjects (e.g. Figs. 5.4e and f).

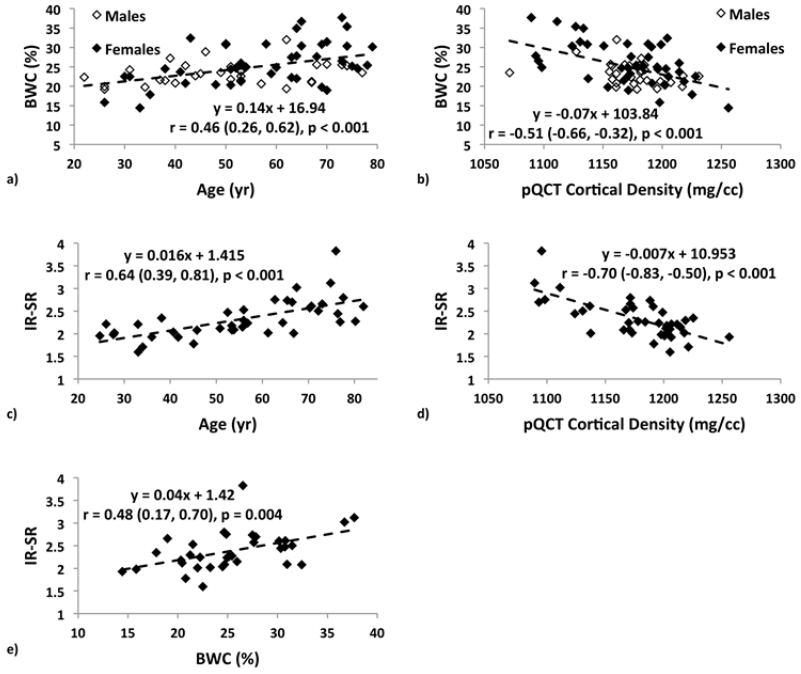

Figure 5.3 Associations between a) BWC and age; b) BWC and cortical pQCT BMD for the entire study population; c) IR-SR and age; d) IR-SR and cortical BMD from pQCT; e) IR-SR and BWC. Both BWC and SR are positively correlated with age but negatively with BMD. The larger correlation coefficients involving SR, as opposed to BWC as the predictor, suggest the former to be a superior biomarker of porosity.

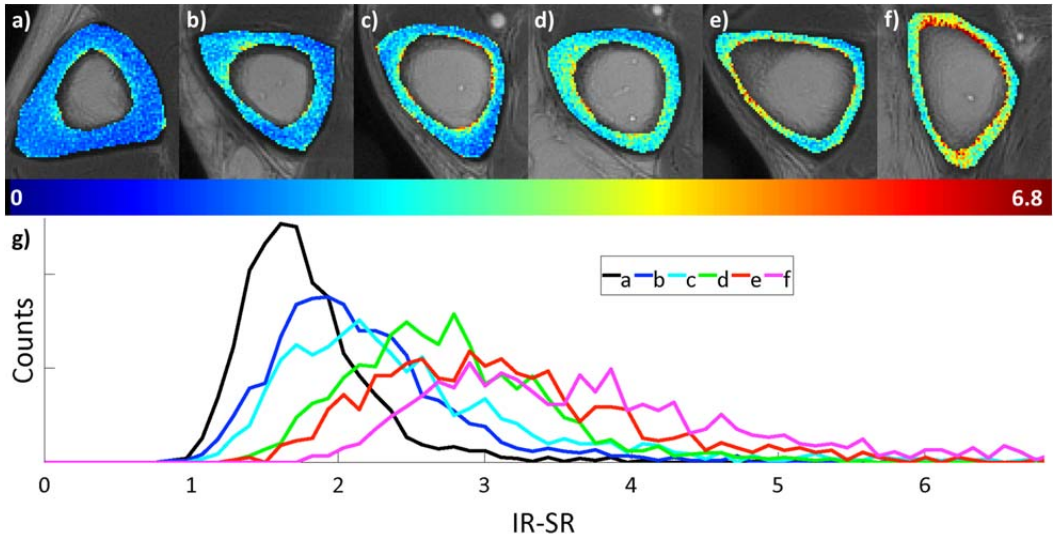

Figure 5.4 Axial mid-tibia IR-SR parametric maps overlaid on anatomic UTE images obtained without long-T_2 suppression in six representative subjects (a-f), along with the corresponding histograms (g). As SR values increase, histograms become increasingly asymmetric with long tails toward high SR values, in line with the notion of elevated T_2 of the water in larger pores.

5.4.2 Reproducibility

Reproducibility data in humans for the measurement of bulk BWC in the tibial shaft have been presented previously (2). Fig. 5.5a shows the test-retest data for SR derived by IR-suppression, yielding an intra-class correlation coefficient of 0.99. As a metric of repeatability, the root mean square error was computed for each subject, which yielded an average within-subject coefficient of variation of 1.5% illustrated in the scatterplot of Fig. 5.5b. Analysis of variance further indicates real differences between subjects ($p<0.001$) suggesting SR to be a reliable differentiator. Similar results were obtained for DB-based suppression (average within-subject coefficient of variation: 1.8%).

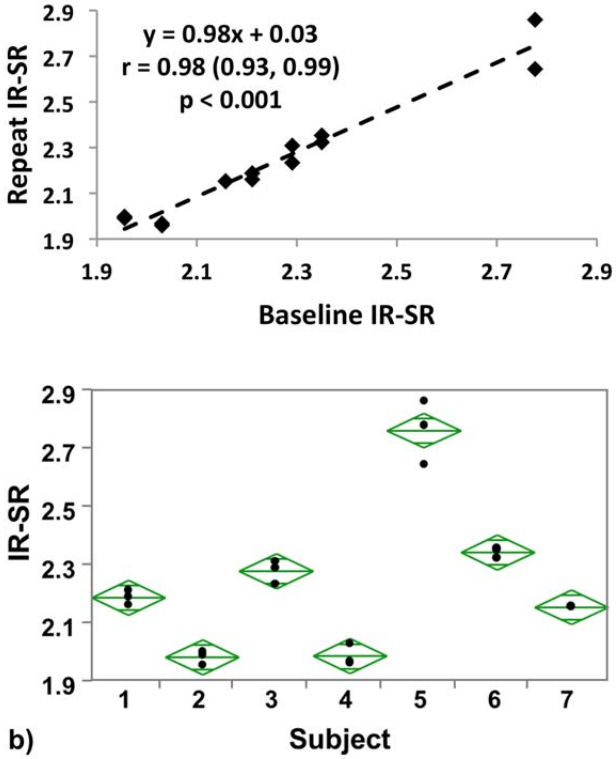

Figure 5.5 Test-retest reproducibility of the IR-SR method. a) Correlation between baseline and first and second follow-up data plotted together on the ordinate in seven subjects; b) Scatterplot of IR-SR values at three time points. Data yielded an intra-class correlation coefficient of 0.99 and average CV of 1.5%.

5.4.3 Correlation between SR values from IR and DB Methods

A high degree of positive correlation between SR values measured by IR and DB methods is observed from the *in vivo* study (N=40; r=0.98, 95% CI: (0.96, 0.99), p<0.001), suggesting that both methods are consistent with each other. For this reason data from only one of the two methods are reported for the *in vivo* study, given the large number of associations examined.

5.4.4 Ex vivo Study

Specimen data, shown for both suppression modes (DB and IR) shown in Figs. 5.6a and b indicate SR and μCT-derived porosity to be strongly positively correlated ((IR) r=0.88, 95% CI: (0.64, 0.96), p<0.001). As expected, cortical BMD was inversely associated with both μCT porosity (r=-0.83, 95% CI: (-0.95, -0.50), p<0.001) and SR (r=-0.57, 95% CI: (-0.85, -0.03), p=0.04), suggesting the variations in BMD to be the result of differences in porosity (data not shown). Further SR and donor age were highly positively correlated with each other (r=0.87, 95% CI: (0.62, 0.96), p<0.001; Fig. 5.6c and d), supporting the expected increase of cortical bone porosity with age (109). Fig. 5.7 shows binary μCT images after pore segmentation and corresponding SR parametric maps from six donors demonstrating a range of mean SR values (Figs. 5.7a-f), along with the histogram of pixel-wise SR values (Fig. 5.7g). Notable are elevated SR in the cortex of older donors paralleling greater μCT porosity. Greater SR is likely the result of a greater proportion of large pores (values up to 385 μm have been reported histologically (110)) associated with elevated T_2 expected in the larger mobile water pools.

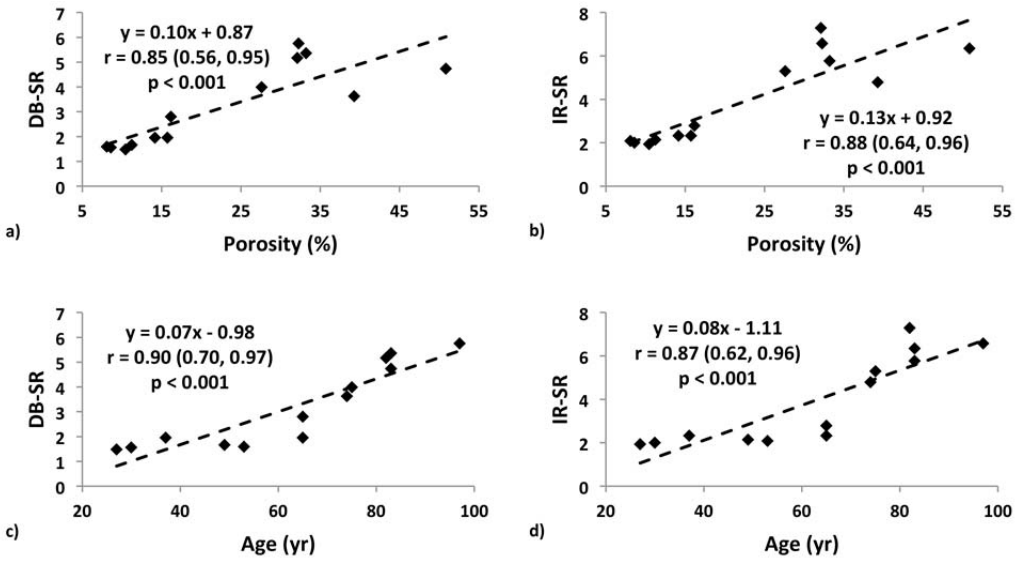

Figure 5.6 Correlation plots in ex vivo validation study (N=13 samples). Data indicate strong associations of SR with both porosity (a, b) as well donor age (c, d) for both SR metrics.

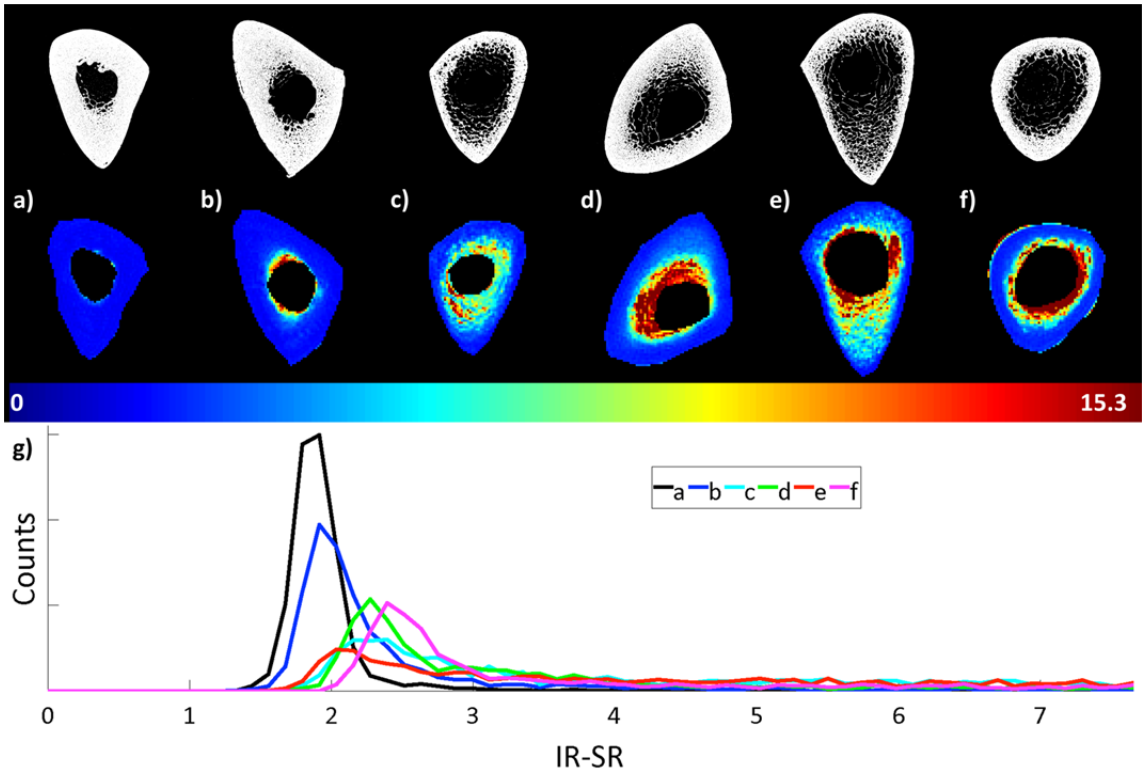

Figure 5.6 Binary μCT images after pore segmentation and corresponding SR parametric maps below from six donors (a-f), along with SR histogram (g). Note the high similarity between the pore distribution in μCT images and the SR maps.

5.5 Discussion and Conclusions

Quantification of BWC has previously shown to be reliably achievable by quantitative UTE imaging techniques in conjunction with a reference sample of known composition and approximately matching relaxation characteristics (3,104). A previous pilot study from the author's laboratory suggested BWC to increase with age (3). By contrast, one would expect a stronger association of bound water with age given that bound water scales with osteoid. The present study suggests SR to be more strongly associated with age than bulk BWC. Both parameters merely require the cortex to be thick enough to provide enough voxels for averaging. However, unlike BWC, the quantification of SR does not require a reference sample. Also, both bulk BWC and SR were negatively correlated with vBMD, with the association of the latter appearing stronger.

Previously, bicomponent analysis (39,111), an approach that makes use of the expected longer effective transverse relaxation time T_2* of pore versus bound water (2-5 ms versus 300-400 μs) has yielded compelling results *ex vivo* in bovine and human cortical bone. However, the method is difficult to perform *in vivo* because of the large number of successive scans that are needed to accurately map the signal decay curve. In contrast, SR, even though it does not yield pore volume fraction, is shown in this work to be a strong predictor of porosity as evidenced by the *ex vivo* data. Notably, these were obtained from human cortical bone of the same anatomic location as the *in vivo* data, and the parameter can conveniently be derived from only two successive scans, obtained with and without long-T_2 suppression, respectively. Indeed, the data in excised bone from the

mid-tibia show that SR is highly predictive of micro-CT porosity (R^2=0.70, p<0.001), more strongly so than the long-T_2* signal fraction as reported in a recent study (R^2=0.25; p<0.001) (111). Further, image processing is simple and does not require curve fitting, which is a fundamentally ill-posed problem. Nevertheless, at least in specimens, where high signal-to-noise ratio is achievable and neither scan duration or subject motion are a consideration, the work in (39,111) performed at 3T field strength shows that the method yields bound water fractions that are of the expected order of magnitude. Further, the bicomponent fitting approach rests on the assumption of only two relaxation components, which has been shown not to be the case since T_2* in porous media is a function of the surface-to-volume area (112).

The present approach is more akin to the method suggested by Horch et al. (42), which showed that pore water can selectively be imaged by preceding the UTE sequence by two successive adiabatic inversion pulses, which restore the pore water signal by virtue of its long T_2 relaxation time while saturating the bound water protons. Obtaining pore volume fraction then requires either a measurement of bulk BW or bound water separately. Manhard et al. recently implemented this technique (113) ona 3T clinical scanner and showed the derived pore water fraction to correlate with values from T_2 spectra obtained independently on a small-bore system at 4.7T as described in (32,43).

The clinical motivation for quantifying pore and bound water is these parameters' relationship to the bone's mechanical properties. As has been well known for over two decades, pore volume fraction is, entirely analogous to man-made materials, a predictor of material strength (see, for example (114)). In a study involving data from over 200 specimens of human cortical bone of the femur, McCalden et al. (38) found age-related

increases in porosity to account for over 70 % of the reduction in strength. Conversely, bound water fraction, as pointed out previously, is proportional to the true density of bone material and thus should be a predictor of bone strength in its own right (43). Indeed, Nyman et al.'s work conducted in femoral cortical bone specimens by means of a relaxometric MR approach on a low-field wide-line system indicated that the fraction assigned to bound water was positively, and mobile water negatively, correlated with fracture toughness (115). More recently, Horch et al., using similar MR relaxometric techniques to separate the relevant water constituents in bone, found the fractions of bound and free (i.e. pore) water to correlate positively (R^2=0.68) and negatively (R^2=0.61), respectively, with peak stress (43).

Importantly, porosity has been shown to be a modifiable parameter. Treatment with antiresorptives has provided evidence of reduced porosity (116,117) quantified on the basis of histomorphometry or μCT analysis of bone biopsies. Since biopsy-based measurements of bone microstructure such as porosity are not clinically practical, a robust noninvasive tool with adequate reproducibility would be desirable. High-resolution peripheral quantitative computed tomography (HRpQCT) has shown to be able to partially resolve pores in the cortex of the distal extremities using segmentation techniques (42). The method has provided useful insight, for example, by differentiating subjects with from those without fractures. In distinction, the MRI-derived SR index can be measured at any anatomic location, including the femoral neck, the site of the most traumatic fractures, since it does not hinge on the ability to physically resolve pores.

Some limitations of this study are noted. First, smaller pores tend to have larger surface-to-volume ratio, resulting in shorter T_2 values of the resident water compared to

larger pores, thereby potentially contributing to the long-T_2 suppressed UTE signal. Generally, IR-UTE is less susceptible to pore BW contamination than DB-UTE due to superior T_2-selecitivity and less sensitivity to B1 inhomogeneity of the adiabatic inversion pulse. These distinguishing properties in the long-T_2 suppression methods probably explain the higher IR-SR values. Second, the proposed SR is a semi-quantitative index in the sense that it does not provide actual pore water volume fraction. Third, this study is not statistically powered to test the hypothesis that SR is more strongly positively correlated with age and negatively with pQCT BMD than is BWC. Lastly, the SR study was conducted 12-18 months after measurement of BWC, so one could argue that biological effects may have confounded the results. This, however, is unlikely since all subjects were healthy and cortical bone remodeling is substantially slower than trabecular remodeling.

Aside from the evidence the study provides for the greater effectiveness of SR as a biomarker for porosity relative to BWC, its simplicity and compatibility with clinical scanners are particularly attractive features. Finally, given the method's reproducibility and ease of implementation, studies in patients at risk of fracture and as a means to evaluate the response to intervention are indicated.

In conclusion, the suppression ratio, i.e. the ratio of UTE MRI signal amplitude obtained without long-T_2 suppression, over the signal with long-T_2 suppression, can potentially be a better biomarker for cortical bone porosity than bulk bone water concentration, thereby providing quantitative insight into the structural degradation of cortical bone in degenerative bone disease.

Chapter 6 Direct Myelin Detection and Quantification with ZTE Imaging

6.1 Abstract

Direct assessment of spatially-resolved myelin concentration has the potential to reveal central nervous system (CNS) abnormalities and enhance our understanding of neurological diseases. The proton spectrum of reconstituted extracted myelin was measured on a 9.4T NMR laboratory spectrometer, from which its T_2 spectrum was calculated via super-Lorentzian line shape fitting. Bloch equation simulations were conducted to investigate the T_2 blurring effect by calculating the image point spread function (PSF) and the fraction of detectable myelin signal under current scanner hardware constraints. Finally, the feasibility of zero-echo time (ZTE) imaging of myelin was demonstrated by imaging reconstituted extracted myelin and intact lamb spinal cord at 9.4T and on a 3T whole-body scanner.

6.2 Introduction

Myelin is an essential biomaterial responsible for electrically insulating axons and thus ensuring efficient neural current transport. Image-based quantification of myelin concentration has the potential to reveal CNS abnormalities, such as multiple sclerosis, and enhance our understanding of neurological diseases. Most current MRI methods for detection of myelin abnormalities use magnetization transfer (MT) imaging or T_2 relaxometry based on water's interaction with myelin. Both methods are indirect, i.e. providing surrogate measures of myelin content, rather than detecting myelin itself, and the underlying biophysical mechanisms are not well understood. Direct detection of myelin would eliminate these complications. Previous work in the author's laboratory

demonstrated that myelin extract and intact rat spinal cord myelin can be imaged on a laboratory 9.4T spectrometer with ultra-short echo time (UTE) imaging (1). However, the extremely short T_2 values (ranging from 1-100 μs) and relatively low proton density pose significant challenges given clinical systems' hardware limitations. In this chapter, the performance of zero-echo time (ZTE) imaging is evaluated with imaging of reconstituted myelin and lamb spinal cord at 9.4T as well as on a 3T whole-body scanner.

6.3 Methods

6.3.1 Myelin Sample Preparation

Myelin was extracted from bovine spinal cord by a sucrose gradient technique, in which the lipid bilayer structure has been shown to be largely preserved (118). Following isolation, the crude myelin was dissolved in a (4:2:1) ternary mixture of chloroform, methanol, and water to remove residual sucrose contaminants. Dissolution in the ternary mixture inverts the bilayer, thereby releasing imbedded proteins, yielding myelin lipids (119). Purified myelin lipids were removed from the chloroform phase following evaporation under a continuous flow of nitrogen gas. The remaining myelin lipid residue was then re-suspended in distilled water, frozen, and lyophilized to remove all remaining traces of solvent. Finally, the purified extract was suspended in 99.9% D_2O to achieve 14% concentration matching that of myelin in white matter. The ^1H spectrum of the purified myelin extract was recorded at 9.4T with the following parameters: SW=100 kHz, NS (number of scans) =256, TD=262144, TR=3.6 s, $\alpha=90^o$, pulse duration = 9.6 μs.

Two 36-mm segments of cervical spinal cord were dissected from the neck of a lamb slaughtered 2 weeks prior. Before imaging, one segment was D_2O-exchanged in 4

passes of 12 mL D_2O-saline each over the course of 44 hours, and one was stored in 12 mL of H_2O-phosphate buffered saline.

6.3.2 Estimation of Fraction of Detected Signal

In order to estimate the fraction of detected signal, the T_2* distribution of myelin was first estimated by fitting the acquired ^1H spectrum into a super-Lorentzian (SL) line shape given by (120):

$$L(\omega) = \int_0^{\pi/2} \frac{\sin(\theta)}{\left|3\cos^2(\theta)-1\right|} f\left[\frac{\omega-\omega_0}{\left|3\cos^2(\theta)-1\right|}\right] d\theta \qquad [1]$$

where ω_0 is the chemical shift, θ is the angle of the lipid bilayer surface normal with respect to B_0, and $f(\omega\text{-}\omega_0)$ is set to be a Lorentzian. From the widths and intensities of these Lorentzians, the T_2^* distribution of a single SL can be calculated. Protons at different chemical shifts, e.g. alkyl chain methylenes, terminal methyls, and choline, are each expected to give rise to SL line shapes (121).

Spectral fitting was performed in Matlab (Mathworks, Natick, MA, USA). Four SLs were used to represent alkyl chain methylenes from fatty acid, cholesterol alkyl chain methylenes, terminal methyls, and choline, while a single Lorentzian was used to model residual HDO. The chemical shifts of each SL were set to the known isotropic shift of the various moieties, and the width and relative intensities were free parameters to be determined from the SL fitting.

Based on the SL fitting results, the fraction of the total myelin signal detected by imaging was estimated. Including the effect of the adiabatic inversion pulse and assuming

the magnetization to have reached a steady state, the acquired myelin signal was calculated as:

$$S = f_{xy}\frac{1-(1-f_{z,inv})\exp(-TI/T_1)-f_{z,inv}\exp(-(TR-T_{inv})/T_1)}{(1-f_{z,inv}f_z\exp(-(TR-T_{inv})/T_1))}\exp(-TE/T_2^*) \quad [2]$$

where $f_{z,inv}$ is the normalized longitudinal magnetization of the myelin protons in response to the adiabatic inversion pulse. T_{inv} is the adiabatic inversion pulse duration, TI is the inversion time, defined as the time interval between the end of the adiabatic pulse and the start of the rectangular excitation pulse. Further, f_{xy} and f_z represent the normalized transverse and longitudinal magnetizations in response to the hard pulse. TR and TE are the repetition time and echo time (defined as the time interval between the end of hard pulse and the start of signal acquisition, i.e. the first readout point), and T_1 and T_2^* are the relaxation times. T_1 was obtained by standard inversion recovery of the myelin lipid extract yielding a value of 0.66±0.03 s. The response of the magnetization to the adiabatic and rectangular pulses due to coherence losses during nutation of the magnetization were computed numerically from the Bloch equations. A matrix-form based Bloch equation simulation algorithm was used to accelerate the computation. Specifically, the pulses were approximated by a series of rectangular sub-pulses of 1 μs duration and the effect of each pulse on the magnetization was evaluated by multiplication with rotation and relaxation matrices. The same approach was also used for computing losses during the RF pulse in the spectroscopic experiments.

The T_2* decay effect on the image blurring was also computed in terms of the point-spread function (PSF). The PSF is governed by the ratio of acquisiton time to T_2*, which

determines the extent to which the highest spatial-frequency signals are attenuated during readout. For 3D radial sampling the FWHM of the PSF in units of voxel length is given as (87):

$$FWHM = 0.41\frac{T_{acq}}{T_2^*} \quad [3]$$

An effective T_2* was estimated from the full width at half maximum (FWHM) of the myelin spectrum and T_{acq} is given as N_s / BW with N_s and BW representing the number of samples along each radial trajectory and BW is the sampling frequency bandwidth.

6.3.3 Hardware Configuration and Image Acquisition

The myelin sample and lamb spinal cord samples were scanned on both 9.4T spectrometer and 3T clinical scanner. At 9.4T, scans were performed using a 15-mm linearly-driven birdcage RF coil in a 1,000 mT/m 3-axis gradient set. 3T imaging was performed with a custom-built 4.5 cm-diameter, 8 cm-long, 3-turn transmit/receive solenoid RF coil constructed using fully ^{1}H-free materials, with 40 mT/m maximum gradient strength.

The myelin extract and D_2O-exchanged lamb spinal cord were scanned at 9.4T using a commercial ZTE sequence with the following parameters: TR=2 ms, FA=4.1^o, 2 μs pulse duration, 3.2 μs dwell time, G=245 mT/m, 80,892 half projections, 188×188×375μm^3 resolution, scan time ~21 mins. To provide reference anatomic images, the H_2O buffered lamb spinal cord was scanned with a turbo-RARE sequence at 51×51×400 μm^3 voxel size. At 3T, the myelin sample was imaged with a ZTE-PETRA sequence with the following parameters: TR=7 ms, FA=8.3^o, 32 μs pulse duration, 16 μs

dwell time, 25,000 half-projections, $1\times1\times1\text{mm}^3$ voxel size, 4 averages, scan time~13mins. To evaluate the feasibility of long-T_2 suppression, the myelin phantom was scanned with an IR-ZTE sequence in which 7 ZTE acquisitions were performed after each adiabatic inversion with TR=300 ms and TI=120 ms (scan time ~18 min). The D_2O-exchanged lamb spinal cord was imaged using the same protocol as myelin extract imaging.

6.4 Results

Fig. 6.1 shows the ^{1}H NMR spectrum of the D_2O suspension of myelin lipid extract. A broad resonance with a superimposed narrow water resonance was observed, consistent with dipolar broadened liquid-crystalline lipid system. The narrow water resonance was from residual HDO. Fig. 6.2 shows the calculated T_2^* distribution for the super-Lorentzian representing the alkyl chain methylene protons as derived from the fit of the myelin lipid extract ^{1}H NMR spectra at 20°C and 37°C. It is representative of the general T_2^* distribution characteristics for all SLs. The T_2^* distribution is bi-modal with the first peak starting at 8 μs and the second peak starting at 16 μs. These two peaks arise from protons with an effective angle of $\theta = 0$ and $\pi/2$ relative to the main magnetic field. The factor of two difference in T_2^* between the peaks results from the $\left|3\cos^2\theta - 1\right|^{-1}$ angular dependence of T_2^* for a SL line shape (120). The large difference in peak intensities is due to the much lower weights ($\sin\theta \times \left|3\cos^2 - 1\right|^{-1}$) of T_2^* components at $\theta = 0$ compared to those at $\theta = \pi/2$.

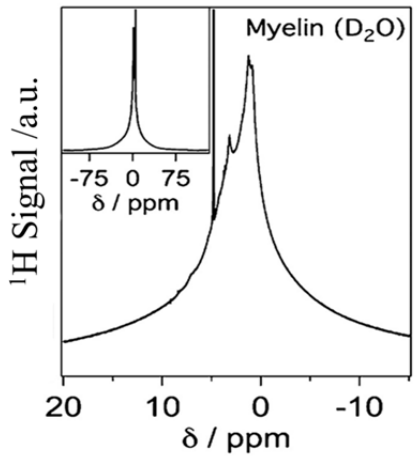

Figure 6.1 The proton spectrum from myelin extract suspended in D_2O. The inset shows the broad resonance with wide tail in the spectrum, indicating the presence of short-T_2 proton signal. The narrow water resonance may from residual HDO.

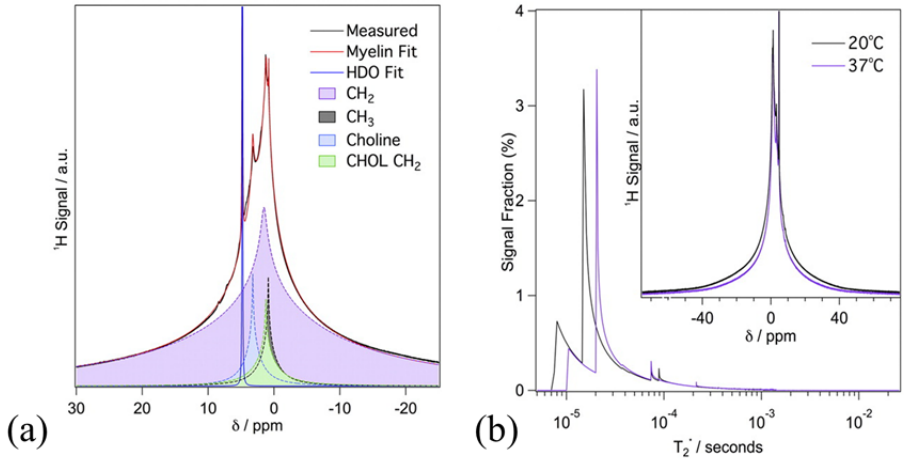

Figure 6.2 Proton NMR spectra and analysis of purified bovine myelin extract suspended in D_2O. (a) NMR spectrum (black) and SL fitting showing the resulting myelin (red) and HDO (blue) fits, as well as the four individual SL components of myelin (shaded). (b) T_2* histogram of myelin components at 20 and 37 °C derived from the SL fitting. Inset: Myelin extract spectra collected at the two temperatures.

Based on the calculated T_2^* spectrum, the Bloch equation simulation showed that 4.9% of the total myelin proton signal (i.e. 0.7% of the total proton signal given that myelin accounts for 14% of WM) to be recoverable on a 3 T clinical MRI system, under

the maximum B_1 and gradient constrains and assuming a 20 μs hard pulse of 7.6º flip angle is used.

FWHM of the PSF for a 3D UTE/ZTE pulse sequence was computed as the intrinsic resolution expected for proton imaging of myelin, at 20 and 37ºC, under the experimental conditions at 9.4 T and 3 T are shown in Table 6.1. As indicated in Table 6.1, the image blurring due to the T_2* decay within the sampling window may be tolerable for direct myelin imaging.

Temperature (ºC)	20	37
FWHM (Hz) at 9.4T	2059	1525
Δx_i (mm) at 9.4T	0.15	0.11
Δx_i (mm) at 3T	1.21	0.90

Table 6.1 Full width at half maximum (FWHM) of the PSF for a 3D UTE/ZTE sequence for myelin imaging at 20 and 37 ºC and field strengths of 9.4 T and 3 T.

Fig. 6.3 shows the 400 MHz myelin extract image at SNR~50. The signal surrounding the sample originates from the RF coil's plastic support. Figs. 6.3b and c show the RARE image of the native tissue sample and ZTE image of the same lamb spinal cord specimen after D_2O-exchange, respectively. The white matter region shows higher signal intensity than gray matter in the ZTE image, consistent with the notion that myelin content is higher in white matter.

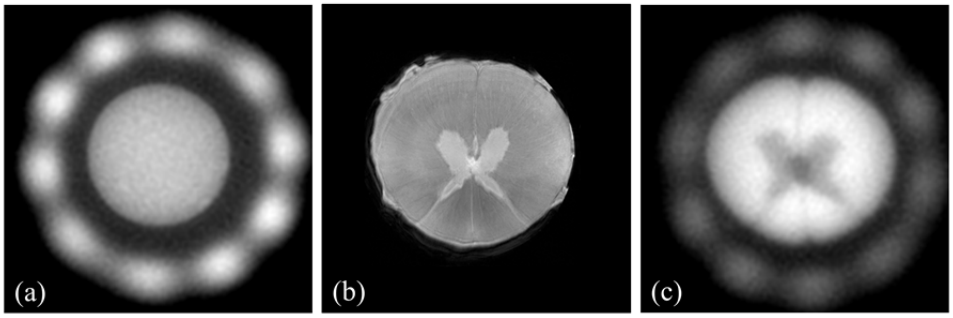

Figure 6.3 9.4T results: (a) ZTE image of myelin extract in D_2O; (b) High-resolution RARE image of lamb spinal cord; (c) ZTE of D_2O exchanged spinal cord.

Myelin extract images at 3T are shown in Figs. 6.4a and b. Image SNR of the myelin sample was ~20 and whereas the signal of D_2O was virtually at noise level, demonstrating that over 99% of the signal in the myelin suspension arose from myelin rather than from residual HDO. More than 90% of the water signal was suppressed in Fig. 6.4b while the myelin extract signal was attenuated by 15%, resulting in higher signal level in the myelin sample than in water. Fig. 6.4c shows the image of D_2O-exchanged lamb spinal cord with SNR~20. Due to the low gradient strengths available on clinical scanners and the very short T_2 of myelin, point-spread function blurring is severe; nevertheless, the central low-signal intensity gray matter is clearly visible. The spectrum in Fig. 6.4d further confirms that the measured signal in Fig. 6.4c arises from myelin.

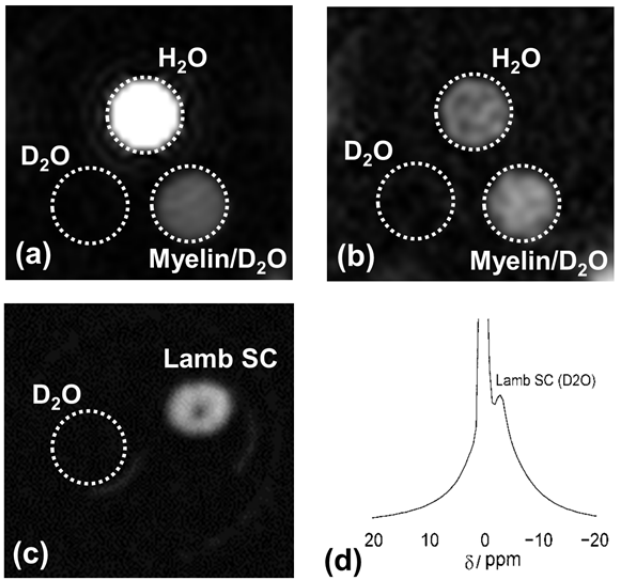

Figure 6.4 3T results: ZTE images of myelin sample (a) without and (b) with long-T_2 suppression; (c) ZTE image and spectrum of D_2O-exchanged lamb spinal cord

6.5 Discussion and Conclusions

In this chapter, the feasibility of direct imaging and quantification of myelin was explored at 3T. To this end, the spectral properties of the myelin proton signal in reconstituted suspensions of myelin lipid extract were characterized. The results show that the short T_2^* component of WM originates primarily from myelin lipid protons and further that direct imaging of these protons is possible at 3 T with ZTE even though the shortest components are not detectable. However, direct myelin imaging *in vivo* is still limited by the hardware constraints, such as gradient strength and the B_1 peak power.

The spectrum of the isolated, reconstituted myelin exhibited a very broad line with relatively narrow components centered approximately 3.5 ppm upfield from water, consistent with methylene protons of alkyl chains, the main constituent of myelin. The myelin resonance is consistent with the SL line shape of a dipolar-broadened liquid-crystalline lipid system (120,122). Following previous work (121), the myelin lipid

extract spectrum was modeled as a sum of SLs representing protons from alkyl chain methylenes, alkyl chain methylenes, terminal methyls, and choline. While the T_2^* distribution showed a wide range of values (0.008 to 26 ms), the distribution was dominated by that of the alkyl chain methylenes as they make up ~75% of the four myelin lipid proton moieties under consideration.

In contrast to the SL fitting performed in this work, Horch et al performed multi-exponential fitting of the time-domain signal decay (61). While the SL line shape theoretically cannot be described with a basis set of exponential functions, the authors suggested that the resulting errors would be small for the case of myelin. Horch et al analyzed FID signals of myelinated mammalian and amphibian nerves as well as synthetic myelin at 4.7 T, yielding histograms of relaxation times. The authors detected significant components with T_2^* values of 20 and 70 μs in frog sciatic nerve, which they conjectured to arise from protein and methylene protons of myelin, respectively. In contrast, as the myelin extract used in this work was free of protein, the present data alternatively suggest the short T_2^* components (<25 μs) to arise from myelin lipids.

The results indicate that about 20% of the protons in myelin lipids have an effective T_2^* less than 25 μs. Even under the more favorable conditions of imaging experiments, the majority of these short T_2^* components remains undetectable. The very short lifetime of the signal has potentially adverse effects on the PSF manifesting as blurring. However, since these extremely short T_2 is not detectable under the current experimental condition, their effects on the image blurring would be negligible. Indeed, the calculation predicted an intrinsic resolution on the order of 1 mm at 3T.

Direct myelin imaging, especially performed *in vivo*, is still challenging. The major limitation is the achievable image SNR. The simulation showed that 4.9% of the total myelin proton signal (i.e. 0.7% of the total proton signal given that myelin accounts for 14% of WM) to be recoverable on a 3 T clinical MRI system. Given that tissue proton centration is ~100 M, the concentration of detectable myelin protons is only about 700 mM. Several factors result in low SNR. First, its extremely short T_2 causes significant signal decay during RF excitation and data sampling. The hardware limitations on clinical scanners pose additional difficulties. In order to minimize the T_2 decay effect, the RF pulse duration needs to be shorten to several microseconds, which would cause the achievable flip angle lower than the optimal angle due to the B_1 peak power and SAR constraints. The maximum gradient strength on the 3T scanner used is 40 mT/m, ~25 times lower than the 9.4T spectrometer used in this work, resulting in longer sampling time and larger T_2 decay effect. Therefore, a dedicated RF coil and gradient coil would be necessary for myelin imaging on clinical scanners.

The performance of long-T_2 suppression is critical in myelin imaging. The residual long-T_2 signal may be misclassified as short T_2^* and hence falsely identified as myelin. Moreover, the long-T_2 suppression module also partially suppresses the myelin proton signal. For example, in IR-based method, the adiabatic inversion pulse saturates the magnetization of myelin protons and the available myelin signal is in fact from the T_1 recovery during the inversion time. However, given the relatively long T_1 of myelin proton (~660 ms), the recovered longitudinal magnetization is about 15% of the equilibrium magnetization.

Another concern is the specificity on myelin detection since it detects myelin solely based on its T_2^* properties. There are other possible non-myelin short-T_2^* sources that could contribute to the ZTE signal, including glial cell membranes, calcifications, tissue scars, vasculature, and hemorrhage (123) that would be indistinguishable from myelin.

In conclusion, both theoretical analysis and the images of myelin extract and spinal cord acquired with ZTE at 3T suggest feasibility of myelin imaging on a clinical scanner. However, *in vivo* myelin imaging is still challenging. Future work needs to optimize the long-T_2 suppression module in ZTE imaging and to apply it to native tissue specimens, eventually to human brain *in vivo*.

Chapter 7 Conclusions and Future Work

7.1 Conclusions

The main results of this thesis research are summarized as follows:

- Three long-T_2 suppressed UTE sequences, i.e. echo subtraction (dual-echo UTE), saturation via dual-band saturation pulses (dual-band UTE), and inversion by adiabatic inversion pulses (IR-UTE) at 3T, were optimized and compared via Bloch simulations and experimentally *in vivo* in the lower extremities of test subjects. Results show that excellent short-T_2 contrast can be achieved with these optimized sequences. A combination of dual-band UTE with dual-echo UTE provides good short-T_2 SNR and CNR with less sensitivity to B_1 homogeneity. IR-UTE was found to have the lowest short-T_2 SNR efficiency but provides highly uniform short-T_2 contrast and is well suited for imaging short-T_2 species with relatively short T_1 such as bone water.
- A novel approach was proposed to correct the image artifacts in ZTE imaging due to the presence of a spatial encoding gradient during excitation by applying quadratic phase-modulated RF excitation and iteratively solving an inverse problem formulated from the signal model of ZTE imaging. A simple pulse sequence was also developed to measure the excitation profile of the RF pulse. Results from simulations, phantom and *in vivo* studies demonstrate the effectiveness of the method in correcting image artifacts caused by inhomogeneous excitation. The proposed method may contribute toward establishing ZTE MRI as a routine 3D pulse sequence for imaging protons and

other nuclei with quasi solid-state behavior on clinical scanners.

- Compressed sensing (CS) and anisotropic field-of-view (FOV) trajectories were firstly applied to shorten the scan time in UTE and ZTE imaging. A hybrid 3D compressed sensing UTE (COMPUTE) sequence and an anisotropic FOV ZTE (AFOV ZTE) sequence were developed. Numerical simulations, phantom and *in vivo* experiments were conducted to demonstrate their imaging performance. A scan time reduction factor of ~6 in COMPUTE and ~3 in AFOV ZTE was achieved without visible image quality degradation. These may have potential applications in non-proton short-T_2 imaging and inversion recovery-based long-T_2 suppressed imaging where long scan time is typically required.
- A new biomarker, suppression ratio (SR) (the ratio of signal amplitude without to that with long-T_2 suppression) as a surrogate measure of cortical bone porosity, was introduced. *Ex vivo* and *in vivo* studies were designed to evaluate the performance of SR index. Experimental data suggest SR may be a more direct measure of porosity than total bone water concentration (BWC), which is also supported by *ex vivo* measurements showing SR to be strongly positively correlated with micro-CT porosity and with age. The MR imaging-derived SR may serve as a biomarker for cortical bone porosity that is potentially superior to BWC.
- The feasibility of direct myelin quantification on a 3T clinical whole body scanner was demonstrated. The proton spectrum of reconstituted extracted myelin on a 9.4T NMR laboratory spectrometer was measured and its T_2 spectrum was

calculated via super-Lorentzian line shape fitting. Bloch equation simulations were conducted to investigate the T_2 blurring effect by calculating the image PSF and the fraction of detectable myelin signal under current scanner hardware constrain. Finally, the feasibility of quantitative ZTE imaging of reconstituted extracted myelin and intact lamb spinal cord was demonstrated at 9.4T and on a 3T whole-body scanner.

7.2 Future Work

Based on the results in this dissertation, several issues need further investigation in future work:

- Develop better long-T_2 suppression methods with shorter scan time and higher SNR: Chapter 3 compares different long-T_2 suppression approaches in UTE imaging and concludes that the IR-based method achieves the most uniform T_2 contrast with less sensitivity to B_1 inhomogeneity. However, IR-UTE suffers from long scan time and low short-T_2 SNR since the adiabatic inversion pulse saturates the short-T_2 species and the short-T_2 signal is mainly from the T_1 recovery during the inversion time. One possible way to achieve shorter scan time and higher SNR is to design more effective T_2-selective pulses to suppress the long T_2 tissue while preserving the short-T_2 species with relatively high B0 and B1 inhomogeneity tolerance. Post-processing approaches may also provide a way to separate short and long-T_2 components from the acquired datasets, such as designing a T_2-selective filter (124,125).
- Develop a faster reconstruction method for ZTE imaging with artifact correction:

Currently, the iterative reconstruction proposed in Chapter 3 needs several hours of CPU time and the most time-consuming step is the NUFFT process, which maps the data between *k*-space and image space. As discussed in Chapter 3, parallel computation is a possible direction. Alternative way is to modify the reconstruction into a non-iterative version. Since the gradient strength changes continuously from *k*-space radial to the center Cartesian region, the excitation profile therefore is also continuous, which allows transformation of the Cartesian into a radial trajectory matched to the acquired radial *k*-space. Then the correction can be done at each projection separately in a non-iterative fashion, followed by regridding to generate the final corrected image.

- Applications of COMPUTE and AFOV ZTE imaging: Chapter 5 showed that scan time can be reduced significantly by compressed sensing and anisotropic FOV. However, only proof-of-concept experiments have been done so far, either by extracting a portion of the fully sampled data, and scanning phantoms and a single healthy subject. Full integration of these methods into UTE and ZTE imaging is needed for applications in short-T_2 tissue quantification, such as cortical bone water and myelin quantification.
- Comparison of myelin imaging with other MRI-based indirect methods: It will be necessary to compare the myelin images with the myelin content derived from indirect methods, such as magnetization transfer or T_2 relaxometry. Results could also be evaluated by correlation with established histological methods by means of myelin staining.
- *In vivo* direct myelin imaging: Chapter 6 presented ZTE images of purified

myelin extract and D_2O-exchanged lamb spinal cord specimen by means of a small solenoidal coil. However, *in vivo* myelin imaging is still challenging and needs a great amount of work and effort. Dedicated RF and gradient coils generating greater B_1 power and gradient strength would almost certainly be necessary for *in vivo* myelin imaging on clinical scanners. Lastly, the performance of long-T_2 suppression needs further improvement in order to further reduce the long-T_2 signal and to maximally preserve the myelin proton signal.

BIBLIOGRAPHY

1. Wilhelm MJ, Ong HH, Wehrli SL, Li C, Tsai PH, Hackney DB, Wehrli FW. Direct magnetic resonance detection of myelin and prospects for quantitative imaging of myelin density. Proceedings of the National Academy of Sciences of the United States of America 2012;109(24):9605-9610.
2. Rad HS, Lam SC, Magland JF, Ong H, Li C, Song HK, Love J, Wehrli FW. Quantifying cortical bone water in vivo by three-dimensional ultra-short echo-time MRI. NMR in biomedicine 2011;24(7):855-864.
3. Techawiboonwong A, Song HK, Leonard MB, Wehrli FW. Cortical bone water: In vivo quantification with ultrashort echo-time MR imaging. Radiology 2008;248(3):824-833.
4. Bergin CJ, Pauly JM, Macovski A. Lung parenchyma: projection reconstruction MR imaging. Radiology 1991;179(3):777-781.
5. Seifert AC, Wright AC, Wehrli SL, Ong HH, Li C, Wehrli FW. 31P NMR relaxation of cortical bone mineral at multiple magnetic field strengths and levels of demineralization. NMR in biomedicine 2013;26(9):1158-1166.
6. Knaap MSvd, Valk J. Magnetic resonance of myelin, myelination, and myelin disorders. Berlin ; New York: Springer; 1995.
7. Robson MD, Gatehouse PD, Bydder M, Bydder GM. Magnetic resonance: an introduction to ultrashort TE (UTE) imaging. Journal of computer assisted tomography 2003;27(6):825-846.
8. Wu Y, Dai G, Ackerman JL, Hrovat MI, Glimcher MJ, Snyder BD, Nazarian A, Chesler DA. Water- and fat-suppressed proton projection MRI (WASPI) of rat femur bone. Magnetic resonance in medicine : official journal of the Society of Magnetic Resonance in Medicine / Society of Magnetic Resonance in Medicine 2007;57(3):554-567.
9. Grodzki DM, Jakob PM, Heismann B. Ultrashort echo time imaging using pointwise encoding time reduction with radial acquisition (PETRA). Magnet Reson Med 2012;67(2):510-518.
10. Weiger M, Pruessmann KP, Hennel F. MRI with zero echo time: hard versus sweep pulse excitation. Magnetic resonance in medicine : official journal of the Society of Magnetic Resonance in Medicine / Society of Magnetic Resonance in Medicine 2011;66(2):379-389.
11. Idiyatullin D, Corum C, Park JY, Garwood M. Fast and quiet MRI using a swept radiofrequency. J Magn Reson 2006;181(2):342-349.
12. Gatehouse PD, Bydder GM. Magnetic resonance imaging of short T2 components in tissue. Clinical radiology 2003;58(1):1-19.
13. Pauly JM, Conolly SM, Nishimura DG, Macovski A. Slice-selective excitation for very short T2 species. In: Proceedings of SMRM, 8th Annual Meeting, Amsterdam, 1989. p 28.
14. Nielsen HT, Gold GE, Olcott EW, Pauly JM, Nishimura DG. Ultra-short echo-time 2D time-of-flight MR angiography using a half-pulse excitation. Magnetic resonance in medicine : official journal of the Society of Magnetic Resonance in Medicine / Society of Magnetic Resonance in Medicine 1999;41(3):591-599.
15. Conolly S, Nishimura D, Macovski A, Glover G. Variable-Rate Selective Excitation. J Magn Reson 1988;78(3):440-458.
16. Jackson JI, Meyer CH, Nishimura DG, Macovski A. Selection of a Convolution Function for Fourier Inversion Using Gridding. Ieee T Med Imaging 1991;10(3):473-478.

17. Greengard L, Lee JY. Accelerating the nonuniform fast Fourier transform. Siam Rev 2004;46(3):443-454.
18. Atkinson IC, Lu A, Thulborn KR. Characterization and correction of system delays and eddy currents for MR imaging with ultrashort echo-time and time-varying gradients. Magnetic resonance in medicine : official journal of the Society of Magnetic Resonance in Medicine / Society of Magnetic Resonance in Medicine 2009;62(2):532-537.
19. Alley MT, Glover GH, Pelc NJ. Gradient characterization using a Fourier-transform technique. Magnet Reson Med 1998;39(4):581-587.
20. Magland JF, Rad HS, Wehrli FW. Correcting for gradient imperfections in ultra-shoft echo time imaging. In: Proceedings of ISMRM, 18th Annual Meeting, Stockholm, Sweden, 2010. p 3102.
21. Kuethe DO, Caprihan A, Lowe IJ, Madio DP, Gach HM. Transforming NMR data despite missing points. J Magn Reson 1999;139(1):18-25.
22. Weiger M, Brunner DO, Dietrich BE, Muller CF, Pruessmann KP. ZTE imaging in humans. Magnetic resonance in medicine : official journal of the Society of Magnetic Resonance in Medicine / Society of Magnetic Resonance in Medicine 2013;70(2):328-332.
23. Grodzki DM, Jakob PM, Heismann B. Correcting slice selectivity in hard pulse sequences. J Magn Reson 2012;214(1):61-67.
24. Idiyatullin D, Corum C, Moeller S, Garwood M. Gapped pulses for frequency-swept MRI. J Magn Reson 2008;193(2):267-273.
25. Idiyatullin D, Suddarth S, Corum CA, Adriany G, Garwood M. Continuous SWIFT. J Magn Reson 2012;220:26-31.
26. Emid S, Creyghton JHN. High-Resolution Nmr Imaging in Solids. Physica B & C 1985;128(1):81-83.
27. Axelson DE, Kantzas A, Nauerth A. H-1 magnetic resonance imaging of rigid polymeric solids. Solid State Nucl Mag 1996;6(4):309-321.
28. Gravina S, Cory DG. Sensitivity and Resolution of Constant-Time Imaging. J Magn Reson Ser B 1994;104(1):53-61.
29. Balcom BJ, Macgregor RP, Beyea SD, Green DP, Armstrong RL, Bremner TW. Single-Point Ramped Imaging with T1 Enhancement (SPRITE). Journal of magnetic resonance Series A 1996;123(1):131-134.
30. Cho ZH, Ro YM. Multipoint K-Space Point Mapping (Kpm) Technique for Nmr Microscopy. Magnet Reson Med 1994;32(2):258-262.
31. Fernandez-Seara MA, Wehrli SL, Wehrli FW. Multipoint mapping for imaging of semi-solid materials. J Magn Reson 2003;160(2):144-150.
32. Horch RA, Nyman JS, Gochberg DF, Dortch RD, Does MD. Characterization of 1H NMR signal in human cortical bone for magnetic resonance imaging. Magnetic resonance in medicine : official journal of the Society of Magnetic Resonance in Medicine / Society of Magnetic Resonance in Medicine 2010;64(3):680-687.
33. Ong HH, Wright AC, Wehrli FW. Deuterium nuclear magnetic resonance unambiguously quantifies pore and collagen-bound water in cortical bone. J Bone Miner Res 2012.
34. Ni QW, Nyman JS, Wang XD, De Los Santos A, Nicolella DP. Assessment of water distribution changes in human cortical bone by nuclear magnetic resonance. Meas Sci Technol 2007;18(3):715-723.
35. Cooper DM, Thomas CD, Clement JG, Turinsky AL, Sensen CW, Hallgrimsson B. Age-dependent change in the 3D structure of cortical porosity at the human femoral midshaft. Bone 2007;40(4):957-965.
36. Seeman E, Delmas PD. Bone quality--the material and structural basis of bone strength

and fragility. N Engl J Med 2006;354(21):2250-2261.
37. Bousson V, Peyrin F, Bergot C, Hausard M, Sautet A, Laredo JD. Cortical bone in the human femoral neck: three-dimensional appearance and porosity using synchrotron radiation. J Bone Miner Res 2004;19(5):794-801.
38. McCalden RW, McGeough JA, Barker MB, Court-Brown CM. Age-related changes in the tensile properties of cortical bone. The relative importance of changes in porosity, mineralization, and microstructure. J Bone Joint Surg Am 1993;75(8):1193-1205.
39. Biswas R, Bae W, Diaz E, Masuda K, Chung CB, Bydder GM, Du J. Ultrashort echo time (UTE) imaging with bi-component analysis: bound and free water evaluation of bovine cortical bone subject to sequential drying. Bone 2012;50(3):749-755.
40. Diaz E, Chung CB, Bae WC, Statum S, Znamirowski R, Bydder GM, Du J. Ultrashort echo time spectroscopic imaging (UTESI): an efficient method for quantifying bound and free water. NMR Biomed 2012;25(1):161-168.
41. Du J, Diaz E, Carl M, Bae W, Chung CB, Bydder GM. Ultrashort echo time imaging with bicomponent analysis. Magnetic resonance in medicine : official journal of the Society of Magnetic Resonance in Medicine / Society of Magnetic Resonance in Medicine 2012;67(3):645-649.
42. Horch RA, Gochberg DF, Nyman JS, Does MD. Clinically compatible MRI strategies for discriminating bound and pore water in cortical bone. Magnetic resonance in medicine : official journal of the Society of Magnetic Resonance in Medicine / Society of Magnetic Resonance in Medicine 2012;68(6):1774-1784.
43. Horch RA, Gochberg DF, Nyman JS, Does MD. Non-invasive predictors of human cortical bone mechanical properties: T(2)-discriminated H NMR compared with high resolution X-ray. PLoS One 2011;6(1):e16359.
44. Nave KA. Myelination and the trophic support of long axons. Nature reviews Neuroscience 2010;11(4):275-283.
45. Griffiths I, Klugmann M, Anderson T, Yool D, Thomson C, Schwab MH, Schneider A, Zimmermann F, McCulloch M, Nadon N, Nave KA. Axonal swellings and degeneration in mice lacking the major proteolipid of myelin. Science 1998;280(5369):1610-1613.
46. Lappe-Siefke C, Goebbels S, Gravel M, Nicksch E, Lee J, Braun PE, Griffiths IR, Nave KA. Disruption of Cnp1 uncouples oligodendroglial functions in axonal support and myelination. Nature genetics 2003;33(3):366-374.
47. Laule C, Kozlowski P, Leung E, Li DKB, MacKay AL, Moore GRW. Myelin water imaging of multiple sclerosis at 7 T: Correlations with histopathology. Neuroimage 2008;40(4):1575-1580.
48. Avila RL, Inouye H, Back RC, Yin XH, Trapp BD, Feltri ML, Wrabetz L, Kirschner DA. Structure and stability of internodal myelin in mouse models of hereditary neuropathy. J Neuropath Exp Neur 2005;64(11):976-990.
49. Wang HF, Fu Y, Zickmund P, Shi RY, Cheng JX. Coherent anti-stokes Raman scattering imaging of axonal myelin in live spinal tissues. Biophys J 2005;89(1):581-591.
50. Fu Y, Huff TB, Wang HW, Wang HF, Cheng JX. Ex vivo and in vivo imaging of myelin fibers in mouse brain by coherent anti-Stokes Raman scattering microscopy. Opt Express 2008;16(24):19396-19409.
51. Wolff SD, Balaban RS. Magnetization transfer contrast (MTC) and tissue water proton relaxation in vivo. Mag Res Med 1989;10:135-144.
52. Dousset V, Grossman RI, Ramer KN, Schnall MD, Young LH, Gonzalez-Scarano F, Lavi E, Cohen JA. Experimental allergic encephalomyelitis and multiple sclerosis: Lesion characterization with magnetization transfer imaging. Radiology 1992;182:483-491.
53. Ropele S, Seifert T, Enzinger C, Fazekas F. Method for quantitative imaging of the

macromolecular 1H fraction in tissues. Magnetic resonance in medicine : official journal of the Society of Magnetic Resonance in Medicine / Society of Magnetic Resonance in Medicine 2003;49(5):864-871.
54. Soellinger M, Langkammer C, Seifert-Held T, Fazekas F, Ropele S. Fast bound pool fraction mapping using stimulated echoes. Magnetic resonance in medicine : official journal of the Society of Magnetic Resonance in Medicine / Society of Magnetic Resonance in Medicine;66(3):717-724.
55. Whittall KP, MacKay AL, Graeb DA, Nugent RA, Li DK, Paty DW. In vivo measurement of T2 distributions and water contents in normal human brain. Magnetic resonance in medicine : official journal of the Society of Magnetic Resonance in Medicine / Society of Magnetic Resonance in Medicine 1997;37(1):34-43.
56. Alonso-Ortiz E, Levesque IR, Pike GB. MRI-based myelin water imaging: A technical review. Magnetic resonance in medicine : official journal of the Society of Magnetic Resonance in Medicine / Society of Magnetic Resonance in Medicine 2014.
57. Schmierer K, Scaravilli F, Altmann DR, Barker GJ, Miller DH. Magnetization transfer ratio and myelin in postmortem multiple sclerosis brain. Ann Neurol 2004;56(3):407-415.
58. Dula AN, Gochberg DF, Valentine HL, Valentine WM, Does MD. Multiexponential T2, magnetization transfer, and quantitative histology in white matter tracts of rat spinal cord. Magn Reson Med 2010;63(4):902-909.
59. Laule C, Vavasour IM, Kolind SH, Li DKB, Traboulsee TL, Moore GRW, MacKay AL. Magnetic resonance imaging of myelin. Neurotherapeutics 2007;4:460-484.
60. Ramani A. Another approach to protons with constricted mobility in white matter: Pilot studies using wideline and high-resolution NMR spectroscopy. Magn Reson Imaging 2003;21:1039-1043.
61. Horch RA, Gore JC, Does MD. Origins of the ultrashort-T2 1H NMR signals in myelinated nerve: A direct measure of myelin content? Mag Res Med 2011;66:24-31.
62. Pauly JM, Conolly SM, Macovski A. Suppression of long-T_2 components for short-T_2 imaging. In: Proceedings of SMRM, 10th Annual Meeting, New York, 1992. p 330.
63. Sussman MS, Pauly JM, Wright GA. Design of practical T2-selective RF excitation (TELEX) pulses. Magnetic resonance in medicine : official journal of the Society of Magnetic Resonance in Medicine / Society of Magnetic Resonance in Medicine 1998;40(6):890-899.
64. Wu Y, Ackerman JL, Chesler DA, Graham L, Wang Y, Glimcher MJ. Density of organic matrix of native mineralized bone measured by water- and fat-suppressed proton projection MRI. Magnetic resonance in medicine : official journal of the Society of Magnetic Resonance in Medicine / Society of Magnetic Resonance in Medicine 2003;50(1):59-68.
65. Larson PE, Gurney PT, Nayak K, Gold GE, Pauly JM, Nishimura DG. Designing long-T2 suppression pulses for ultrashort echo time imaging. Magnetic resonance in medicine : official journal of the Society of Magnetic Resonance in Medicine / Society of Magnetic Resonance in Medicine 2006;56(1):94-103.
66. Larson PE, Conolly SM, Pauly JM, Nishimura DG. Using adiabatic inversion pulses for long-T2 suppression in ultrashort echo time (UTE) imaging. Magnetic resonance in medicine : official journal of the Society of Magnetic Resonance in Medicine / Society of Magnetic Resonance in Medicine 2007;58(5):952-961.
67. Du J, Takahashi AM, Bae WC, Chung CB, Bydder GM. Dual inversion recovery, ultrashort echo time (DIR UTE) imaging: creating high contrast for short-T(2) species. Magnetic resonance in medicine : official journal of the Society of Magnetic Resonance in Medicine / Society of Magnetic Resonance in Medicine 2010;63(2):447-455.

68. Du J, Takahashi AM, Bydder M, Chung CB, Bydder GM. Ultrashort TE imaging with off-resonance saturation contrast (UTE-OSC). Magnetic resonance in medicine : official journal of the Society of Magnetic Resonance in Medicine / Society of Magnetic Resonance in Medicine 2009;62(2):527-531.
69. Pauly J, Le Roux P, Nishimura D, Macovski A. Parameter relations for the Shinnar-Le Roux selective excitation pulse design algorithm. IEEE Trans Med Imaging 1991;10(1):53-65.
70. Wu Y, Hrovat MI, Ackerman JL, Reese TG, Cao H, Ecklund K, Glimcher MJ. Bone matrix imaged in vivo by water- and fat-suppressed proton projection MRI (WASPI) of animal and human subjects. J Magn Reson Imaging 2010;31(4):954-963.
71. Rahmer J, Blume U, Bornert P. Selective 3D ultrashort TE imaging: comparison of "dual-echo" acquisition and magnetization preparation for improving short-T-2 contrast. Magn Reson Mater Phy 2007;20(2):83-92.
72. Du J, Bydder M, Takahashi AM, Carl M, Chung CB, Bydder GM. Short T2 contrast with three-dimensional ultrashort echo time imaging. Magnetic resonance imaging 2011;29(4):470-482.
73. Rad HS, Lam SC, Magland JF, Ong H, Li C, Song HK, Love J, Wehrli FW. Quantifying cortical bone water in vivo by three-dimensional ultra-short echo-time MRI. NMR Biomed 2011.
74. Robson MD, Benjamin M, Gishen P, Bydder GM. Magnetic resonance imaging of the Achilles tendon using ultrashort TE (UTE) pulse sequences. Clinical radiology 2004;59(8):727-735.
75. Du J, Pak BC, Znamirowski R, Statum S, Takahashi A, Chung CB, Bydder GM. Magic angle effect in magnetic resonance imaging of the Achilles tendon and enthesis. Magnetic resonance imaging 2009;27(4):557-564.
76. Jaynes ET. Matrix Treatment of Nuclear Induction. Phys Rev 1955;98(4):1099-1105.
77. Du J, Carl M, Bydder M, Takahashi A, Chung CB, Bydder GM. Qualitative and quantitative ultrashort echo time (UTE) imaging of cortical bone. J Magn Reson 2010;207(2):304-311.
78. Smith MJ, Li C, Bhagat YA, Lam S, Love JH, Wehrli FW. Implications of soft-tissue suppression on cortical bone water signal in ultrashort echo-time imaging. In: Proceedings of ISMRM, 19th Annual Meeting, Montreal, Canada, 2011. p 1131.
79. Pauly JM. Design of large-flip-angle half pulse. In: Proceedings of ISMRM, 14th Annual Meeting, Seattle, 2006. p 2997.
80. Bydder M, Rahal A, Fullerton GD, Bydder GM. The magic angle effect: a source of artifact, determinant of image contrast, and technique for imaging. J Magn Reson Imaging 2007;25(2):290-300.
81. Norris DG, Ludemann H, Leibfritz D. An Analysis of the Effects of Short T2 Values on the Hyperbolic-Secant Pulse. J Magn Reson 1991;92(1):94-101.
82. Johnson AJ, Garwood M, Ugurbil K. Slice Selection with Gradient-Modulated Adiabatic Excitation Despite the Presence of Large B1-Inhomogeneities. J Magn Reson 1989;81(3):653-660.
83. Goelman G. Two methods for peak RF power minimization of multiple inversion-band pulses. Magnetic resonance in medicine : official journal of the Society of Magnetic Resonance in Medicine / Society of Magnetic Resonance in Medicine 1997;37(5):658-665.
84. Du J, Corbeil J, Znamirowski R, Angle N, Peterson M, Bydder GM, Kahn AM. Direct imaging and quantification of carotid plaque calcification. Magnetic resonance in medicine : official journal of the Society of Magnetic Resonance in Medicine / Society of

Magnetic Resonance in Medicine 2010.
85. Chan CF, Keenan NG, Nielles-Vallespin S, Gatehouse P, Sheppard MN, Boyle JJ, Pennell DJ, Firmin DN. Ultra-short echo time cardiovascular magnetic resonance of atherosclerotic carotid plaque. J Cardiovasc Magn R 2010;12:17.
86. Wilhelm MJ, Ong HH, Wehrli SL, Tsai P-H, Hackney DB, Wehrli FW. Prospects for quantitative imaging of myelin with dual-echo short inversion time 3D UTE MRI. In: Proceedings of ISMRM, 19th Annual Meeting, Montreal, Canada, 2011. p 2460.
87. Rahmer J, Bornert P, Groen J, Bos C. Three-dimensional radial ultrashort echo-time imaging with T2 adapted sampling. Magnetic resonance in medicine : official journal of the Society of Magnetic Resonance in Medicine / Society of Magnetic Resonance in Medicine 2006;55(5):1075-1082.
88. Pauly J, Nishimura D, Macovski A. A K-Space Analysis of Small-Tip-Angle Excitation. J Magn Reson 1989;81(1):43-56.
89. Hinshaw WS, Lent AH. An Introduction to Nmr Imaging - from the Bloch Equation to the Imaging Equation. P Ieee 1983;71(3):338-350.
90. Block KT, Uecker M, Frahm J. Undersampled radial MRI with multiple coils. Iterative image reconstruction using a total variation constraint. Magnet Reson Med 2007;57(6):1086-1098.
91. Goldstein T, Osher S. The Split Bregman Method for L1-Regularized Problems. Siam J Imaging Sci 2009;2(2):323-343.
92. Keiner J, Kunis S, Potts D. Using NFFT 3-A Software Library for Various Nonequispaced Fast Fourier Transforms. Acm T Math Software 2009;36(4).
93. Fraser D. Interpolation by the Fft Revisited - an Experimental Investigation. Ieee T Acoust Speech 1989;37(5):665-675.
94. Seifert AC, Wright AC, Wehrli SL, Ong HH, Li C, Wehrli FW. P NMR relaxation of cortical bone mineral at multiple magnetic field strengths and levels of demineralization. NMR in biomedicine 2013.
95. Weiger M, Pruessmann KP, Bracher AK, Kohler S, Lehmann V, Wolfram U, Hennel F, Rasche V. High-resolution ZTE imaging of human teeth. NMR in biomedicine 2012;25(10):1144-1151.
96. Li C, Magland JF, Rad HS, Song HK, Wehrli FW. Comparison of optimized soft-tissue suppression schemes for ultrashort echo time MRI. Magnetic resonance in medicine : official journal of the Society of Magnetic Resonance in Medicine / Society of Magnetic Resonance in Medicine 2012;68(3):680-689.
97. Sorensen TS, Schaeffter T, Noe KO, Hansen MS. Accelerating the nonequispaced fast Fourier transform on commodity graphics hardware. Ieee T Med Imaging 2008;27(4):538-547.
98. Gai JD, Obeid N, Holtrop JL, Wu XL, Lam F, Fu MJ, Haldar JP, Hwu WMW, Liang ZP, Sutton BP. More IMPATIENT: A gridding-accelerated Toeplitz-based strategy for non-Cartesian high-resolution 3D MRI on GPUs. J Parallel Distr Com 2013;73(5):686-697.
99. Lustig M, Donoho D, Pauly JM. Sparse MRI: The application of compressed sensing for rapid MR imaging. Magnetic resonance in medicine : official journal of the Society of Magnetic Resonance in Medicine / Society of Magnetic Resonance in Medicine 2007;58(6):1182-1195.
100. Scheffler K, Hennig J. Reduced circular field-of-view imaging. Magnetic resonance in medicine : official journal of the Society of Magnetic Resonance in Medicine / Society of Magnetic Resonance in Medicine 1998;40(3):474-480.
101. Larson PZ, Gurney PT, Nishimura DG. Anisotropic field-of-views in radial imaging. IEEE Trans Med Imaging 2008;27(1):47-57.

102. Reichert IL, Robson MD, Gatehouse PD, He T, Chappell KE, Holmes J, Girgis S, Bydder GM. Magnetic resonance imaging of cortical bone with ultrashort TE pulse sequences. Magnetic resonance imaging 2005;23(5):611-618.
103. Fernandez-Seara M, Wehrli SL, Takahashi M, Wehrli FW. Water content measured by proton-deuteron exchange NMR predicts bone mineral density and mechanical properties. J Bone Mineral Res 2004;19(2):289-296.
104. Techawiboonwong A, Song HK, Wehrli FW. In vivo MRI of submillisecond T(2) species with two-dimensional and three-dimensional radial sequences and applications to the measurement of cortical bone water. NMR Biomed 2007;21(1):59-70.
105. Hopkins JA, Wehrli FW. Magnetic susceptibility measurement of insoluble solids by NMR: magnetic susceptibility of bone. Magnetic resonance in medicine : official journal of the Society of Magnetic Resonance in Medicine / Society of Magnetic Resonance in Medicine 1997;**37**:494-500.
106. Li C, Seifert AC, Rad HS, Bhagat Y, Rajapakse CS, Sun W, Lam SC, Wehrli FW. Cortical Bone Water Concentration: Dependence of MR Imaging Measures on Age and Pore Volume Fraction. Radiology 2014:132585.
107. Wang X, Ni Q. Determination of cortical bone porosity and pore size distribution using a low field pulsed NMR approach. J Orthop Res 2003;21(2):312-319.
108. Rad HS, Lam SC, Magland JF, Ong H, Li C, Song HK, Love J, Wehrli FW. Quantifying cortical bone water in vivo by three-dimensional ultra-short echo-time MRI. NMR in Biomedicine 2011;24(7):855-864.
109. Bousson V, Meunier A, Bergot C, Vicaut E, Rocha MA, Morais MH, Laval-Jeantet AM, Laredo JD. Distribution of intracortical porosity in human midfemoral cortex by age and gender. J Bone Miner Res 2001;16(7):1308-1317.
110. Bell KL, Loveridge N, Jordan GR, Power J, Constant CR, Reeve J. A novel mechanism for induction of increased cortical porosity in cases of intracapsular hip fracture. Bone 2000;27(2):297-304.
111. Bae WC, Chen PC, Chung CB, Masuda K, D'Lima D, Du J. Quantitative ultrashort echo time (UTE) MRI of human cortical bone: correlation with porosity and biomechanical properties. J Bone Miner Res 2012;27(4):848-857.
112. Ni Q, King J, Wang X. The characterization of human compact bone structure changes by low-field nuclear magnetic resonance. Meas Sci Technol 2004(15):58–66.
113. Manhard MK, Horch RA, Harkins KD, Gochberg DF, Nyman JS, Does MD. Validation of quantitative bound- and pore-water imaging in cortical bone. Magnetic resonance in medicine : official journal of the Society of Magnetic Resonance in Medicine / Society of Magnetic Resonance in Medicine 2014;71(6):2166-2171.
114. Martin RB. Determinants of the Mechanical Properties of Bone. Journal of Biomechanics 1991;24(S1):79-88.
115. Nyman JS, Ni Q, Nicolella DP, Wang X. Measurements of mobile and bound water by nuclear magnetic resonance correlate with mechanical properties of bone. Bone 2008;42(1):193-199.
116. Borah B, Dufresne T, Nurre J, Phipps R, Chmielewski P, Wagner L, Lundy M, Bouxsein M, Zebaze R, Seeman E. Risedronate reduces intracortical porosity in women with osteoporosis. J Bone Miner Res 2010;25(1):41-47.
117. Roschger P, Rinnerthaler S, Yates J, Rodan GA, Fratzl P, Klaushofer K. Alendronate increases degree and uniformity of mineralization in cancellous bone and decreases the porosity in cortical bone of osteoporotic women. Bone 2001;29(2):185-191.
118. Norton WT. Isolation of myelin from nerve tissue. Methods Enzymol 1974;31:435-444.
119. Wessel D, Flugge UI. A method for the quantitative recovery of protein in dilute solution

in the presence of detergents and lipids. Analytical biochemistry 1984;138(1):141-143.
120. Wennerstrom H. Proton nuclear magnetic resonance lineshapes in lamellar liquid crystals. Chem Phys Lett 1973;18:41-44.
121. Ulmius J, Wennerström H, Lindblom G, Arvidson G. Proton NMR bandshape studies of lamellar liquid crystals and gel phases containing lecithins and cholesterol. Biochim Biophys Acta 1975;389:197-202.
122. Bloom M, Holmes K, Mountford C, Williams P. Complete proton magnetic resonance in whole cells. J Magn Reson 1986;69:73-91.
123. Waldman A, Rees JH, Brock CS, Robson MD, Gatehouse PD, Bydder GM. MRI of the brain with ultra-short echo-time pulse sequences. Neuroradiology 2003;45:887-892.
124. Jones CK, Xiang Q-S, Whittall KP, MacKay AL. Linear combination of multiecho data: short T2 component selection. Mag Res Med 2004;51:495-502.
125. Vidarsson L, Conolly SM, Lim KO, Gold GE, Pauly JM. Echo time optimization for linear combination myelin imaging. Mag Res Med 2005;53:398-407.